# A Statistical Analysis of Rouge Waves

**Eva Charlotte Berner**
Master's Thesis, Spring 2022

This master's thesis is submitted under the master's programme *Fluid Mechanics*, with programme option *Energy, Environment and Safety*, at the Department of Mathematics, University of Oslo. The scope of the thesis is 60 credits.

The front page depicts a section of the root system of the exceptional Lie group $E_8$, projected into the plane. Lie groups were invented by the Norwegian mathematician Sophus Lie (1842–1899) to express symmetries in differential equations and today they play a central role in various parts of mathematics.

To Dad
Finn Berner

$04.04.1944 - 11.10.2021$

Although you never saw the completion of this work,
you're in every page.

# Abstract

This master thesis studies the statistical properties of waves generated at the Hydrodynamics Laboratory of the Department of Mathematics at the University of Oslo. We look at two distinct experimental setups. First, we study the evolution of two different, fairly narrow banded spectra and verify the results found in K. B. Dysthe et al. (2003). We show that the wave spectrum with the highest initial Benjamin-Feir index also has the sharpest increase in surface elevation kurtosis as the wave process propagates. Additionally, we discover that for the process with the highest initial Benjamin-Feir index, the surface elevation and velocity field kurtosis increase at different rates. Second, we study the effects of an asymmetric shoal on a wave process with a Pierson-Moskowitz wave spectrum. We show that the kurtosis and skewness of the surface elevation and velocity field display similar tendencies as the results in Trulsen, Raustøl et al. (2020). The higher order comoments are studied and we show that the steeper the uphill slope of the shoal, the lower the cokurtosis. Then, by using Q-Q plots, estimated probability density functions and PDFs, we discover that the distribution of the surface elevation and velocity behave differently. Moreover, we show that the dependence structure of the surface elevation and velocity field is best described by a T-copula.

# Acknowledgements

I have been fascinated by the ocean since I was a little girl. These last two years, as a master student, I have had the profound privilege of following my childhood interest. For that, I am eternally grateful.

There are a handful of people who have made this thesis possible. Firstly, I would like to thank my supervisor professor Karsten Trulsen. A friend, mentor and unwitting matchmaker. Your enthusiasm and support has been invaluable. You have an incredible ability to bring out the best in your students.

I would also like to thank Lab Engineer Olav Gundersen for building a fantastic shoal and being an equipment guru. Thank you for looking out for me when I returned to the lab last October.

I would also like to thank my friends, and the 901 study hall. Thank you to Karen Samseth for our many long conversations, and excellent collaboration these last three months.

Thank you Mum, Else Christina Wigen Berner. You are my role model, my best friend, and permanent proofreader.

Finally, thank you to my fiancé Martin Hornkjøl. You are the wind beneath my wings and the love of my life.

# Contents

# CHAPTER 1

## Introduction

The Eggum stone is a viking grave stone dated to $650 - 700$ A.D. with runic inscriptions found in Sogndal, Norway. It is a description of a shipwreck in bad weather. The mast had broken and the vikings' oars could not save them. The god Ægir cast a death wave upon them. The ship and crew were lost.

Tales of unexpectedly large, 'monster', waves lurching towards ships and ocean structures, causing mayhem and destruction have been reported throughout maritime history. The reports have been relegated to maritime myth, not to be taken too seriously and fit to scare only those who have yet to fully attain their sea legs.

In academia, this skepticism could be attributed to the deterministic framework of nineteenth-century fluid mechanics not understanding the inherent randomness of the ocean surface.

It was not until after the Second World War that stochastic analysis was implemented in ocean wave forecasting. Yet, our ability to successfully predict rogue waves, and provide warnings to seafarers, remains the same as the crew whose fate is described on the Eggum stone.

Recently, oceanic rogue waves have garnered significant attention from academia, shipping and offshore industries, with good reason. Life-threatening waves are bad for business. An example of such a wave is the 'New Year Wave' that hit the Draupner oil platform and had a significant wave height of 11.8 meters and a maximum wave height of 25.6 meters, Haver (2004).



Figure 1.1: The Eggum stone. Originally called 'Del av innskrifta på Eggjasteinen' by Arild Finne Nybø. Picture acquired from Store Norske Leksikon, https://snl.no/Eggjasteinen. The image is used under a Creative Commons 3.0 liscense: https://creativecommons.org/licenses/by-sa/3.0/no/

In fluid mechanics, oceanic rogue waves can be described as surface gravity waves whose wave heights are much larger than the average sea state. Specifically, we characterise a 'rouge' wave as at least twice the size of the significant wave height, $H > 2H_s$, K. Dysthe, Krogstad and Müller (2008). The significant wave height is defined as four times the standard deviation, $H_s = 4\sigma$.

## 1.1 Literature Review

Trulsen, Zeng and Gramstad (2012) were the first to report experimental results showing an increased occurrence of rogue waves above a shoal. They performed several calculations including a confidence interval for estimated variance, autoskewness and autokurtosis as well as exceedance probability for three different experimental results of long-crested irregular waves propagating over a sloped bathymetry. The experimental data used in the publication came from MARIN in the Netherlands, Bunnik (2010). The results from all three experiments showed that there is a local maximum in autokurtosis as well as a local maximum in autoskewness near the shallow end of the slope. Moreover, they found that the location of the local maxima is also the location of the local maximal amplitude.

This research was continued by Gramstad et al. (2013) who implemented a standard one dimensional Boussinesq numerical model with improved linear dispersion. The Boussinesq model describes weakly non-linear and weakly dispersive waves in shallow water. Point estimates for autokurtosis and autoskewness as well as the probability for rouge waves were calculated for long-crested waves that propagate towards different non-uniform bathymetry profiles. The results showed that non-uniform bathymetry can provoke significantly increased autoskewness, autokurtosis and probability of rogue waves as a wave field propagates into shallower water. Furthermore, they showed that the increased risk of rouge waves is sustained over a distance in the shallow domain before it decreases and then stabilises. For some of the bathymetry profiles, there is a weak local minimum autoskewness and autokurtosis on the downhill slope. In addition, it was observed that the probability of rogue waves was intensified when the shallow regime was sufficiently shallow and the slope sufficiently steep. If the shallow regime becomes deep enough the local maxima disappear and we observe a gradual transition from one stable regime to another.

Trulsen, Raustøl et al. (2020) was the first publication to show that the surface elevation and velocity field behave differently as the wave field propagates over a shoal. Whilst the kurtosis of the surface elevation reaches a maximum over the shoal, the kurtosis of the horizontal velocity achieve a maximum on the lee side of the shoal. The publication reports the results of laboratory experiments performed by, Raustøl (2014), Jorde (2018), and Rye (2014). Their results indicate that there is a threshold depth for the extreme statistics over the shoal to appear. When the shoal is shallower than a threshold depth the autoskewness and autokurtosis over the shoal deviate from Gaussian statistics. The authors postulate that this depth may be $kh = 1.3$, yet admit that this threshold depth may depend on the steepness and bandwidth of the waves.

Zeng and Trulsen (2012) used a numerical model to study how slowly varying bathymetry changes the autoskewness and autokurtosis of weakly nonlinear,

irregular waves propagating from deeper to shallower water. The chosen numerical model was a nonlinear Schrödinger equation with variable coefficients and a shoaling term for slowly varying depths. They simulated three different wave fields with different Benjamin-Feir indices that propagated over five different slowly varying slopes. The dimensionless depth in the deep regime was kept as $kh = 10$, whilst the final dimensionless depth in the shallow regime was $kh = 1.2, 1.363, 2.065, 3.015, 4.003$ respectively. Their results showed that autokurtosis and autoskewness were reduced for shallower regimes and had a local minimum at the shallow end of the slope. After a given distance the statistical parameters stabilised to an equilibrium value.

Bitner (1980) explored non-linear effects of wind waves on shallow water by theoretical calculations and the comparison of these to experimental data. The publication assumes that surface waves have near Gaussian waves probability distribution and implemented the Gram-Charlier series distribution. She also assumes that the process is stationary, homogeneous and ergodic. She found that non-linear effects will affect the average wave height, period and the distribution in ways not predicted by linear theory. Additionally, the Gram-Charlier series distribution fit the experimental data well.

Cherneva et al. (2005) examined the ability of different probability density function to describe crests, troughs and heights of wind waves off the coast of Bulgaria. The field data was compared to three theoretical distributions of wave parameters proposed by Ochi (1998), Al-Humoud, Tayfun and Askar (2002), and Mori and Yasuda (2002). Cherneva et al. (2005) found that the occurrence of large wave crests and heights are under estimated by the theoretical models. Furthermore, the publication found that large values of autoskewness and autokurtosis lead to negative values for the crest and trough probability density function postulated by Al-Humoud, Tayfun and Askar (2002) and Mori and Yasuda (2002). This leads to the models being inapplicable for shallow regimes.

Grue (1992) did wave tank experiments with both rectangular and cylindrical shoals. The waves generated in the experiments had large wavelength compared to the depth of the tank. The publication utilises fully deterministic analysis. They found that the cylindrical shoal gave rise to higher harmonic free amplitude waves of on the far side of the shoal.

Beji and Battjes (1993) observed the time series and spectrum of waves propagating over a shoal. They used both JONSWAP and narrow-banded spectra. The shoal consisted of an uphill, a plateau and a downhill. The downhill was steeper than the uphill. They found that waves breaking did not have much effect on the shape of their spectra, even though the waves lost energy. The spectrum showed a clear difference between the frequencies of the generated waves and the frequencies resulting from non-linear interactions. From the time series we see that long wavelength monochromatic waves develop a sawtooth shape, loosing their previous symmetry. On the plateau triple resonance was observed. Then, the waves decoupled into smaller amplitude waves with near harmonic frequency as the energy redistributed toward a new equilibrium. For shorter wavelengths the effects were less pronounced.

To analyse wave propagating over a spherical or oval cylindrical shoal, T. Janssen, Herbers and Battjes (2008) developed a stochastic model. Of particular interest was the direction dependent evolution of the waves after the shoal. By

comparing their model to analytical and experimental data, they discovered that it performed well for a two-dimensional seafloor topography. The model precisely recreated the combination of wide angle refraction and diffraction from the seafloor topography.

T. T. Janssen and Herbers (2009) developed a frequency-angular spectrum model for waves in slowly varying mediums. They researched whether variables, such as ocean currents and varying bathymetry, can cause a focusing of wave energy increasing probability of extreme waves. They found that if the focusing effect is strong enough the waves are forced into an unstable state. This induces formidable deviations from Gaussian statistics and an increased probability of extreme waves. The authors observed that concomitant effects of non linearity and focusing may cause significant deviations from Gaussian statistics in already intensified sea states.

Sergeeva, Pelinovsky and Talipova (2011) studied the transformation of an irregular wave field propagating over shallow within the framework of a variable-coefficient Korteweg-de Vries equation. It applies to weakly non-linear and weakly non-dispersive was that propagate over variable depths. The authors performed two distinct numerical simulations with different initial steepness, $\epsilon = 5 \times 10^{-3}$ and $\epsilon = 1 \times 10^{-2}$. The waves propagated over a flat bathymetry, a sloped bathymetry that transitions from deep to shallow water and one that transitions from deep to shallow water. The deeper regime had a dimensionless depth of $kh = 0.44$, where as the shallower regime had dimensionless depth of $kh = 0.3$. The publication showed that there is an increased probability of rogue waves when depth decreases and stated that this process is characterised by the initial wave steepness.

Viotti and Dias (2014). They utilised numerical simulations of the Euler equation to show that autoskewness and autokurtosis is largest near the start of the plateau using numerical simulations of the Euler equations. The probability distribution showed that the autoskewness of wave became larger for a shallower plateau. The shape of the spectrum at the start of the plateau was in line with Phillips $\omega^{-5}$ power-law for the stronger depth transitions.

Kashima, Hirayama and Mori (2014) investigated waves propagating in a wave tank over changing depth, going from deep to shallow. They did both experiments and numerical simulation employing the Boussinesq equations. They generated waves with different JONSWAP spectra altering the wave height and peak enhancement factor, $\gamma$. They noticed a change in wave behavior at the water depth threshold value $k_p h = 1.363$. For values of $k_p h < 1.363$ the kurtosis and skewness increased rapidly, while for $k_p h > 1.363$ the skewness remained near constant and the kurtosis continued to grow. For a flat bottom the kurtosis was dependent on the wave height and increased with distance from the wave source for $\gamma < 1$. This behavior was not as pronounced for the skewness. They concluded that the Boussinesq equations did not sufficiently describe the behavior seen in the experiments. Specifically, the equations did not produce the same occurrence of freak waves seen experimentally. This is because their Boussinesq equation did not account for third order non-linear effects, which the authors believed to be causing the increase in kurtosis for $k_p h < 1.363$.

Yu et al. (2014) did experiments with a shoal consisting of an uphill, a pleateau

and a downhill. The waves generated had a JONSWAP spectrum with different values of $\gamma$. Their experiments showed that a $\gamma$ value of 3.3 resulted in the highest probability of freak waves and that the most vulnerable location was the last part of the uphill. This same location had the largest skewness and kurtosis. They also investigated the relationship between the skewness and kurtosis. Here, they found a parabolic dependence fist shown in Mori and Kobayashi (1999).

## 1.2 Research Scope

This master thesis studies the results of two different experiments that we conducted at the Hydrodynamics Laboratory of the Department of Mathematics at the University of Oslo. Experiment 1 is inspired by K. B. Dysthe et al. (2003) and has a wave spectra designed to hopefully induce modulation instability and nonlinear effects, but with a uniform bathymetry. Experiment 2 is motivated by Trulsen, Raustøl et al. (2020). It has a stable wave spectra and an interesting non-uniform bathymetry.

We implement techniques commonly found in mathematical finance and quantitative risk management in order to study how altering the wave spectra, or the bathymetry, can impact rogue wave statistics.

We perform an analysis of the higher order automoments of the surface elevation of experiment 2 as well as studying the evolution of the power spectral density of the surface elevation as the process propagates.

For experiment 3 we study typical mechanical parameters, the higher order automoments of the surface elevation and velocity field and the comoments of the surface elevation and velocity field. Moreover, we compare the normal distribution with the probability density function of the surface elevation and the probability density function velocity field. Lastly, we study the dependence structure of the surface elevation and velocity field using a Copula.

## 1.3 Outline

The rest of the text is organised as follows:

**Chapter 2** provides a brief introduction to the background mathematics necessary for the full enjoyment of this thesis.

**Chapter 3** establishes key terms and concepts within Stochastic analysis used study the experimental data.

**Chapter 4** outlines wave theoretical foundations including the anatomy of a wave, dimensionless numbers and wave parameters as well as the concept of a wave spectra. Furthermore, the chapter describes narrow-banded spectra and modulation instability.

**Chapter 5** describes the theorectical framework surrounding the experimental equipment used in the measurements of surface elevation and velocity field.

**Chapter 6** discusses the 'prelab' work including specifying the different timeseries that run the wave maker, choosing the length of each experimental run, deciding on an appropriate quiescent surface level and peak period. Furthermore, this chapter discusses ADV placement and equipment synchronisation.

**Chapter 7** outlines the experimental set-up and methodology for each of the three different experiments. Furthermore, it provides a comprehensive overview of the different techniques used to post process the data.

**Chapter 8** presents the results of experiment 1, which studies the effects of modulation instability on narrow banded spectra. The analysis is done in two parts. The first analysis studies how statistical moments evolve in spaces as the wave process propagates along the tank. The second analysis shows how the wave spectra changes as the wave process propagates along the tank.

**Chapter 9** displays the results of experiment 2, which studies the effects of non-uniform bathymetry.

**Chapter 10** discusses the results.

**Chapter 11** concludes the thesis.

**Appendix A** contains additional results not deemed interesting enough for the main thesis.

**Appendix B** shows tests used to verify the validity of the experimental setup.

**Appendix C** discusses univariate and multivariate Hilbert transforms. As a result of time constraints, this theory was not applied to the experimental data.

**Appendix D** includes bits of code used for postprocessing and analysis.

# PART I

## Theory

<div align="center">

# CHAPTER 2

</div>

---

<div align="center">

# Background Mathematics

</div>

---

## 2.1 The distinction between Multivariate and Multidimensional

This thesis aims to describe the multivariate, multidimensional wave processes. It is vital to clarify the difference between the terms multivariate and multidimensional. Let U and V be two scalar processes that depend on three coordinates, time and two spatial coordinates such that

$$U(x, y, t) \quad \text{and} \quad V(x, y, t).$$

We can now describe the bivariate, tridimensional process

$$\{U, V\}(x, y, t). \tag{2.1}$$

The term "multivariate" refers to multiple scalar processes, whilst multidimensional refers to multiple coordinates.

## 2.2 Cauchy Principal Value

Cauchy principal value is a technique used to solve improper integrals, which would otherwise remain undefined, by approaching the singularity from both sides with the same speed. The common notation, which is used in this thesis is

$$P \int f(x) \, \mathrm{d}x.$$

If $f(x)$ has a singularity in the interval over which the integral is being evaluated, then Cauchy principal value takes the form,

$$P \int_{\alpha}^{\beta} f(x) dx = \lim_{\varepsilon \to 0} \left[ \int_{\alpha}^{t-\varepsilon} f(x) dx + \int_{t+\varepsilon}^{\beta} f(x) dx \right], \tag{2.2}$$

where $f(x)$ has a singularity at $x = t$, King 2009a.

## 2.3 Discrete Fourier Transform

We would like to express a finite complex sequence with N elements $\{f_j : j = 1, 2, \cdots N\}$ as a superposition of the basis function $\{e^{\frac{2\pi i j n}{N}} : j = 1, 2, \cdots N\}$.

This can be expressed as

$$f_j = \sum_{n=1}^{N} \hat{f}_n e^{\frac{2\pi i j m}{N}}.$$

(2.3)

Since the basis functions are orthogonal, $\langle e^{\frac{2\pi i j n}{N}}, e^{\frac{2\pi i j m}{M}} \rangle = N\delta_{n,m}$ where $\delta_{n,m}$ is the Kronecker delta, the discrete Fourier transform becomes

$$\hat{f}_n = \frac{1}{N} \sum_{j=1}^{N} f_j e^{-\frac{2\pi i n j}{N}}.$$

(2.4)

# CHAPTER 3

## Stochastic Analysis

### 3.1 Statistical foundations

Colloquially a random variable is a variable whose value depends on the outcome of random phenomena. Formally, a stochastic variable $X$ is a function that maps a set of possible outcomes $\Omega$ to a measureable space E, $X : \Omega \to E$. If X is real valued, then $X : \Omega \to \mathbb{R}$.

The probability distribution or probability density funtion (pdf) of a continous random variable $X$ is a function such that for any two numbers a and b with $a \leq b$, Devore, Berk and Carlton (2012), we have

$$P(a \leq X \leq b) = \int_a^b f(x) \ \mathrm{d}x. \tag{3.1}$$

A probability density function must satisfy:

1. $f(x) \geq 0 \quad \forall x,$

2. $\int_{-\infty}^{\infty} f(x) \ \mathrm{d}x = 1.$

The cumulative distribution function for a random variable X describes the probability $P(X \leq x)$ for a given value x. We define the cumulative distribution function (CDF) $F(x)$, as

$$F(x) = P(X \leq x) = \int_{-\infty}^{x} f(y) \ \mathrm{d}y. \tag{3.2}$$

A cumulative distribution function has the properties

1. $F(-\infty) = 0,$

2. $F(\infty) = 1,$

3. F(X) is monotonically increasing function.

## 3.2  Common statistical distributions and their properties

A normal distribution or Gaussian distribution is continuous probability density function for a real-valued random variable. The general form of a normally distributed pdf is

$$f(x) = \frac{1}{\sigma\sqrt{2\pi}} e^{-\frac{1}{2}\frac{(x-\mu)^2}{\sigma^2}}, \tag{3.3}$$

where $\mu$ is the mean and $\sigma$ is the standard deviation.

The chi distribution is the distribution of the Euclidean distance of normally distributed random variables from the origin. If $\{X_i : i = 1, ..., k\}$ are normally distributed with mean, $\mu = 0$ and standard deviation, $\sigma = 1$ then the static

$$Y = \sqrt{\sum_{i=1}^{k} X_i^2}, \tag{3.4}$$

is Chi distributed. The parameter k, that describes the number of random variables, specifies the degrees of freedom of the distribution.

A Chi distribution with two degrees of freedom is called a Rayleigh distribution with the requirement that it only applies for non negative number, $X > 0$ otherwise the distribution is zero. The probability density function of a Rayleigh distribution has the form

$$f(x; \alpha) = \frac{x}{\alpha^2} e^{-x^2/2\alpha^2}. \tag{3.5}$$

## 3.3  Moments and Comoments

The expected value, mean or first moment for a discrete random variable with a finite set of possible outcomes, is a weighted average of all possible outcomes, $x_i$, where the weights are the corresponding probabilities, $p_i$. Thus the expected value is given by

$$\mu = \mathrm{E}[X] = \sum_{i=1}^{\infty} p_i x_i. \tag{3.6}$$

If we consider a continuous random variable X with a pdf $f(x)$ then the expectation is given by

$$\mu = \mathrm{E}[X] = \int_{-\infty}^{\infty} x f(x) \, \mathrm{d}x. \tag{3.7}$$

The expected value of a function is given by

$$\mu = \mathrm{E}[g(X)] = \int_{-\infty}^{\infty} g(x) f(x) \, \mathrm{d}x. \tag{3.8}$$

The second central moment is the variance, which measures how a set of numbers is dispersed from their average value.

$$\sigma^2 = \mathrm{Var}[X] = \mathrm{E}[(X - \mu)^2]. \tag{3.9}$$

The square root of the variance is the standard deviation.

$$\sigma^2 = \sqrt{\sigma}. \tag{3.10}$$

Skewness measures the level of asymmetry of a real-valued distribution around the mean,

$$\gamma = \frac{\mathrm{E}[(X - \mu)^3]}{\sigma^3}. \tag{3.11}$$

A rule of thumb is that if the skewness is between $\gamma = 0.5$ and $\gamma = -0.5$ we characterise the distribution as fairly symmetrical. If the skewness is between 0.5 and 1 or between between $-0.5$ and $-1$ the distribution is moderately skewed and if the skewness is above 1 or below $-1$ the distribution is heavily skewed.

Additionally if $\gamma < 0$ then the mass of the distribution is concentrated on the left with the right tailed drawn out. If $\gamma > 0$ then the mass of the distribution is concentrated on the right with the left tailed drawn out.

Kurtosis measures how 'heavy' the tails of a distribution are. In other words it describes how many or how extreme the outliers of a distribution are,

$$\kappa = \frac{\mathrm{E}[(X - \mu)^4]}{\sigma^4}. \tag{3.12}$$

If $\kappa > 3$ the distribution is leptokurtic and has fatter tails or more outliers. If $\kappa < 3$ the distribution is platykurtic and has thinner tails or less outliers. If $\kappa = 0$ the distribution is mesokurtic.

## Comoments

The correlation used in this thesis is the Pearson correlation coefficient which is defined as the covariance between two variables divided by the product of their standard deviations

$$\rho_{X,Y} = \frac{\mathrm{COV}(X, Y)}{\sigma_X \sigma_Y} \tag{3.13}$$

The covariance is defined as

$$\mathrm{COV} = \mathrm{E}[(X - E[X])(Y - E[Y])] \tag{3.14}$$

Correlation and covariance describe the linear relationship between two variables.

Coskewness describes the asymmetry of the simultaneous distribution of random variables. If two random variables are positively co-skewed then the exhibit positive asymmetry simultaneously. Naturally the reverse is true for negative coskewness, Miller 2013. For random variables X and Y coskewness can be expressed as,

$$\gamma_{2,1}(X, X, Y) = \frac{\mathrm{E}[(x - E[X])^2(y - E[Y])]}{\sigma_x^2 \sigma_y}, \tag{3.15}$$

$$\gamma_{1,2}(X, Y, Y) = \frac{\mathrm{E}[(x - E[X])(y - E[Y])^2]}{\sigma_x \sigma_y^2}. \tag{3.16}$$

Cokurtosis determines whether the tails of a simultaneous distribution contains more or less extreme values, i.e. outliers. A high cokurtosis describes a distribution that contains more outliers and is therefore 'thicker-tailed'. A simultaneous distribution with a lower cokurtosis can be described as 'thinner-tailed', Miller 2013.

$$\kappa_{2,2}(X, X, Y, Y) = \frac{\mathrm{E}[(x - \mathrm{E}[X])^2 (y - \mathrm{E}[Y])^2]}{\sigma_x^2 \sigma_y^2}, \tag{3.17}$$

$$\kappa_{3,1}(X, X, X, Y) = \frac{\mathrm{E}[(x - \mathrm{E}[X])^3 (y - \mathrm{E}[Y])]}{\sigma_x^3 \sigma_y}, \tag{3.18}$$

$$\kappa_{1,3}(X, Y, Y, Y) = \frac{\mathrm{E}[(x - \mathrm{E}[X])(y - \mathrm{E}[Y])^3]}{\sigma_x \sigma_y^3}. \tag{3.19}$$

Kurtosis is a special case of Cokurtosis where there is only one random variable. To make this distinction clear we will use the term autokurtosis to describe a kurtosis calculation with one random variable. The autokurtosis of a univariate Gaussian normal distribution is 3. If a univariate distribution has an autokurtosis greater than 3 then the distribution is said to be 'leptokurtic'. If a univariate distribution has an autokurtosis less than 3 it is said to be 'platykurtic'.

### Convergence of moments

The estimators of the statistical moments converge at the rate of

$$\sqrt{\frac{C}{N}}, \tag{3.20}$$

where C is a moment-specific constant, equal to 1 for estimating the mean, 2 for the standard deviation estimate, 6 for the autoskewness estimate and 24 for the autokurtosis estimate. N is the sample size. This estimator requires all samples are independent.

## 3.4  Stochastic processes

A stochastic process describes how random phenomena evolve in time. Formally, a stochastic process is a set of stochastic variables, $\{X(t) : t \in T\}$, where at every time t in the set T, we obtain a random variable X(t). If the set T is countable or finite it is a discrete-time process. If the set T is not finite or countable we have a continuous time process. We can define the expected value as

$$\mu(t) = \mathrm{E}[X(t)] = \int_{-\infty}^{\infty} x f(x, t) \, \mathrm{d}x. \tag{3.21}$$

Moreover, we can define the autocorrelation function for a stochastic process as

$$R[X(t_1)X(t_2)] = \int_{-\infty}^{\infty} x_1 x_2 f(x_1, x_2, t_1, t_2) \, \mathrm{d}x_1 \, \mathrm{d}x_2. \tag{3.22}$$

13

The second moment of a stochastic process is also called the *mean power*, and can be defined by

$$R(t, t) = \text{E}[|X(t)|^2]. \tag{3.23}$$

A weekly stationary process is a stochastic process where the expected value is independent of time, $\text{E}[X(t)] = \mu$ and the autocorrelation function only depends on the time difference, $\tau = t_2 - t_1$. We have

$$R(t_1, t_2) = \text{E}[X(t_1)X(t_2)] = R(\tau).$$

## 3.5  Copulae

The term copula comes from the Latin word for link ,'copulare', and was coined by Sklar (1959). In essence a Copula is a multivariate cumulative distribution function for which the marginal probability distribution function of each of its component variables is uniformly distributed from $[0, 1]$. For an entertaining introduction to the subject see Mikosch (2005) and Genest and Rémillard (2006), best read in that order.

The main purpose of copulas is to describe the dependence or inter-correlation between random variables. Consider a set of random variables $\{X_i : i = 1, \cdots, n\}$ where each random variable is described by its cumulative distribution function, CDF such that

$$F_i(x) := P(X_i \leq x). \tag{3.24}$$

The different CDFs are often referred to as marginals. These marginals provide us with no understanding of the joint behaviour of the different random variables i.e. if the variables are independent, the joint distribution is the product of the separate CDFs,

$$P(X_1 \leq x_1, X_2 \leq x_2) = F(x_1) \cdot F(X_2). \tag{3.25}$$

The goal of Copulas is to disentangle the marginal distributions and dependence structure so that we can fully describe the behaviour of $X_1$ and $X_2$ together.

**Definition 3.5.1** (Schmidt 2007)**.** A d-dimensional copula $C : [0, 1]^d :\to [0, 1]$ is a function which is a cumulative distribution function with uniform marginals.

By requiring a Copula to be a distribution function we get several properties

- The copula is equal to zero if any of its arguments are zero, $C(u_1, u_2, \cdots u_{i-1}, 0, u_{i+1}, \cdots u_d) = 0$.

- The marginal $u_i$ can be obtained by setting $u_j = 1, \quad \forall j \neq i$, $C(1, 1, \cdots u_i, 1, 1, \cdots 1) = u_i$.

Sklar´s theorem provides the theoretical foundation for the application of copulas and states that if we chose a copula and entangle it with some marginal distributions we can end up with a fully fledged multivariate distribution function.

**Theorem 3.5.2** (Sklar´s Theorem). *Sklar 1959*
*Let $F(x)$ and $F(y)$ be marginal cumulative distribution functions of two random variables $x$ and $y$ such that $F(x) = P(X \leq x)$ and $F(y) = P(Y \leq x)$. Let $F(x,y)$ be a joint cumulative distribution function $F(x,y) = P(X \leq x, Y \leq x)$, then $F(x,y)$ is linked to $F(x)$ and $F(y)$ through a copula such that*

$$F(x,y) = C(F(x), F(y)). \tag{3.26}$$

There are several different families of Copulae. This thesis tested three different copulas. Gaussian, t and Gumbel copulas. Suppose we have two random variables that have the correlation matrix

$$\sum = \begin{bmatrix} 1 & \rho \\ \rho & 1 \end{bmatrix}, \tag{3.27}$$

then the Gaussian Copula is given by

$$C_R^N(X) = \Phi_R(\Phi^{-1}(u_1) \cdots \Phi^{-1}(u_d)), \tag{3.28}$$

where $\Phi^{-1}$ is the inverse cumulative distribution function of a standard normal and $\Phi_R$ is the joint cumulative distribution function of a multivariate normal distribution.

Futhermore, the t-copula or 'Student' copula is given by

$$C_{\nu,\sum}^t(X) = t_{\nu,\sum}(t_\nu-1(u_1) \cdots t_\nu-1(u_d)), \tag{3.29}$$

where $\sum$ is the correlation matrix, $t_\nu$ is the CDF of a one dimensional student $t_\nu$ distribution and $t_{\nu,\sum}$ is the CDF of a multivariate $t_{\nu,\sum}$ distribution

The Gaussian and t copulae are derived from multivariate distributions and as a result there are no simple analytical formulas for the copula functions. Conversely, there are some copulas that can by stated directly and often fall into the category of Archimedean copulas. The Gumbel copula or Gumbel - Hougaard copula is used in thesis thesis fall into this category, and is given of the form

$$C_\theta^{Gu}(u_1, u_2) = \exp\left[-((-\ln u_1)^\theta + (-\ln u_2)^\theta)^{\frac{1}{\theta}}\right], \tag{3.30}$$

where $\theta \in [1, \infty)$.

## Tail dependence

Copulas model dependence structure on a *quantile* scale, making them useful for identifying dependence structure of extreme outcomes. In simple terms if variables have tail dependence then there is more of a tendency for $X_2$ to be extreme when $X_1$ is extreme and vice versa, McNeil, Frey and Embrechts (2015).

This thesis utilises three different copulae of model the dependence structure between the surface elevation and velocity field. The first is a Gaussian copula which has no tail dependence i.e. there is no change in relationship for extremely

large or extremely small values.  The second is a Gumbel copula which has positive tail dependence indicating that there is more of a tendency for $X_2$ to have extreme large values when $X_1$ has extreme large values and vice versa.  The third copula is a T-copula which has both positive and negative tail dependence of the same magnitude.

## Akaike information criterion

To select which Copula best describes our data we utilise the Akaike information criterion, AIC.  Let $k$ be the number of estimates parameters and let $\hat{L}$ be the maximum of the likelihood function of the model.  The AIC is given by

$$AIC = 2k - 2\ln(\hat{L}). \tag{3.31}$$

For our three copulae, the preferred model is the one that minimises the AIC.

# CHAPTER 4

# Wave Theory

## 4.1 Anatomy of a wave

The surface elevation of a wave, $\eta(t)$, describes the position of the water surface that limits the free air. The equilibrium surface elevation or quiescent surface is the water level when the water is at rest.

The frequency $f$, angular frequency $\omega$, and wavenumber $k$ are given by,

$$f = \frac{1}{T}, \quad \omega = \frac{2\pi}{T} \quad \text{and} \quad k = \frac{2\pi}{\lambda}. \tag{4.1}$$

The wave period is given by T, and the wavelength by $\lambda$.

A wave crest is the local maxima of the surface elevation function, i.e. the points at which the wave exhibits the maximum amount of displacement from the quiescent surface. Conversely, the wave troughs are the local minimums of the surface elevation.

In an inhomogeneous wave field the wave height can vary wildly. Therefore, we describe the significant wave height as four times the standard deviation of the wave process,

$$H_s = 4\sigma. \tag{4.2}$$

In this thesis we choose to follow K. Dysthe, Krogstad and Müller (2008)'s classification of a rogue wave, which states that a rogue wave must have a wave height larger than two times the significant wave height,

$$H > 2H_s = 8\sigma. \tag{4.3}$$

## 4.2 Dimensionless Parameters and Wave Properties

The characteristic wave steepness, $\epsilon$, of a wave field is given by

$$\epsilon = k_c a_c, \tag{4.4}$$

where $k_c$ is the characteristic wavenumber and $a_c$ is the characteristic amplitude. Wave steepness is linked to the non-linearity of the waves. Greater steepness indicates that the waves are displaying more nonlinear tendencies.

There are many ways to define the characteristic wavenumber. In this thesis, the characteristic wavenumber $k_c$ is chosen to be the peak wavenumber $k_p$. Peak wavenumber is the wavenumber that corresponds to the maximum angular frequency, of peak frequency, $\omega_p$ and can be found using the dispersion relation for surface gravity waves

$$\omega_p = \sqrt{gk_p} \tanh k_p h. \tag{4.5}$$

The amplitude of a wave is often understood as a constant for the whole wave train. However, in an irregular wave train the crest height is not constant. The crest height can be negative and the trough depth can be positive. The wave height is the distance between neighbouring wave crests and troughs. Therefore we aim to define a characteristic amplitude as

$$a_c = \sqrt{2}\sigma, \tag{4.6}$$

where $\sigma$ is the standard deviation of the surface elevation.

The Ursell Number, abbreviated Ur, describes the non-linearity of long surface gravity waves. It is defined as

$$\text{Ur} = \frac{a_c k_p}{(k_p h)^3}. \tag{4.7}$$

The dimensionless depth is given by $k_p h$, and is traditionally used to define deep water, $k_p h \gg 1$, and shallow water, $k_p h \ll 1$.

## 4.3 Stokes waves

The surface elevation function, $\eta$, and velocity field potential, $\phi$, for second-order Stokes waves in finite depth are

$$\eta = a\cos(kx - wt) + \frac{2 - \tanh^2 kh}{4\tanh^4 kh} ka^2 \cos 2(kx - wt) \tag{4.8}$$

and

$$\begin{aligned}
\phi = &\frac{\omega a}{k} \frac{\cosh(k(y+h))}{\sinh(kh)} \sin(kx - \omega t) - \frac{\omega^2(1 - \tanh^2 kh)}{4\tanh^3 kh} t \mid a \mid^2 \\
&+ \frac{3\omega a^2(1 - \tanh^2 kh)}{4\tanh^3 kh} \frac{\cosh(2k(y+h))}{\sinh(2kh)} \sin 2(kx - \omega t).
\end{aligned} \tag{4.9}$$

## 4.4 Wave Spectra

When observing the sea surface we notice that it is not described by a simple sinusodial. The ocean fascinates us because it is composed of waves of different lengths and periods. When storms roar the ocean may unleash its ferocity and on other days, the ocean may be calm and gentle. Different sea states must be represented differently.

To be able to represent the complexity of the sea surface we introduce the concept of a wave spectrum. The wave spectrum gives us the distribution of

wave energy among different wave frequencies of wave-lengths on the ocean surface.

Using a Fourier expansion we can represent the ocean surface as an infinite series of sine and cosine functions of different wave-lengths moving in any direction. Since wave-lengths and wave frequencies are connected through the dispersion relation, we can represent the ocean surface as an infinite sum of sine and cosine functions of different frequencies moving in any direction.

The implication of using infinite Fourier series is that we can represent an inhomogenous wave field as a superposition of monochromatic waves. We choose to define

$$\eta(x,t) = \sum_n \sqrt{2S(\omega_n)(\Delta\omega)_n} \cos{(k_n x - \omega_n t + \Theta_n)}, \qquad (4.10)$$

where $S(\omega_n)$ is the wave spectra, $(\Delta\omega)_n$ is the distance between to neighbouring frequency components and $k_n$ represents the wavenumber associated with the angular frequency $\omega_n$ by a dispersion relation. Moreover, $\Theta_n$ is a phase angle which is uniformly distributed from $[0, 2\pi)$.

We demand that $\eta$, in Equation (4.10), must reproduce a desired wave spectrum. However, there is no specific reason that $\Theta$ should have a certain probability distribution, it is not necessarily the case that the phase angles must be uniformly distributed. Nor is it the case that $S(\omega_n)$ needs to be deterministic. Another option might be to use a stochastic variable that has expectation $S(\omega_n)$ with a probability distribution that is sometimes assumed to be Rayleigh.

The choice of Equation (4.10) is made on the basis of two different considerations, to reconstruct the desired spectrum and provide an acceptable probability distribution. In that case, deterministic $S(\omega_n)$ and uniform $\Theta_n$ are a typical choices.

## Pierson - Moskowitz Spectrum

We can use various different idealized wave spectra to describe the different sea states and other properties. The Pierson - Moskowitz spectrum describes a sea state where the wind has steadily blown over the a large ocean area for a long time. The waves come into an equilibrium with the wind. This is called fully developed sea.

To develop the spectrum Pierson Jr and Moskowitz (1964), they studied wave measurements made by accelerometers placed on weather ships in the North Atlantic after the wind had blown, steadily, for a long time over a large area. The formula derived from the experiments defines the spectrum as

$$S(\omega) = \frac{\alpha g^2}{\omega^5} \exp\left(-\beta(\frac{\omega_o}{\omega})^4\right), \qquad (4.11)$$

where $\alpha$ is an amplitude factor, $\omega_p$ is the frequency is the most energy, and $g$ is acceleration due to gravity.

**JONSWAP Spectrum**

By analysing data from the Joint North Sea Wave Observation Project (JONSWAP). K. Hasselmann et al. (1973) , found that the ocean is rarely fully developed. Non-linear interactions effect the sea surface for a very long time and over great distances. Therefore, to increase the the fit to their measurements, they multiplied the Pierson-Moskowitz spectrum by a peak enhancement factor, $\gamma$ and created what is now known as the JONSWAP spectrum,

$$S(\omega) = \frac{\alpha g^2}{\omega^5} \exp\left(-\beta(\frac{\omega_o}{\omega})^4\right) \gamma^r, \tag{4.12}$$

where $r$ is defined as

$$r = \exp\left[-\frac{(\omega - \omega_p)^2}{2\sigma^2\omega_p^2}\right]. \tag{4.13}$$

**Gaussian Spectrum**

A Gaussian wave spectrum will then have the form,

$$S(\omega) = \frac{1}{\sigma\sqrt{2\pi}}e^{-\frac{(\omega-\mu)^2}{2\sigma^2}}. \tag{4.14}$$

The Gaussian wave spectrum has several benefits, one of the them being that it is fairly simple to create a narrow-banded Gaussian spectrum by letting $\sigma$ be very small. In this instance, $\sigma$, is not the standard deviation.

## 4.5 Narrow Banded process

A narrow banded process has a spectrum with a small bandwidth. Simply put, the spectrum includes only a narrow range of frequencies. There are many ways to estimate bandwidth. We choose to define the bandwidth as half the width of a line drawn at half the maximum amplitude

$$\delta = \frac{HPHW}{\omega_p}. \tag{4.15}$$

## 4.6 Modulation Instability

Modulation instability is the phenomenon where small deviations from periodic waveforms are strengthened by nonlinearity which leads to the generation of spectral tails T. Benjamin and Feir (1967).

There is a plethora of research on modulationally unstable surface gravity waves. The original articles on Benjamin-Feir instability are T. B. Benjamin (1967), Feir (1967), G. Whitham (1967),G. B. Whitham (1967), and Hasimoto and Ono (1972). An important result of the research in these papers, is the finding that a Stokes wave is modulationally unstable for long crested perturbations for depths, $kh > 1.363$. Note that short crested perturbations will still be unstable even for shallower regimes, $kh > 1.363$. The results in publications above are

calculated using perturbation theory using Schrödinger equations or similar equations.

J. McLean et al. (1981) and J. W. McLean (1982) did numerical calculations using the Euler equations and confirmed the results of the perturbation analysis, and extended the validity of the analysis to greater steepness and bandwidths.

The results above are limited to Stokes waves which are distinguished by have a bandwidth, $\delta = 0$. If we extend our discussion to Stokes waves with a wave spectrum with a finite bandwidth, $\delta > 0$. The question is whether the such a spectrum is stable. This was originally analyzed by using the Schrödinger equation, Alber and P. Saffman (1978) and Alber (1978) and the Zakharov equation Crawford, P. G. Saffman and Yuen (1980).

Alber (1978) derived a stability criterion that was named the Benjamin-Feir Index by P. A. Janssen (2003)

$$\text{BFI} = \alpha \frac{\epsilon}{\delta},\tag{4.16}$$

where $\epsilon$ is the wave steepness, $\delta$ is the bandwidth, and $\alpha$ is a constant. Alber (1978) shows that if the ratio between the bandwidth and the steepness becomes too large, $\delta > \alpha\epsilon$, then the spectrum is stable.

# PART II

# Experiments

# CHAPTER 5

## Experimental Equipment

### 5.1 Measuring the surface elevation

To conduct surface elevation measurements, $\eta$, we used an ultra sound system from General Acoustics.

The system can make up to four independent measurements simultaneously, each independent measurement corresponds to a channel. Furthermore, each channel can receive data from one to three senors.

The user manual, General Acoustics 2013, states that one channel is more than sufficient to measure waves with low steepness, while for waves with greater steepness results may be improved with a setup with more ultra sound probes per channel.

A fixed reference sensor measures the speed of sound used to measure the distances. The sensors we used have the following settings:

- Ultrasound probe type: USS02/ HFP.

- Samplerate: 125/250 Hz.

- Measurement range: 30 - 250 mm.

- Superior resolution: 0.18 mm.

- Accuracy: $\pm 1$ mm.

The data collected from the sensors is processed by an Ultralab Advanced Controller which converts the data in to meters. Then it sends the converted data to a PC which uses a software, Ultralab: Ultralab Monitoring Software, to record and display the data.

### 5.2 Measuring the velocity component

We used a vectrino, an acoustic Doppler velocimeter (ADV) from Nortek, to measure the different velocity components in the wave field. The ADV we used has a separated transmitter and receiver allowing it to detect velocities in three dimensions.

The center transmitter emits pairs of pulses of high-frequent sound, 10 MHz. The ADV software sets a known time difference between the pulses and seeded particles, a known distance in front of the center probe reflects the sound. Four receivers accumulate sound that is returned with a Doppler-induced phase shift and the measured phase shift is converted to velocity. The receivers work in pairs, with two receivers per axis. It is argued that measuring the phase shift is more accurate than using a direct Doppler frequency technique to measure velocity.

We are able to measure four different velocity components, X, Y, Z1 and Z2. It should be noted that we use capital letters for the ADV's coordinate system. Z1 and Z2 are two different measurements from two different receiver pairs of the velocity along the ADV's center probe. Nortek often refers to this as the ADV´s vertical axis. Due to the way in which the ADV is constructed, this is the axis which is measured most accurately.

The ADV has several different settings that must be determined by the user

- Sampling rate [Hz].

- Transmit length.

- Nominal velocity range $[\frac{m}{s}]$.

- Sampling volume.

- Power level.

The *sampling rate* defines the number of samples per second. A high sampling rate leads to a high time resolution at the cost of lower accuracy.

The *transmit length* determines the transmit pulse length.

The *Nominal velocity range (NVR)* determines the time lag between to pulses in a pulse pair. A low NVR produces a greater lag between pulses. If the NVR is set to high, the data quality will decrease as the signal will be polluted with too much "noise". However, a too low NVR will induce phase ambiguity where the data appears to unrealistically and abruptly vary, often including a sign change. The vertical component, Z1 and Z2, has a greater sensitivity than the other components, however, this also means that it has a lower maximum NVR. A rule of thumb given by, CITATION, is to set the lowest possible NVR without risking that the data quality will suffer.

According to the ADV manual, the measurement volume is located 50mm in front of the center probe. Its form, although irregular, can be approximated to a cylinder with a 6mm diameter and 2.5 - 8.5mm length, depending on the chosen size of the *sampling volume*. A greater sampling volume produces more accurate results.

Choosing a higher power level provides more accuracy, but uses more electricity.

## Output

In addition the four velocity components, the ADV also returns performance indicators used for error evaluation:

- 'Correlation measures' the similarity in the data collected by the two receivers in a receiver pair. The measured correlation should be above 90%.

- 'Signal - to - noise ration' (SNR) [dB] measures the ratio between the accoustic signal and the background noise. The quality of the measurements increases with an increasing SNR to an SNR around 15 or 20. Over this threshold the SNR does not impact quality of the data measurements. To obtain a high SNR it is vital to ensure that there are enough seeding particles in the tank.

- 'Amplitude' counts the number of amplitudes the ADV measures per measurement. It is a measure of signal strength, however, it is not as useful as the other two performance indicators.

The results from every run are saved in a *.vno* file and converted into a *.hdr* file containing meta-data, and *.dat* file containing the velocity components and the performance indicator measurements.

In order for the ADV to work, there must be seeded particles in the tank so that the emitted pulses can be reflected back towards the receivers. Nortek recommends a particle concentration of 20-30 mg/L however the SNR is an apt indicator of whether or not the tank is adequately seeded. We used Norteks own seeding material designed for ADVs in laboratory environments.

### Systematic error

ADVs are often viewed as a non-intrusive measuring technique as the sampling volume is located a known distance away from the device. However, it has been shown that the high frequent sound emitted by the ADV induces a current in the area in front of the center probe which is also the sampling volume, and therefore it produces a systematic error. The article by Poindexter, P. Rusello and Variano (2011) lists current strength compared to the other ADV parameters making it possible to compensate for the generated systematic error.

# CHAPTER 6

# Pre-lab

## 6.1 The wave maker

There is a direct relationship between the Fourier coefficients of the wave maker paddle motion and the Fourier coefficients of surface elevation Newman 2018. This thesis used two different spectra, Gaussian and Pierzon - Moskowitz, to create time series that control the movement of the wave maker paddle. The some of the code used can be found in the appendices.

To determine the frequency resolution, N, we assume that the skewness and kurtosis of the surface elevation will converge at the same N as the skewness and kurtosis of the wave maker paddle signal. We chose N = 3000 as this is the lowest N that insures convergence of kurtosis whilst minimising calculation time.

We know that

$$S(\omega_n) \to 0 \quad \text{when} \quad \frac{\omega_n}{\omega_p} \to 0, \infty.$$

This means that very small or very large values of $\frac{\omega_n}{\omega_p}$ will not contribute significantly to the wave motion. Hence, we have chosen only to include frequencies such that

$$S(\omega_n) \geq \frac{S(\omega_p)}{500}.$$

## Gaussian

We used a narrow banded Gaussian spectra, Figure 6.1, with a $\omega_p = 6.2832$ and a range of frequencies between $5.1958 \leq \omega_n \leq 7.3747$.
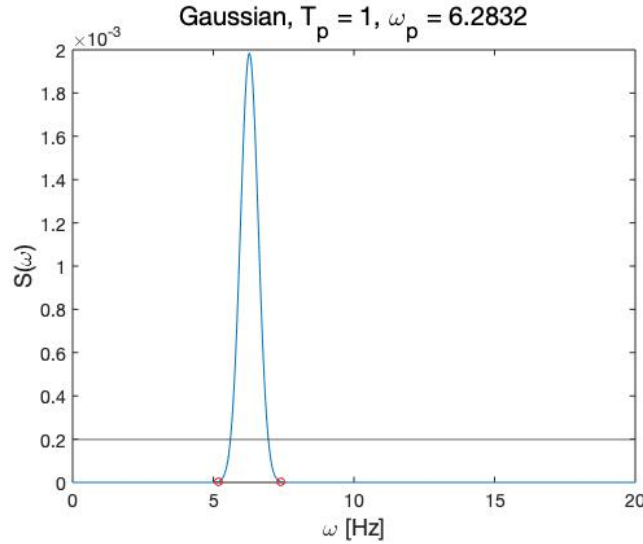


Figure 6.1: Gaussian Spectrum with a range of included frequencies between $5.1958 \leq \omega_n \leq 7.3747$.

We created two different time series from the Gaussian spectra. The first has an amplitude factor of 0.05 and is called Gaussian1. The second has half the amplitude factor, 0.025 and is called Gaussian2. Although they have the same shape, bandwidth and peak frequency they have to be generated separately.

Figure 6.2 is a histogram displaying frequency distribution of Gaussian 1 compared to a theoretical Gaussian spectrum. We observe that the time series is not perfectly distributed with some frequency bins above expected values and some below the expected values. Similarly we see from, Figure 6.3, which is the comparison between the power density spectrum of Gaussian 1 and a theoretical Gaussian spectrum the the PSD is slightly to the right of the theoretical values.

Similarly, we see that the histogram of Gaussian2, Figure 6.4, compared to a theoretical Gaussian spectrum also shows that the generated timeseries has slight deviations from theorectical values. It also seems as if the power density spectrum in Figure 6.5 is also shifted slightly to the right of theorectical values.

## Pierson-Moskowitz

In experiment 2 we used a Pierson-Moskowitz spectrum, Figure 6.6, the included frequencies for the Pierson-Moskowitz spectrum corresponds to a frequency range between $3.66 \leq \omega_n \leq 16.56$.

Histogram of paddle signal $T_p$ = 1.1, T = 20 min,
N = 3000 skew = -0.00018, kurt = 2.9
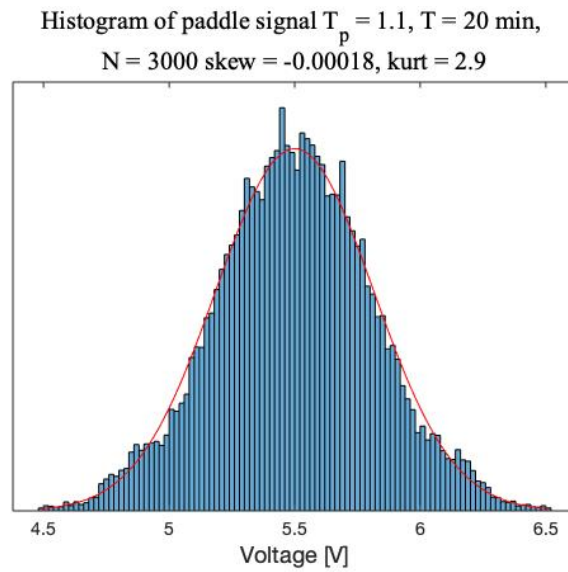


Figure 6.2: Histogram comparing Gaussian 1 time series and theoretical Gaussian spectrum.

Comparison between PSD of paddle signal and Gaussian 1,
$\omega_p$ = 5.712
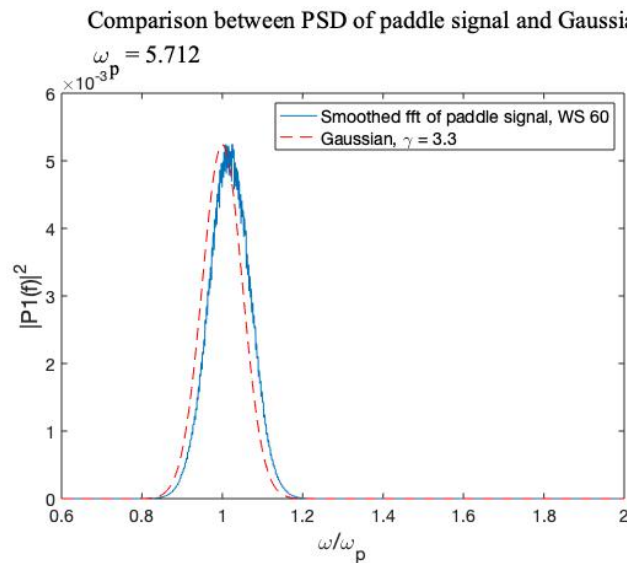


Figure 6.3: Comparison between power density spectrum of Gaussian 1 time series and theoretical Gaussian spectrum.

## 6.2 Parameters and setup

### The length of each run

The values of the statistical parameters converge at a rate of $\sqrt{\frac{C}{N}}$. See SECTION. In Figure 6.9 we show that when using the convergence rate of kurtosis 20 minute runs were are sufficient to ensure convergence. As this is

Histogram of paddle signal $T_p = 1$, T = 30 min,
N = 3000, skew = -4.5e-05, kurt = 2.7
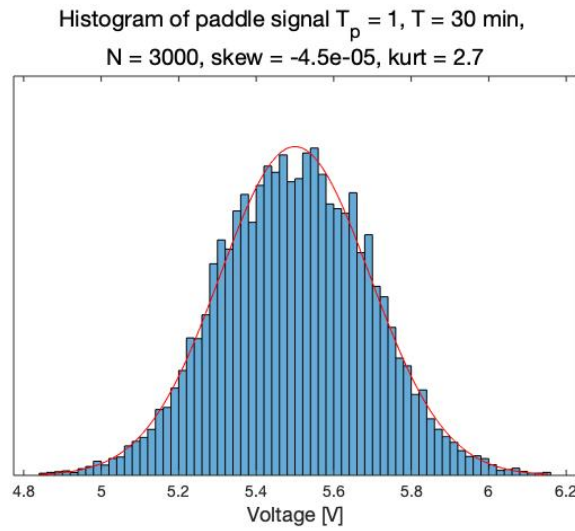


Figure 6.4: Histogram comparing Gaussian 2 time series and theoretical Gaussian spectrum.

Comparison between PDF of paddle signal and Gaussian2,
$\omega_{\text{3p}} = 5.712$
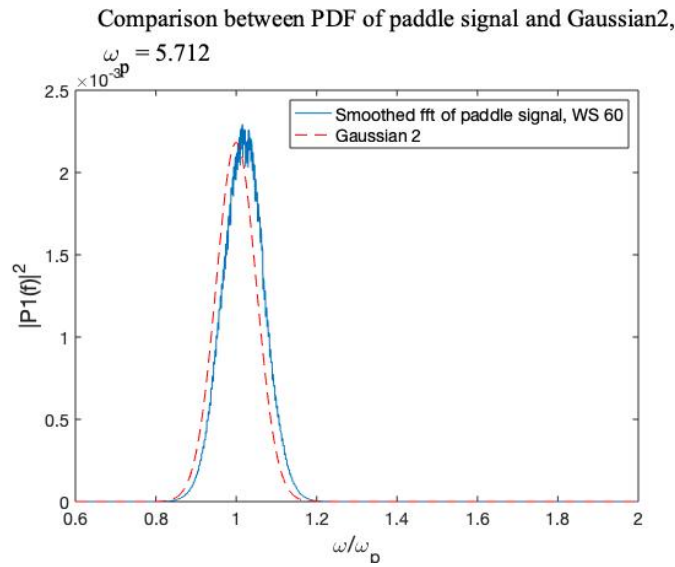


Figure 6.5: Comparison between power density spectrum of Gaussian 2 time series and theoretical Gaussian Spectrum.

the slowest convergence rate it follows that if kurtosis converges so should the other statistical parameters.Longer runs are not practically feasible due to two restraints, time in the lab and amounts of data to be processed.

If the probes start measuring the surface elevation as soon as the wave generator starts, the time series will all include start up effects from the wave maker. The probes will measure the still water before the wave train reaches the probes. Moreover, it is well known that the waves in the early wave train are more extreme than the rest of the wave field. Due to these initial effects we chose

29
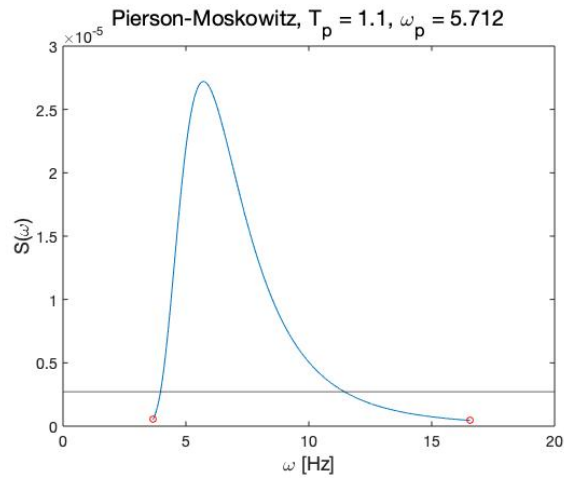
Figure 6.6: Pierson-Moskowitz Spectrum with a range of included frequencies between $3.66 \leq \omega_n \leq 16.56$
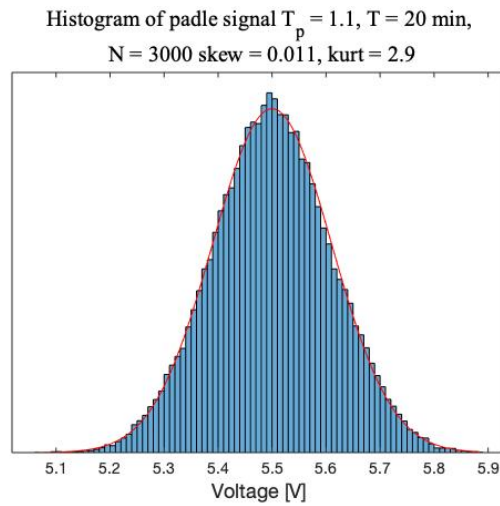


Figure 6.7: Histogram of the paddle signal compared to a with a theorectical Pierson-Moskowitz spectrum.

to run the wave maker for 30 seconds before the probes and the ADV start recording data.

The time series thus became $125 \text{ Hz} \cdot (20.5 \cdot 30) \text{ s} = 153750$ samples long for the ultrasound probes and $200 \text{ Hz} \cdot (20.5 \cdot 30) \text{ s} = 246000$ samples long for the ADV.

## Quiescent surface level and peak period

### Experiment 1

For experiment 1 and the quiescent surface level is set to 0.5 m with peak period of, $T_p = 1$ s. This due to simplicity as both experiments do not depend on a specific dimensionless depth.
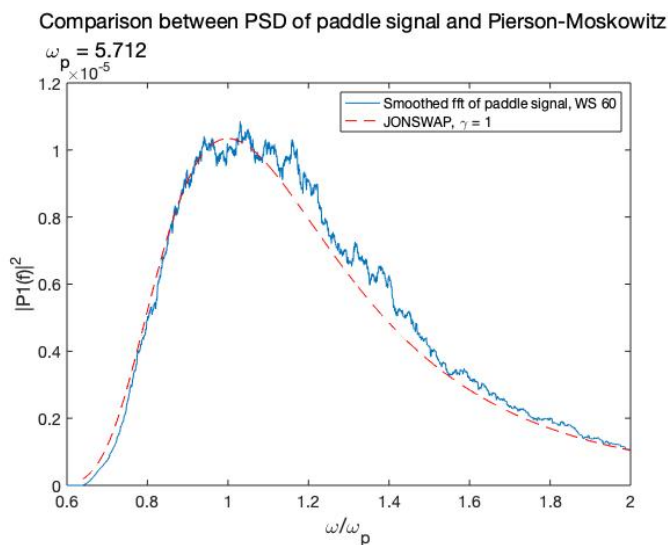
Figure 6.8: Comparison between the PSD of the paddle signal and a theorectrical Pierson Moskowitz spectrum.

### Experiment 2

Raustøl (2014) showed the dimensionless depth, $k_{p,2}h_2$, over the shoal was linked to the degree to which the field displayed Gaussian behaviour. Specifically, a field with a low dimensionless depth displayed more non-Gaussian behavior over the shoal compared to a field with a greater dimensionless depth.

Since we want to emulate the experiments of Raustøl and Jorde, we chose a dimensionless depth of $k_{p,2}h_2 \simeq 0.65$. This is the same dimesionless depth used in Jorde's master thesis. Moreover, we want a steepness $k_{p,2}a_2 \simeq 0.05$ similar to the one used by Raustøl and Jorde, without inducing wave breaking.

Considering that we are using a Pierson-Moskowitz spectrum there are two different factors that determine $k_{p,2}h_2$. The first is the peak period, $T_p$, and the second is water depth over the shoal, $h_2$.

| $T_p$ [s] | $h_2$ [m] | $k_{p,2}h_2$ |
|---|---|---|
| 1 | 0.10 | 0.681 |
| 1 | 0.11 | 0.719 |
| 1.1 | 10 | 0.611 |
| 1.1 | 0.11 | 0.645 |
| 1.1 | 0.12 | 0.677 |
| 1.2 | 0.10 | 0.555 |
| 1.2 | 0.11 | 0.5848 |
| 1.2 | 0.12 | 0.614 |

Table 6.1: Comparison of peak period, water depth over the shoal and dimensionless depth.

Table 6.1 shows that we are able to achieve a dimensionless depth of $k_{p,2}h_2 =$
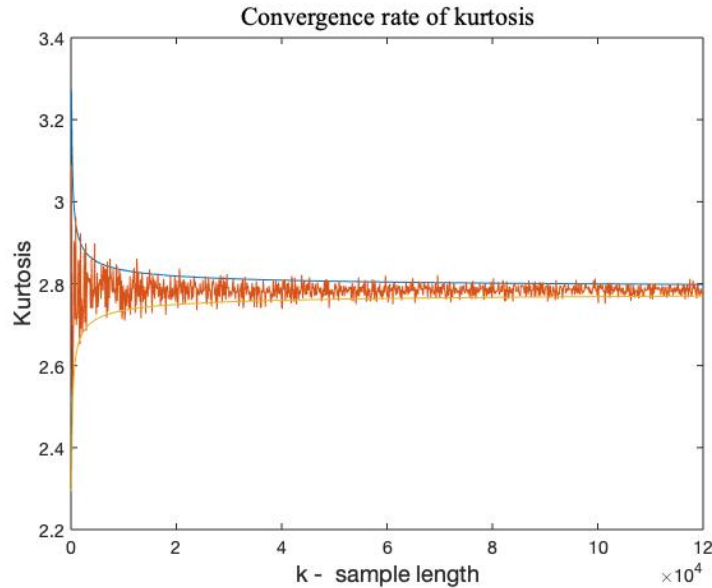
Figure 6.9: Graph displaying that the kurtosis converges as the sample length increases.

0.645 with a peak period, $T_p = 1.1$ s, and a water depth over the shoal of $h_2 = 0.11$ m . The shoal has a height of 0.41 m therefore the total water depth must be $h_1 = 0.52$ m.

### ADV placement

We assume that fluid flow is greatest directly below water surface, and therefore the ideal placement of the ADV is close to the surface without risking that the ADV receivers penetrate the surface in the wave troughs.

In order to measure the simultaneous behaviour of surface elevation and the velocity field it is important to place the ADV so that the measurement area is directly under the ultrasound probes. This placement is very sensitive and a slight misplacement will lead to the data needing to be adjusted in post processing.

For experiment 1, the ADV placement remained the same, 8 cm below the quiescent surface. In experiment 2, we had to account for the shoal, and therefore moved the ADV to 5.5 cm below the quiescent surface.

### Amplitude factors

We chose to run experiment 1 with two different Gaussian spectra that had different amplitude factors in order to test whether amplitude effected how a narrow banded spectrum develops as it propagates along the tank. The first spectrum, Gaussian1, had amplitude factor of 0.05. The second spectrum, Gaussian2, had an amplitude factor of 0.025.

In experiment 2 we want to maximise wave steepness whilst avoiding wave breaking. As the Pierson-Moskowitz spectrum used in experiment 2 has a $\gamma = 1$ the only factor we are at liberty to adjust is the amplitude factor.

We ran experiments, Table 6.2, with different Pierson-Moskowitz spectra, starting with an amplitude factor of alpha $= 0.05$ and decreasing it for every run. For each run we visually inspected the wave process for breaking waves. If breaking waves were observed the process continued. Once we no longer could observe breaking waves, the processed was stopped.

| Run | Amplitude Factor | Did waves Break? |
|-----|------------------|------------------|
| 1 | 0.05 | Yes |
| 2 | 0.025 | Yes |
| 3 | 0.01 | Yes |
| 4 | 0.008 | Yes |
| 5 | 0.006 | No |
| 6 | 0.006 | No |
| 7 | 0.007 | Yes |
| 8 | 0.0065 | Yes |

Table 6.2: Experiment to find maximal amplitude factor for Pierson-Moskowitz spectrum without waves breaking over the shoal.

Thus we achieved an amplitude factor of alpha $= 0.006$.

## 6.3 Parameters and Measurement equipment

We wish to measure the surface elevation several places simultaneously, however, we are limited as we only have four probes. Therefore, instead of using several probes per measuring location, we chose to measure four different locations per run.

After an assessment, we decided to use the ADVs standard settings for *Sampling rate*, *Transmit length*, and *Sampling volume* as they produced adequate results.

To increase accuracy, we set *Power level* to high. The maximum speed was measured to around 0.2 m/s.

Our ADV settings are:

- Sampling rate = 200 Hz.

- Nominal velocity range = 0.3 m/s.

- Transmit length = 1.8 mm.

- Sampling volume = 7.0 mm.

- Power level = High.

## 6.4 Synchronising the instruments

The ADV and ultrasounds probes are synchronised using a trigger signal which insures that once the wave maker is initiated the ADV and the ultrasound

probes start recording data after 30 seconds. We confirmed the accuracy of the trigger signal by running tests using a stopwatch.

We chose a delay of 30 seconds to ensure that the wave process is fully developed before any data is recorded.

# CHAPTER 7

## Experimental Methodology

### 7.1 In the lab

The experiments were performed in the 24.6 m long and 0.5 m wide tank at the Hydrodynamics Laboratory of the Department of Mathematics at the University of Oslo. The wave maker is placed at the one end of the tank and at the other end is a damping beach.

Every day in the lab started with the same routine of checking the water level in the tank and filling it if necessary. Then checking that the ADV is placed at the correct depth. During the time period where the wave maker is off and the water is stationary the seeding particles fall to the bottom of the tank and stick to its side. Therefore, every morning in the lab also starts by sweeping the particles of the tank floor and cleaning the sides of the tank.

#### Experiment 1: Narrow banded Spectra

The goal of this experiment is to study how a narrow banded wave process develops as it propagates along a tank. Therefore it is necessary to measure surface elevation and the velocity field at many different places. The full experimental setup is shown in Figure 7.1

The ultrasound probes 1,2, and 3 are staged with a fixed 1 m distance between on a sliding frame. Probe 1 is the ultrasound probe closest to the wave maker. The ADV is mounted on the end of the frame and is place $-0.08$ m below the quiescent surface. To check the effect of the ADV placement in the tank, probe 4 is mounted behind the ADV.

For every experimental position the frame is moved and the position is measured from probe 3 to the wave maker in its stationary middle position using a laser measure . This can be laborious process as any adjustment in position requires another measurement using the laser measure. The further the frame is moved away from the wave maker the more difficult it becomes to use the laser measure as the beam can more easily be refracted by the glass walls of the tank or the water creating errors.

Many of the experimental runs are repeated three times to ensure that the results are reliable.

For this experiment the y-axis is aligned vertically from the quiescent surface whilst the x-axis runs horizontally with origo placed at the location of the wave

| Position | $P_1$ [m] | $P_2$ [m] | $P_3$ [m] | $P_4$ [m] | ADV [m] |
|:---:|:---:|:---:|:---:|:---:|:---:|
| 1 | 2.006 | 3.006 | 4.006 | 4.711 | 4.006 |
| 2 | 3.003 | 4.003 | 5.003 | 5.71 | 4.003 |
| 3 | 4.005 | 5.005 | 6.005 | 6.763 | 6.005 |
| 4 | 5.003 | 6.003 | 7.003 | 7.757 | 7.003 |
| 5 | 6.062 | 7.062 | 8.062 | 8.819 | 8.062 |
| 6 | 7.008 | 8.008 | 9.008 | 9.765 | 9.008 |
| 7 | 8.009 | 9.009 | 10.01 | 10.758 | 10.01 |
| 8 | 10.022 | 11.022 | 12.02 | 12.776 | 12.02 |
| 9 | 12.015 | 13.015 | 14.015 | 14.771 | 14.015 |
| 10 | 14.009 | 15.009 | 16.009 | 16.758 | 16.009 |
| 11 | 16.018 | 17.018 | 18.018 | 18.773 | 18.018 |

Table 7.1: Location of the ultrasound probes and the ADV for the different experiment 1 positions.
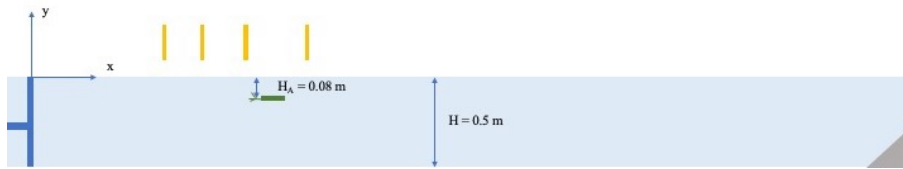


Figure 7.1: Diagram of the experimental setup of experiment 1.

makers middle position.

## Experiment 2: Analysis of the effects of non uniform bathymetry

The experiments utilise three different shoals. All three shoals had a maximum height of 0.41 m. The first shoal has a 1.6 m linear up-slope, a 1.6 m horizontal section and a 0.8 m linear down-slope. The second shoal has a 0.8 m linear up-slope, a 1.6 m horizontal section, and a 1.6 m linear down-slope. The third shoal is a step with a 1.6 m horizontal section creating a discontinuous bathymetry. The experimental setup for shoal one, two and three is shown in Figures 7.2, 7.3 and 7.4 respectively.

The water depth in the deep end of the tank is $h_1 = 0.52$ m, therefore the water depth over the shoal is 0.11 m. The coordinate system is orientated so that the x-axis runs horizontally in the direction of the waves propagation with origin at the start of the horizontal part of the shoal. The y-axis is aligned vertically from the quiescent water level.
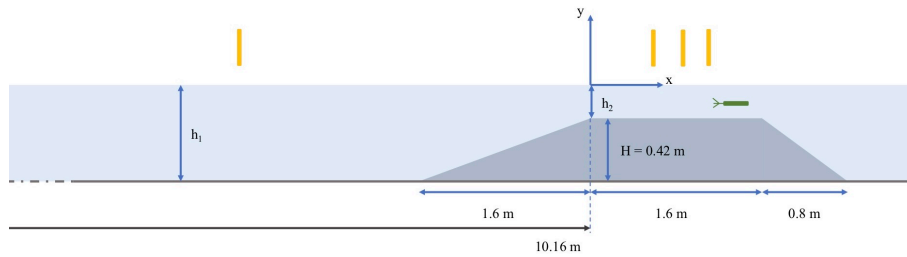
Figure 7.2: Setup of experiment 2 with the first shoal.
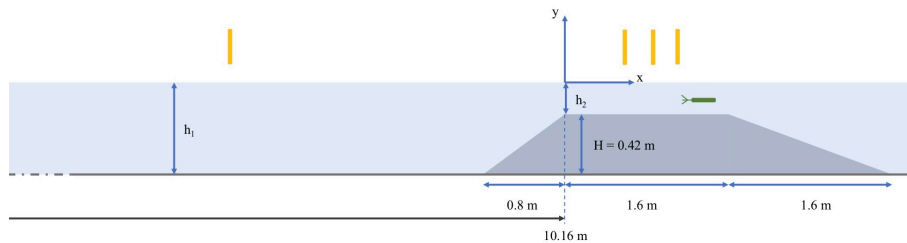


Figure 7.3: Setup of experiment 2 with the second shoal.
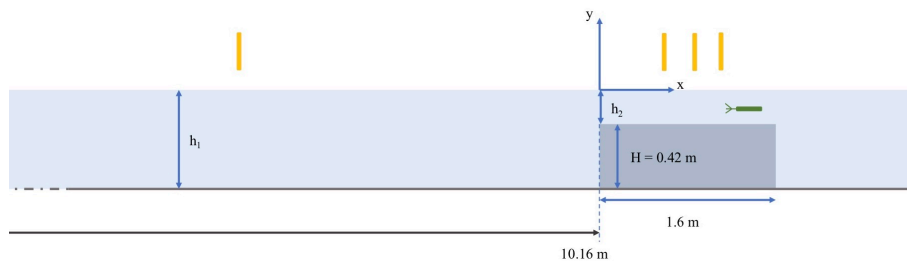


Figure 7.4: Setup of experiment 2 with the third shoal.

We want to measure surface elevation and water velocity at several locations along the tank. Due to the fact that we only have four ultrasound probes and one ADV we need to repeat the experiment at different locations along the tank. It is also useful to repeat several times at the same location to check how reproducible the results are.

The ultrasound probes are mounted vertically, and the ADV horizontally, on a frame that is mobile. The three of the ultrasound probes are staged one after another. The probe furthest from the wave maker measures just above the measuring range of the ADV. The first ultrasound probe is mounted at the deep end of the tank to corroborate that the Pierson-Moskowitz field in is the same for all runs.

It is important that the shallow regime above the shoal is sufficiently shallow, therefore the ADV is mounted horizontally. In order for it to disturb the current as little as possible, the ADV is mounted so that it points towards the wave maker.

The experiments with the first and second shoal were performed three times

| Position | $P_1$ [m] | $P_2$ [m] | $P_3$ [m] | $P_4$ [m] | ADV [m] |
|:---:|:---:|:---:|:---:|:---:|:---:|
| 1 | -2.900 | -2.255 | -1.5 | -0.8 | -0.8 |
| 2 | -2.900 | -1.855 | -1.1 | -0.4 | -0.4 |
| 3 | -2.900 | -1.455 | -0.7 | 0 | 0 |
| 4 | -2.900 | -1.155 | -0.4 | 0.3 | 0.3 |
| 5 | -2.900 | -0.855 | -0.1 | 0.6 | 0.6 |
| 6 | -2.900 | -0.555 | -0.2 | 0.9 | 0.9 |
| 7 | -2.900 | -0.255 | 0.5 | 1.2 | 1.2 |
| 8 | -2.900 | 0.045 | 0.8 | 1.5 | 1.5 |
| 9 | -2.900 | 0.455 | 1.2 | 1.9 | 1.9 |
| 10 | -2.900 | 0.845 | 1.6 | 2.3 | 2.3 |
| 11 | -2.900 | 1.245 | 2 | 2.7 | 2.7 |

Table 7.2: Location of the ultrasound probes and the ADV for the different experiment 2 positions.

at positions 1-11, Table 7.2, totalling 64 runs. The experiments with the third shoal were performed three times at positions 2-10, totalling 27 runs. In total experiment 2 produced of 94 runs.

## 7.2 Postprocessing

### Surface elevation from the Ultrasound Probes

The ultrasound probes measure the distance to the water surface. To find the surface elevation, $\eta$, at the quiescent surface, $x = 0$ m, we use the formula

$$\eta = -(a - \bar{a}), \tag{7.1}$$

where $a$ is the distance measured by the probes, $\bar{a}$ is the average measurements, and the negative sign is there because the ultrasound probes are pointing downwards.

### Dropout Filtering

The raw data from the ultrasound probes contains erroneous noise called dropouts. It is caused by the ultrasonic signal not being returned to the probe when the waves under the probes are too steep. The steepness of the waves causes the signal to be sent in a different direction. One can clearly visually observe these 'dropouts' in the time series.

To increase the accuracy of the statistical analysis of the different times series, the noise must be removed. Several different filters have been designed at the hydrodynamic laboratory by Odin Gramstad, Tore Magnus A. Taklo, and Anne Raustøl among others. In this thesis we used (`InterpolateDropouts`) and (`InterpolateSpikes`)

The first filter, called `InterpolateDropouts`, removes sample points and interpolates new samples points based on the samples in front of and behind the removed sample. It has two criteria for removing points. Firstly, the points that have a value above or bellow a specific threshold are removed by setting the

value to NaN (Not a Number). If the threshold is set to $\pm 5$ cm then all values greater than 5 cm and all values less than $-5$ cm are set to NaN. The second criterion specifies that if two neighbouring points have a Euclidean distance greater than a given threshold, they are also removed and interpolated.

`InterpolateDropouts` is highly efficient at removing dropouts when they are far greater than the typical wave oscillations, however its struggles removing noise when it is within the range of typical wave values. Therefore, we used a second filter called `InterpolateSpikes`. This filter removes sample points that have a slope above a given threshold value. The criterion is given by

$$\left| \frac{(\eta_{i+1} - \eta_i)}{(t_{i+1} - t_i)} \right| > \text{ Threshold.} \qquad (7.2)$$

The results of the interpolation process can be seen below
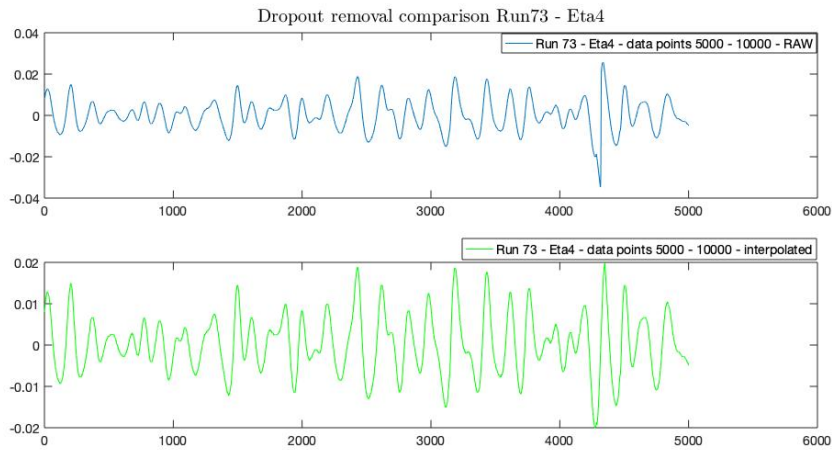


Figure 7.5: Comparison of before and after dropout removal.

### DFT resampling and interpolation

The surface elevation and velocity field are sampled at different rates, 125 Hz and 200 Hz respectively. To study simultaneous relationship between surface elevation and velocity field we want to have the same number of sampling points. This can be achieved by using DFT resampling or 'zero-padding'. It is the process of taking a function with elements $\{f_j : j = 1, 2, \cdots, N\}$ and converting it into its frequency domain $\{\hat{f}_n : n = 1, 2, \cdots, N\}$ using DFT. The signal can then be extended to a a size M by padding the center of the signal, $N/2$ with $M - N$ zeros. Once the function is converted back into the time domain it is resampled.

### Finding $v_{x,best}$ from $v_{x,1}$ and $v_{x,2}$

The ADV produces two independent measurements for $v_x$ for each time point. The two independent measurements can be used to weed out idiosyncratic errors and reduce measurement uncertainty.

The ADV provides three quality indicators of each measurement namely, SNR, correlation, and amplitude. We can also define $\Delta v_x$ as the eucleadian distance between two measurements at the same time, t.

We test the four different performance indicators to discern how well they describe measurement quality. The three performance indicators provided by the ADV do not effectively reveal measurement points which are corrupted by idiosyncratic measurement errors. The problem stems from not being able to find a benchmark which removed obvious errors while not loosing significant information.

However, it seems that $\Delta v_x$ is able to remove idiosyncratic measurement errors. The points removed by $v_x$ as a quality indicator are randomly scattered along the curve, i.e. removing them will not create a systematic error.

The following algorithm is implemented to find $v_{x,best}$:

---
**Algorithm 1** Find $v_{x,best}$

---
    **for** $i = 1 : N$ **do**
        **if** $\Delta v_x(i)$ greater than benchmark **then**
            $v_{x,best} = NAN$
        **else**
            $v_{x,best}(i)$ is mean between $v_{x,1}(i)$ & $v_{x,2}(i)$
        **end if**
    **end for**

---

### Corroborating the wave field

We assume that the field is the same for all runs, so that the measurements are conducted under equal conditions.

To verify this assumption probe 1 is placed at the same position for every run. We calculated the standard deviation of every run for shoal 1 at every time step and the average standard deviation was 4.8 mm.

Moreover, we want the wave field have a Pierson-Moskowitz spectrum. Therefore we can calculate the power spectrum of the surface elevation in the deep regime and compare it to a theoretical Pierson-Moskowitz spectrum.

## 7.3 Mesurement Errors

There are several factors that may effect the results, including the experimental setup, inherent factors in the experimental equipment, and outside idiosyncratic errors.

The ADV is mounted on a metal rod which is connected to the moving frame. On the end of the metal rod there is a small shelf holding the ADV. The shelf is connected to the metal rod by a one screw. This means that with larger waves it is possible for the shelf to move the ADV slightly to the left or slightly to the right. However, when the ADV is on it displays its results in real time graphs. It is therefore possible to control for this visually. Moreover, the amplitude
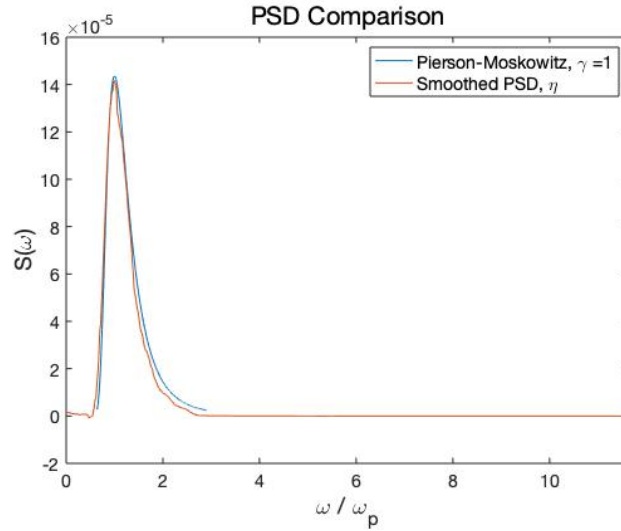
Figure 7.6: Comparison of a theoretical Pierson-Moskowitz Spectrum with the experimentally observed wave spectrum.

factors of the wavemaker spectrums are so small that we were not able to detect any such motion.

When running experiments we took great care to ensure that no waves broke, however it is certainly possible, albeit rarely, that micro-breaking did occur.

It is obvious from Section 7.2 that dropouts in the surface elevation data are a problem. Furthermore, dropouts occur when the surface becomes too steep as the ultrasound waves emitted by the probes are refracted in an direction that cannot be received by the receivers of the probes. This error is systematic and although great care is taken to repair the data, through filtering and interpolation, the reparation will never be perfect.

Although great effort is taken to ensure a high level of measurement accuracy, there is an uncertainty on the distance from the ADV and ultrasound probes to the wave maker paddle. The distance from the wave maker paddle in middle position to the probes and the ADV was measured every single day with a laser measure and the level of dedication to accuracy boarded on mania. Not to mention the ADV depth was kept constant at either 8 cm or 5.5 cm below the quiescent surface. It is not possible to use a laser measure to control this distance as the ADV is under water. Therefore, we used a metal ruler to control the ADV placement. There may be some inaccuracy on a millimeter level.

Using the ADV included filling the tank with copious amounts of seeding particles. Over time these seeding particles could stick to the tank walls at the quiescent surface level and could potential cause surface effects. Cleaning the tank walls became a vital part of my morning routine.

41

# PART III

## Analysis

# CHAPTER 8

# Experiment 1: Narrow banded spectra

This chapter displays the experimental results and the results of the analysis of experiment 1 which studies how a narrow banded spectra develops as it propagates along the tank. Section 8.1 calculates the steepness and dimensionless depth of the surface elevation of the Gaussian 1 and Gaussian 2 wave process. Futhermore, this section calculates the spectral bandwidth and Benjamin-Feir index of the surface elevation and velocity field of both Gaussian 1 and Gaussian 2 wave processes. Section 8.2 presents variance, autoskewness, and autokurtosis. Section 8.3 studies how the power spectral densities of the different wave processes change as they propagate along the tank. Note when we write 'velocity field' we are referring to the velocity field in x-direction.

## 8.1 Mechanical Parameters

Figure 8.1 displays the steepness of the surface elevation of the Gaussian 1 and Gaussian 2 wave processes. In both Figure 8.1(a) and (b) we see that the steepness is decreasing as the wave process propagates along the tank.

We see from Figure 8.2 that the dimensionless depth is reasonably flat. In Figure 8.2(a) we see that there is a downshift around $x = 12$ m. This might due $k_p$ being calculated from the estimated peak frequency $\omega_p$. Yet, some of the points may be due to large errors such as the very obvious point at $x = 13$ m in Figure 8.2(b).

In Figure 8.3(a) we see the bandwidth of the surface elevation of Gaussian 1 is stable, with prominent errors, until $x = 10$ m. After $x = 10$ m the bandwidth varies wildly. This is may be due to an the half peak, half width estimation method not being suitable if the shape of the wave spectrum deforms asymmetrically. We that the bandwidth of the surface elevation of Gaussian 2 is much more stable, yet with unmistakable outliers. Similar the bandwidth of the velocity field, of both Gaussian 1 and Gaussian 2 in Figure 8.3(c) and (d), is much mores stable.

Due to the fact that we are uncertain about our estimation methodology of bandwidth, we are uncertain about the estimation of the Benjamin-Feir Index in Figure 8.4. We see that due to the bandwidth being reasonably constant in Figure 8.3(b), the decreasing trend from the steepness in Figure 8.1(b)

dominates. This results in the BFI of the surface elevation of the Gaussian 2 wave process is clearly decreasing as the process propagates.



(a) Gaussian 1
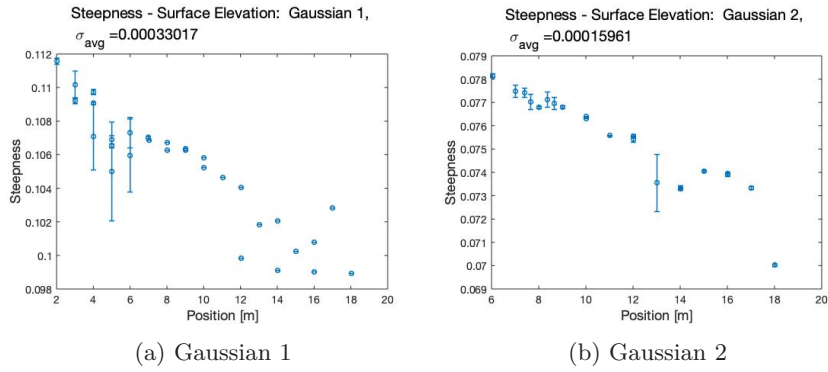
(b) Gaussian 2

Figure 8.1: Figure (a) depicts the steepness, $\epsilon$, of Gaussian 1. Figure (b) displays the steepness, $\epsilon$, of Gaussian 2.



(a) Gaussian 1
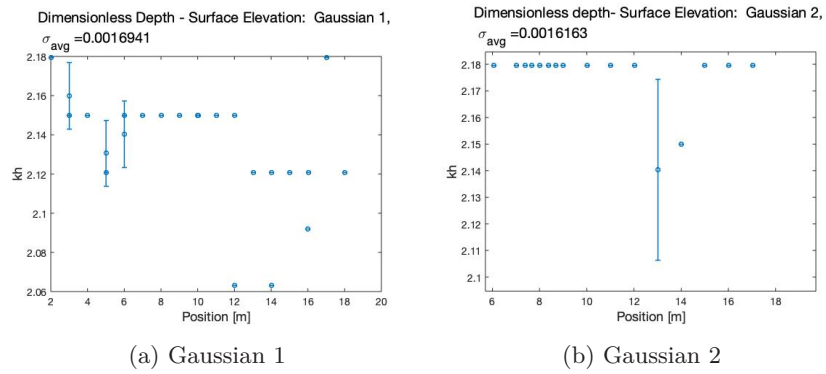
(b) Gaussian 2

Figure 8.2: Figure (a) depicts the dimensionless depth, $kh$, of Gaussian 1. Figure (b) displays the the dimensionless depth, $kh$, of Gaussian 2
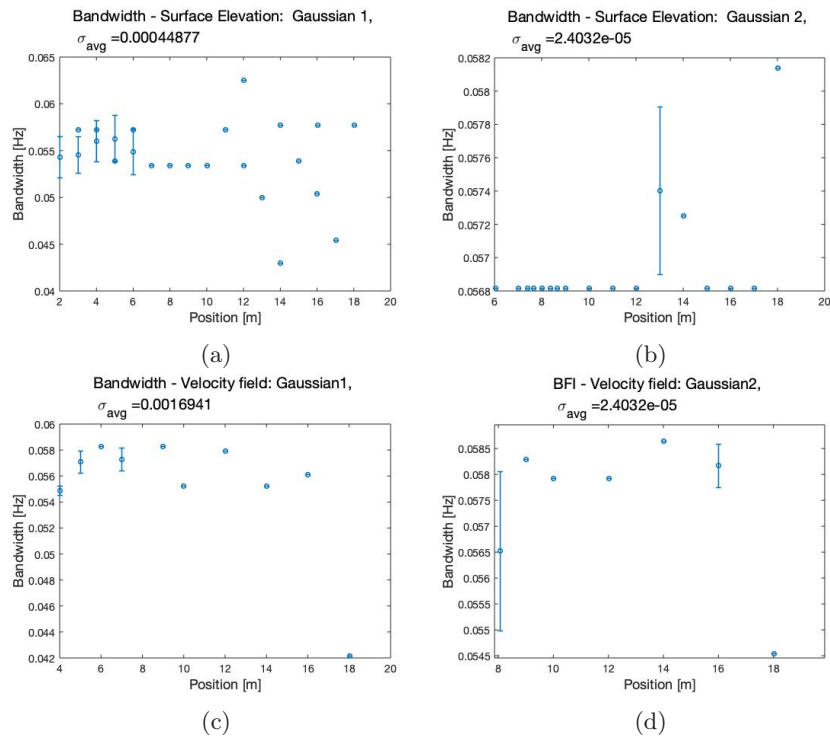
Figure 8.3: Figure (a) displays the bandwidth of the wave spectrum of the surface elevation as Gaussian 1 the wave process propagates along the tank. Figure (b) displays the bandwidth of the wave spectrum of the surface elevation Gaussian 2 the wave process propagates along the tank. Figure (c) displays the bandwidth of the wave spectrum of the velocity field as Gaussian 1 the wave process propagates along the tank. Figure (b) displays the bandwidth of the wave spectrum of the velocity field Gaussian 2 the wave process propagates along the tank.
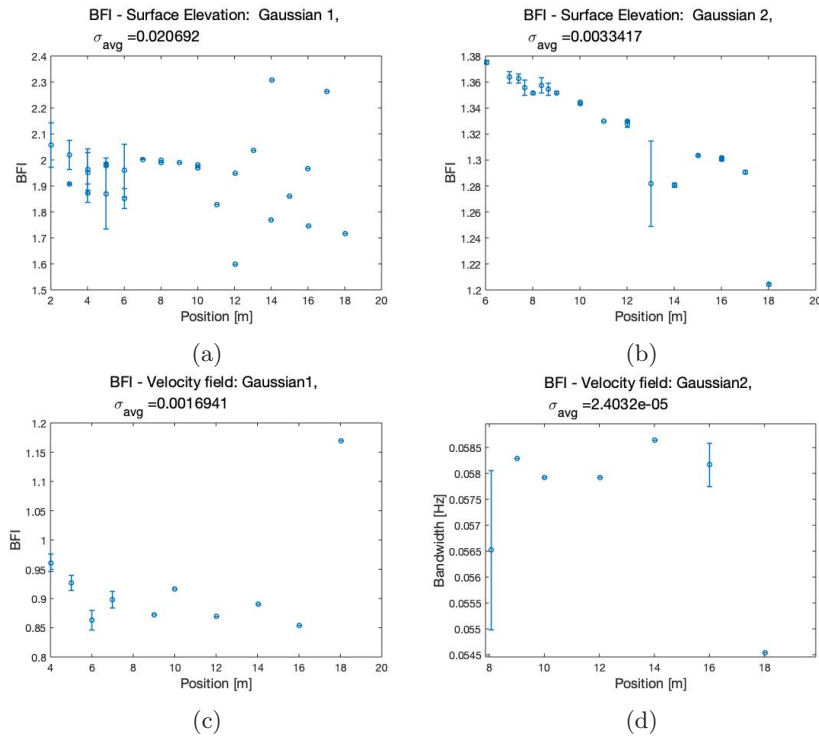
Figure 8.4: Figure (a) displays the BFI of the surface elevation of Gaussian 1. Figure (b) displays the BFI of the surface elevation of Gaussian 2. Figure (c) displays the BFI of the velocity field of Gaussian 1. Figure (d) displays the BFI of velocity field of Gaussian 1.

## 8.2  Statistics

The variance is calculated using MATLABs `var(x, 'omitnan')` function with the nanflag that omits Nan values. The autoskewness and autokurtosis are calculated through functions that we created, since the built-in MATLAB functions did not have an 'omitnan' option.

Figure 8.5 shows a clear declining tendency in the variance of the surface elevation of both the Gaussian 1 wave process and the Gaussian 2 wave process as the processes propagate along the tank. The rate at which the variance decreases is greater for Gaussian 1, compared to Gaussian 2. Additionally, in Figure 8.6 we observe that the velocity field variance exhibits the same declining tendency. Comparing the velocity field and surface elevation, in Figure 8.7, we see the that the variance of the velocity field is significantly greater than the variance of the surface elevation.

In Figure 8.8, we see that the surface autoskewness is increasing for both wave processes. Moreover, both processes are already slightly positively skewed at the first measurement at 2 m and 6 m. This means that the right side distribution, describing positive values of the surface elevation function, will have longer or fatter tails. As a result, the surface elevation function will include a larger range of positive values compared to negative values, meaning that more extreme
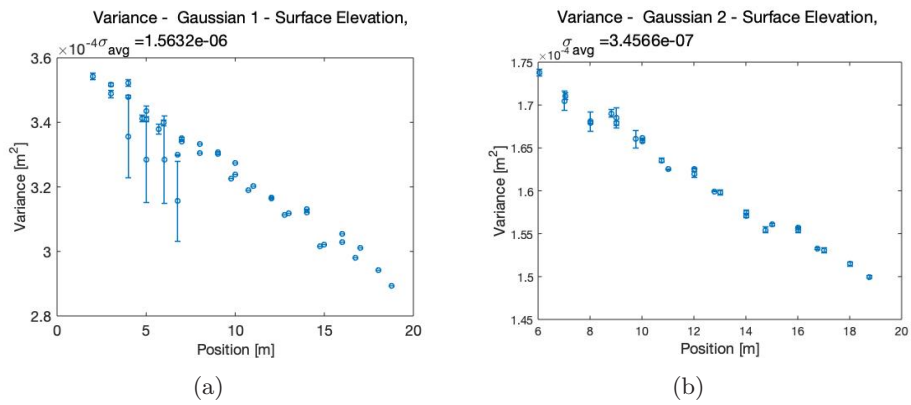
Figure 8.5: Figure (a) displays the variance of the surface elevation of the Gaussian 1 wave process. Figure (b) displays the variance of the surface elevation of the Gaussian 2 wave process.
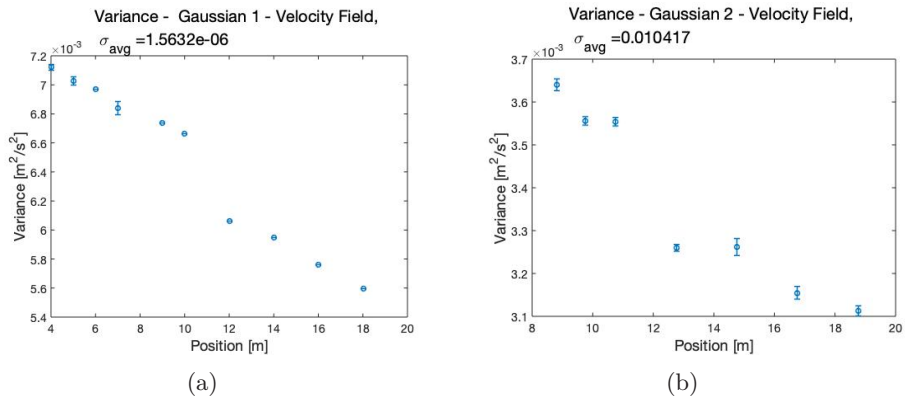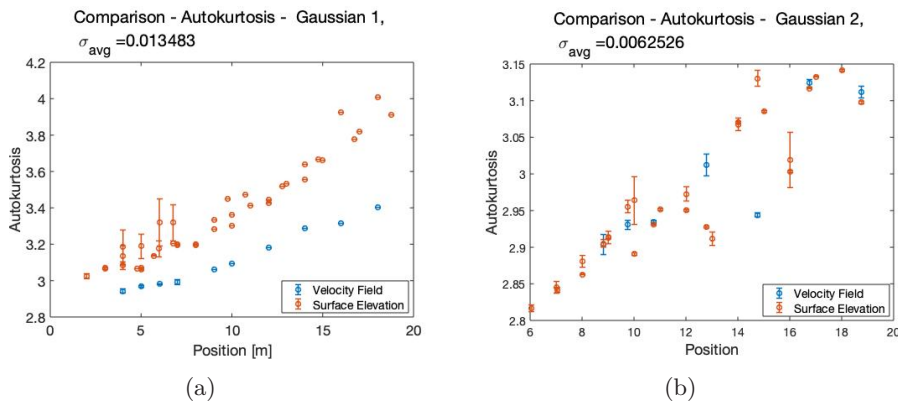


Figure 8.6: Figure (a) displays the variance of the velocity field of the Gaussian 1 wave process. Figure (b) displays the variance of the velocity field of the Gaussian 2 wave process.
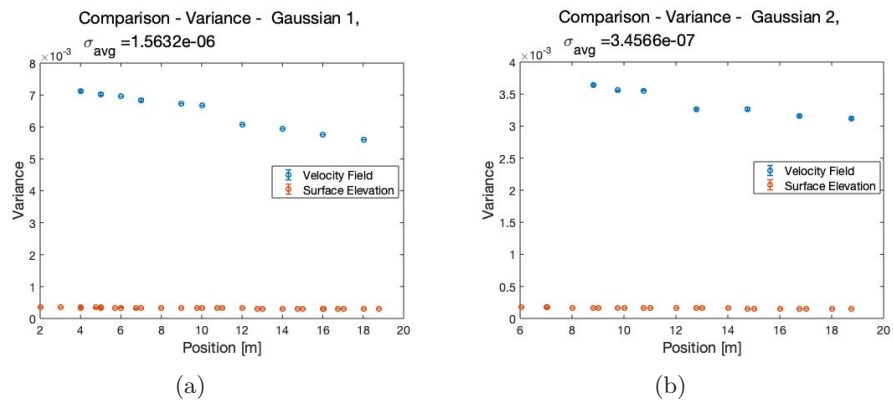


Figure 8.7: Figure (a) displays a comparison of the variance of the Gaussian 1 wave process. Figure (b) displays a comparison of the variance of the Gaussian 1 wave process.

47
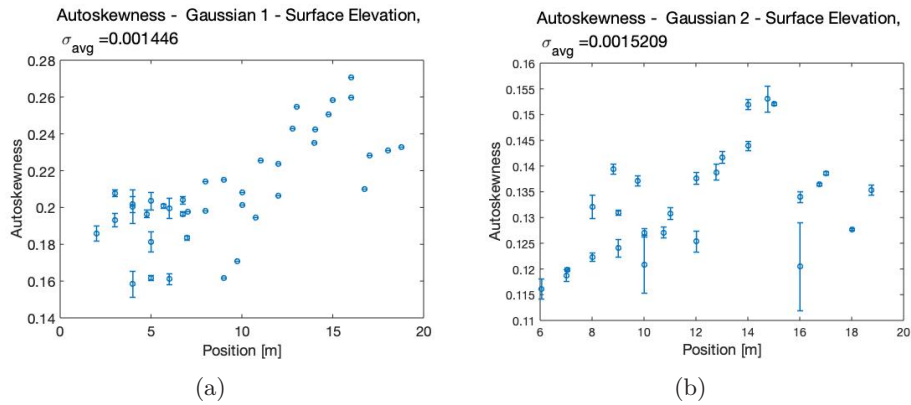
Figure 8.8: Figure (a) displays the autoskewness of the surface elevation of the Gaussian 1 wave process. Figure (b) displays the autoskewness of the surface elevation of the Gaussian 2 wave process.
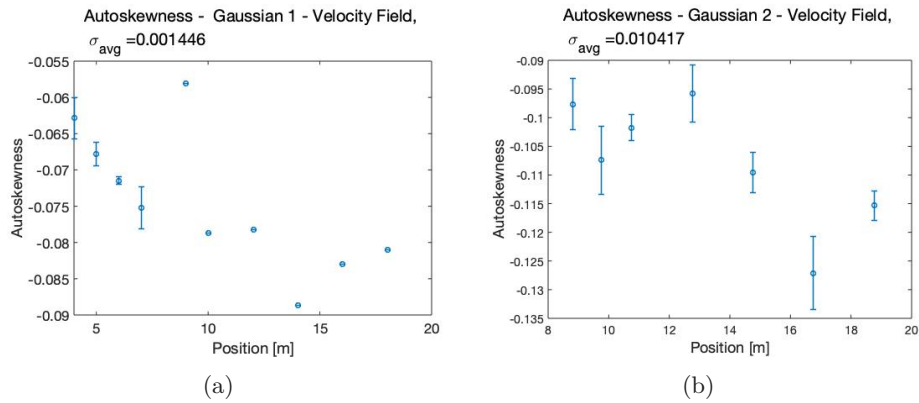


Figure 8.9: Figure (a) displays the autoskewness of the velocity field of the Gaussian 1 wave process. Figure (b) displays the autoskewness of the velocity field of the Gaussian 2 wave process.

positive values occur more often than extreme negative values. Curiously, it seems as if in the autoskewness of the velocity field in Figure 8.9 there may possibly be a slight decrease in autoskewness. However, it is very unclear due to there being very few samples. Either way, the reduction in autoskewness is very slight. For Gaussian 1 autoskewness varies between $-0.0887$ and $-0.063$ and for Gaussian 2 autoskewness varies between $-0.1235$ and $-0.0957$. Yet, it is noticeable that the autoskewness is ever so slightly negatively skewed resulting in the left tail being ever so slightly longer or fatter. A common rule of thumb is that distributions are fairly symmetrical if autoskewness is less that 0.5 and greater than $-0.5$. The autoskewness of the surface elevation and velocity field for both Gaussian 1 and Gaussian 2 are well within those limits. All though it is curious that in Figure 8.10 we observe that the autoskewness of the velocity field and autoskewness of the surface elevation develops differently from each other.

In Figure 8.11, autokurtosis of the surface elevation of both the Gaussian 1 and

48
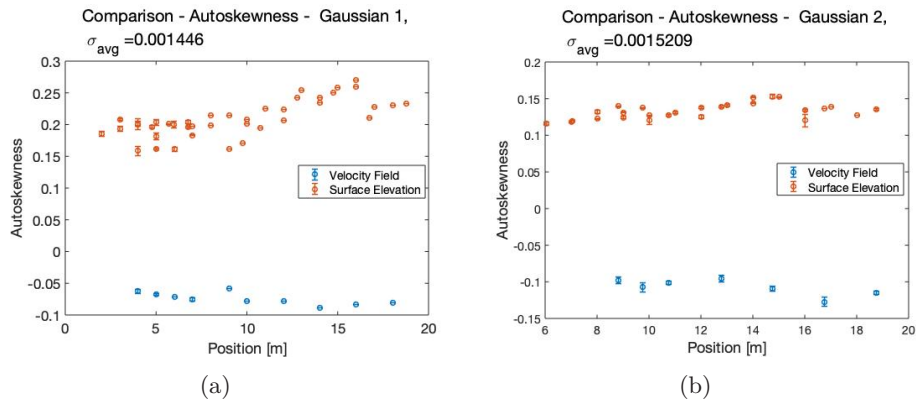
Figure 8.10: Figure (a) compares the autoskewness of the velocity field and surface elevation of the Gaussian 1 wave process. Figure (b) compares the autoskewness of the velocity field and surface elevation of the Gaussian 2 wave process.

Gaussian 2 wave process are clearly increasing. The difference between them, however, is that the wave process with a higher amplitude factor, Gaussian 1, increases at a much higher rate. At 2 m from the wave maker Gaussian 1 has an autokurtosis of 3.0250 and at 18 m from the wave maker Gaussian 1 has a kurtosis of 4.0066. As the Gaussian 1 wave process has propagated along the tank the surface elevation has become much more extreme.

Similarly, in Figure 8.12 the autokurtosis of the velocity field in also increasing. Figure 8.13 is highly interesting as it compares the autokurtosis of the surface elevation and velocity field of both the Gaussian 1 wave process, (*a*) and the Gaussian 2 wave process, (*b*). Clearly, in all cases the autokurtosis increases as the wave process propagates along the tank. However, it is clear that the autokurtosis of the surface elevation of Gaussian 1 increases much more sharply than the velocity field of Gaussian 1. Furthermore, the autokurtosis of the surface elevation of Gaussian 1 increases at a much higher rate than autokurtosis of the surface elevation of Gaussian 2. This indicates that the higher amplitude factor in Gaussian 1, compared to Gaussian 2, increases the rate at which the process becomes more extreme.
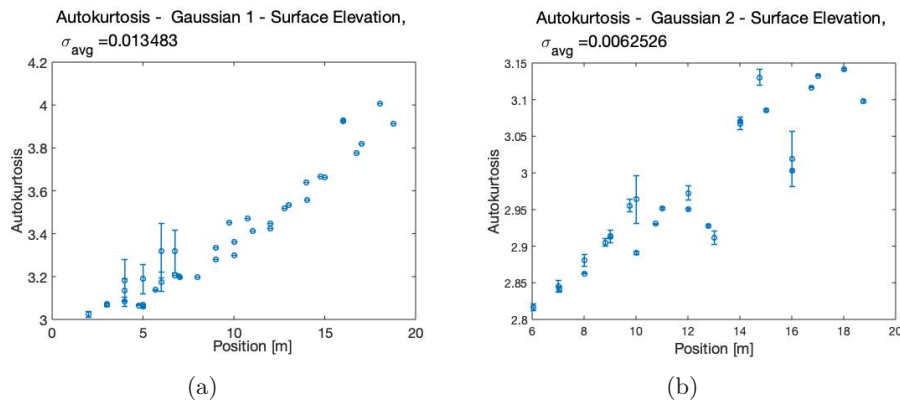
Figure 8.11: Figure (a) displays the autokurtosis of the surface elevation of the Gaussian 1 wave process. Figure (b) displays the autokurtosis of the surface elevation of the Gaussian 2 wave process.
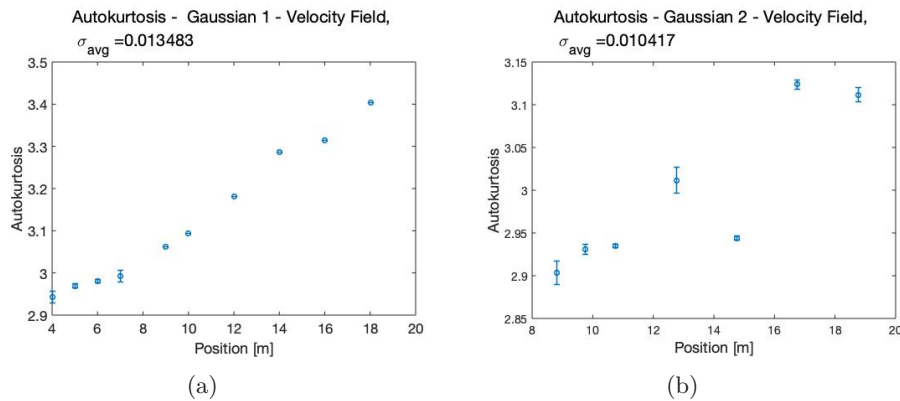


Figure 8.12: Figure (a) displays the autokurtosis of the velocity field of the Gaussian 1 wave process. Figure (b) displays the autokurtosis of the velocity field of the Gaussian 2 wave process.

## 8.3  Spectral Analysis

A major issue when estimating the power spectral densities is that the spectral density estimator has a standard deviation equal to its expected value. This can lead to the estimate looking very rough and not being particularly useful. Therefore, we must employ several tactics to smooth the PSD estimate. The first is to calculate the PSD estimate using the MATLAB function `pwelch(x)` which has built-in smoothing functionalities. However, to get a smooth estimate using `pwelch(x)`, we specified that the signal must be divided into thelongest possible segments obtainable, yet not to exceed 8 segments with 50% overlap and used a hamming window.

Then, the spectral density estimate is sent through MATLABs `smoothdata(x)` where we specified the use of a Savitzky-Golay filter which is particularly adept at increasing the precision of the data without distorting the signal tendency.

50

Figure 8.13: Figure (a) displays the autokurtosis of the velocity field of the Gaussian 1 wave process. Figure (b) displays the autokurtosis of the velocity field of the Gaussian 2 wave process.

Figure 8.14(a) compares the estimated PSD at 2 m and at 18 m for the surface elevation Gaussian 1. We see two effects very clearly. The first is a frequency downshift and the second is a clear change of shape as the right spectral side band has become elongated. Comparatively, in Figure 8.14(b) the PSD of the surface elevation of Gaussian 2 does have a frequency downshift and a small change in shape. Yet they are not of the magnitude as in Figure 8.14(a).

We can better understand how the spectrum of Gaussian 1 develops as it propagates a long the tank by plotting all the PSD estimates at every position in the same graph, Figure 8.15(a). We see clearly the further the process propagates the larger the frequency downshift and shape alteration.

The same comparison in Figure 8.15(a) shows a similar trend a small frequency downshift and some change in shape as the process propagates along the tank. This implicates that the increase amplitude factor of Gaussian 1 increasing the size of or rate at which the process develops.
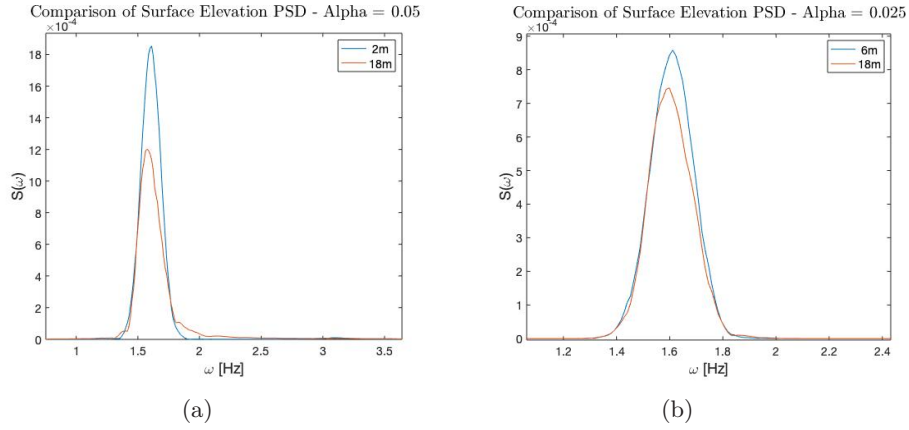
Figure 8.14: Figure (a) compares the PSD at 2 m, (blue), and the PSD at 18 m, (orange), of the surface elevation of Gaussian 1. Figure (b)compares the PSD at 6 m, (blue), and the PSD at 18 m, (orange), surface elevation of Gaussian 2.
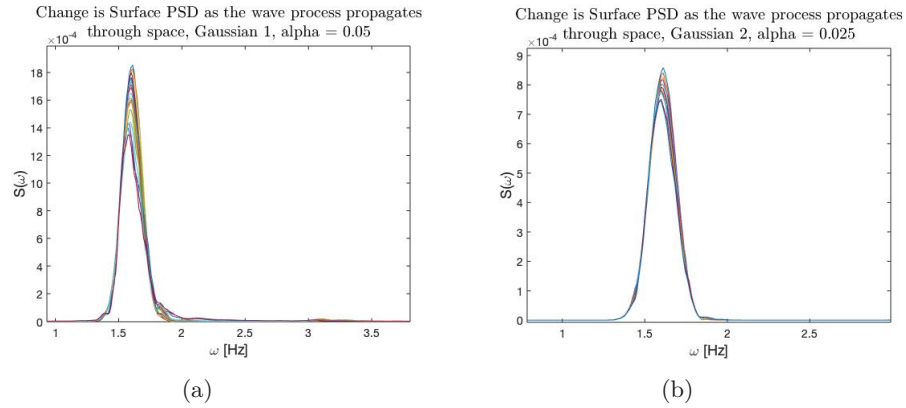


Figure 8.15: Figure (a) compares the PSDs of the surface elevation of Gaussian 1 at different positions along the tank. Figure (b) compares the PSDs of the surface elevation of Gaussian 2 at different positions along the tank. In both cases the measurement points are evenly spread out from 2 m to 18 m.

# CHAPTER 9

## Experiment 2: Effects of non-uniform Bathymetry

This chapter presents the results of experiment 2 which studies the effects on non-uniform bathymetry on a wave field with a Pierson-Moskowitz wave spectrum. Section 9.1 presents common mechanical parameters. Section 9.2 studies how the statistical automoments are effected by the different shoals. It is worth noting that previous studies with a similar setup have studied the effects of a JONSWAP spectrum over a symmetric shoal. This thesis studies the effects of a Pierson-Moskowitz spectrum and an asymmetrical shoal. Section 9.3 examines the statistical comoments of surface elevation and velocity field. Section 9.4 discusses the probability distribution of the velocity field and surface elevation. Section 9.5 analyses the dependence structure between the velocity field and surface elevation through the use of Copulae. Note when we write 'velocity field' we are referring to the velocity field in x-direction.

In all figures that have position on the x-axis the red line indicates the start of the upwards slope, the yellow line indicates the start of the plateau, the purple line indicates the start of the downwards slope, and the green line indicates the end of the downwards slope.

## 9.1   Mechanical Parameters

Figure 9.1 depicts the surface steepness as the wave field propagates over shoal 1 (a), shoal 2 (b), and shoal 3 (c). It is clear that the shoal geometry influences the steepness. As the upward slope becomes shorter and steeper it leads to the waves' steepness increasing at a faster rate. As the wave process propagates over the shoal plateau, the wave steepness stabilises before it decreases as it propagates over the downward slope. It is not evident that the downward slope has the same profound effect as the upward slope.

It is unsurprising that the dimensionless depth in Figure 9.2 decreases as the wave process propagates over the shoal.

Similarly, Figure 9.3, the Ursell number is also affected by the shoals geometry. It increases as the wave process propagates into the shallow regime.

It is interesting to note from Figure 9.4 that the bandwidth remains unchanged from propagating above the shoal.

If we now study the BFI in Figure 9.5, we see that the BFI increases slightly over all three shoals. The BFI of the surface elevation is depicted in Figure 9.5(a), (c) and (e). In Figure 9.5(a), the BFI is $0.0706 \pm 0.001$ at $x = -2.555$ m and increases to $0.1585 \pm 0.001$ at $x = 0$ m. In Figure 9.5(b) the BFI is $0.0793 \pm 0.001$ at $x = -2.555$ m and increases to $0.1439 \pm 0.001$ at $x = 0$ m. If we disregard the three points in front of the shoal 3, Figure 9.5(c), with very high standard deviations we have a peak in BFI of $0.56 \pm 0.03$ at $x = 0.6$ m. The BFI of the velocity field is depicted in Figure 9.5)(b), (d) and (f). They display similar behaviour to that of the surface elevation.



(a)



(b)



(c)
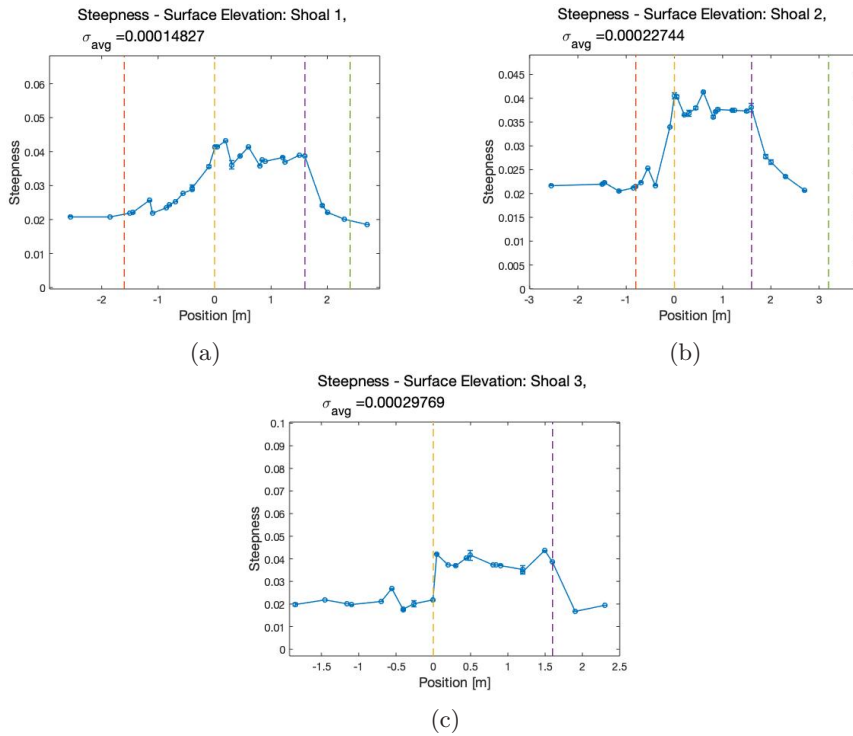
Figure 9.1: This figure compares the steepness of the surface elevation of shoal 1: (a), shoal 2: (b), and shoal3: (c).
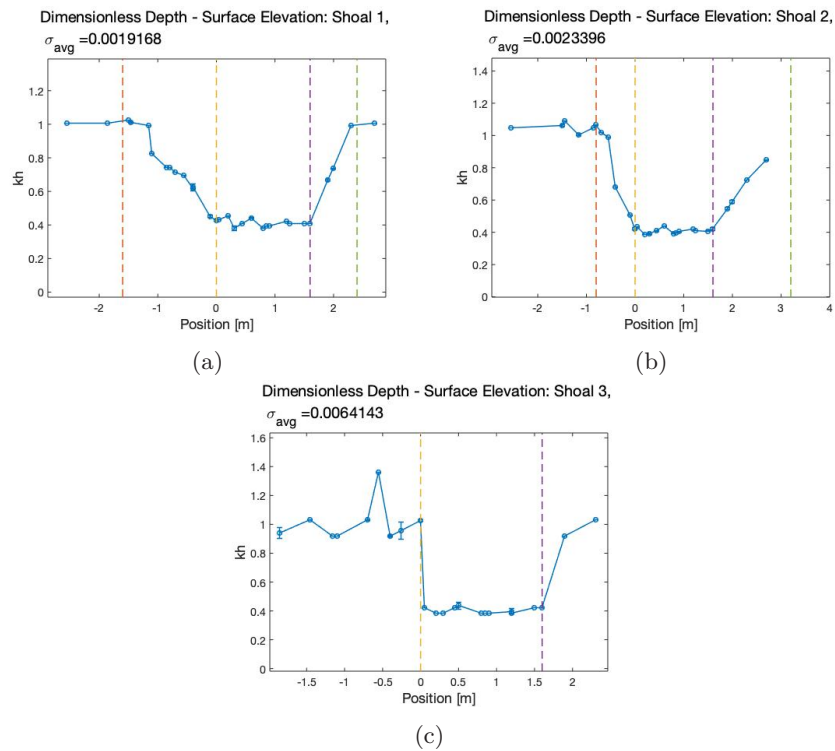
Figure 9.2: This figure compares the dimensionless depth of the surface elevation of shoal 1: (a), shoal 2: (b), and shoal3: (c).
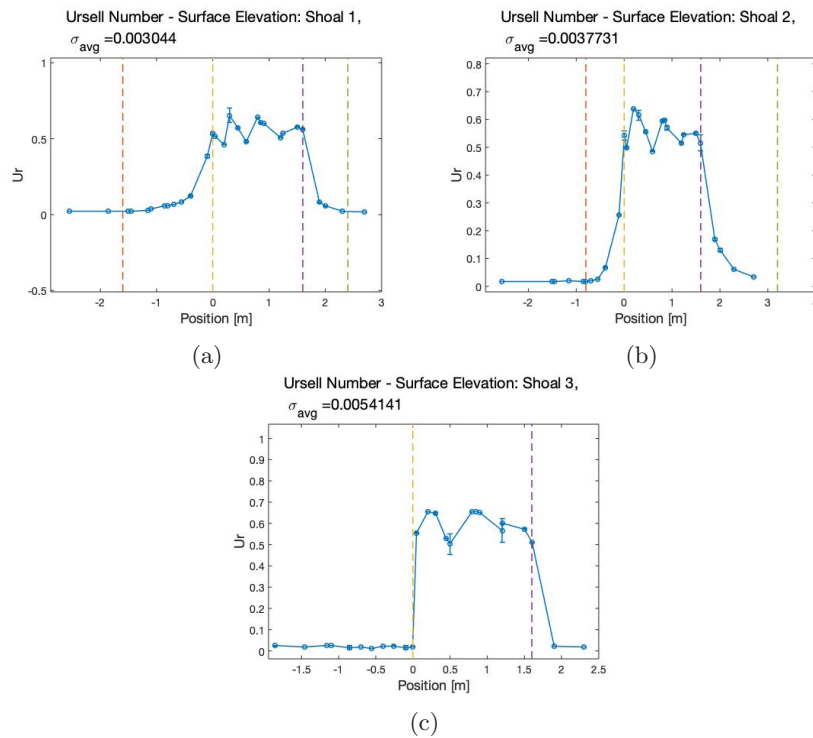


Figure 9.3: This figure compares the Ursell number of the surface elevation of shoal 1: (a), shoal 2: (b), and shoal3: (c).

(a)

(b)

(c)

(d)

(e)

(f)
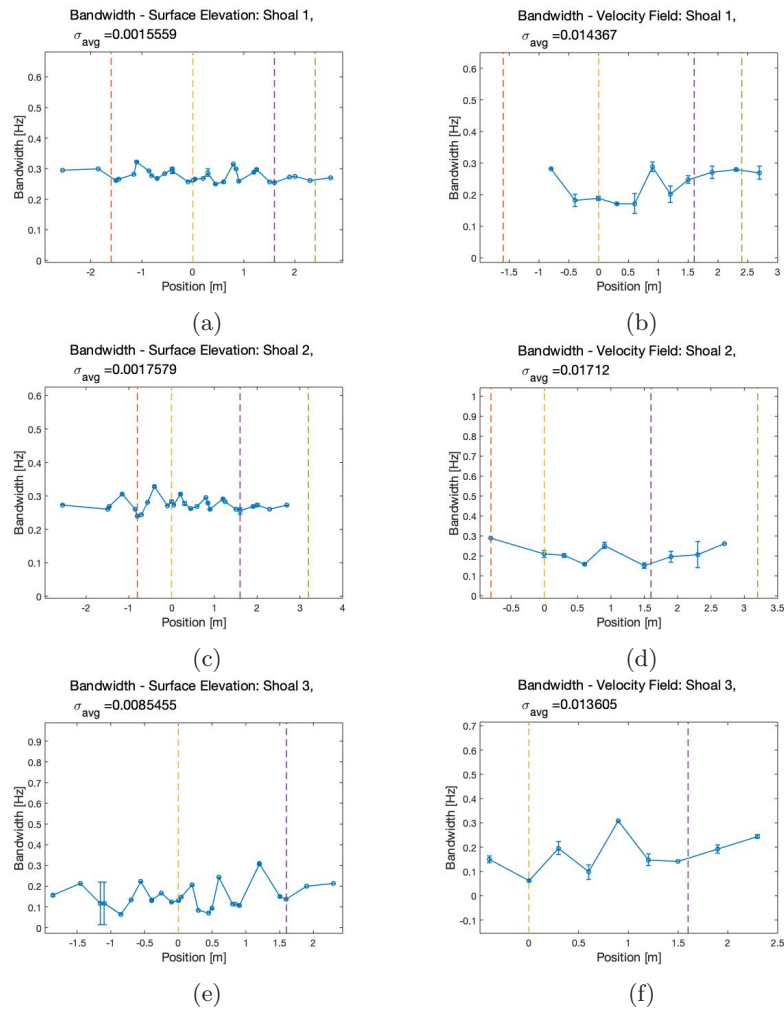
Figure 9.4: This figure compares the bandwidth of the surface elevation of shoal 1: (a), shoal 2: (c), and shoal3: (e) and the bandwidth of the velocity field of shoal 1: (b), shoal 2: (d), and shoal3: (f).
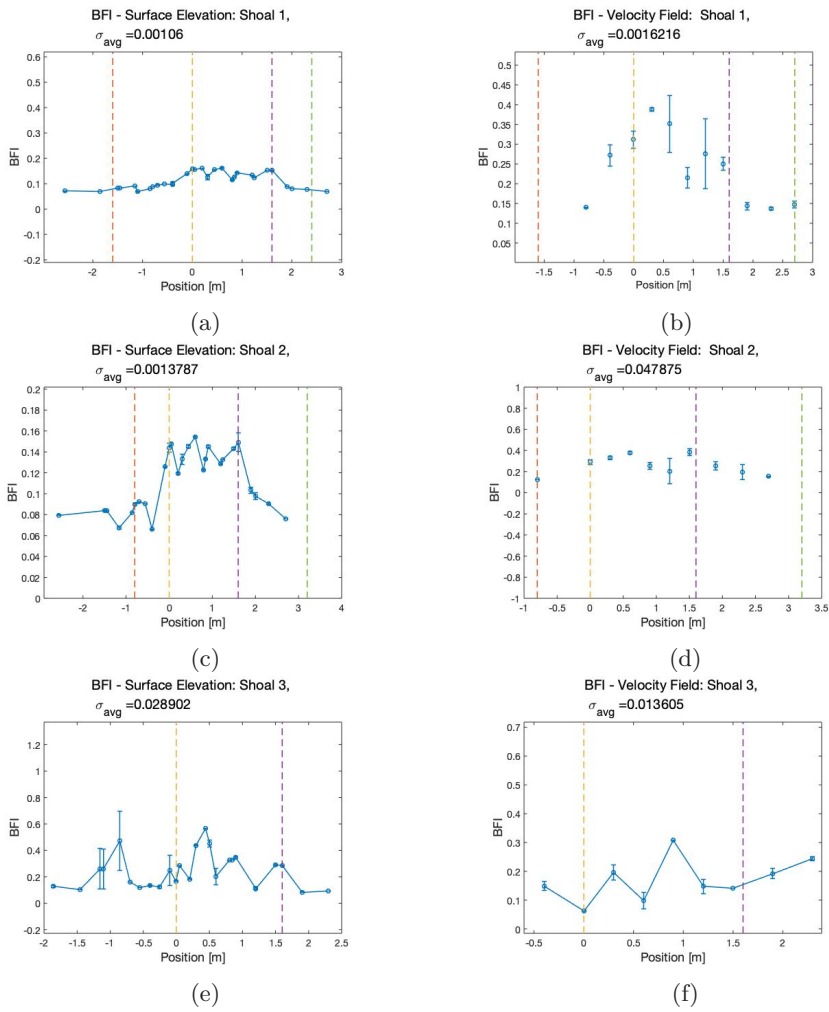
Figure 9.5: This figure compares the BFI of the surface elevation of shoal 1: (a), shoal 2: (c), and shoal3: (e) and the BFI of the velocity field of shoal 1: (b), shoal 2: (d), and shoal3: (f).

## 9.2 Automoments

This section presents the autoskewness and autokurtosis of the surface elevation and velocity field for shoal 1, 2 and 3. The theoretical background for this analysis can be found in Section 3.3. The results in each point are an average of the three runs at the same position. The autoskewness and autokurtosis are calculated through function created for this thesis to include an 'omitnan' option.

Figure 9.6(a) shows that the autoskewness of the surface elevation increases abruptly at the start of the plateau at $x = 0$ m and reaches a maximum of 0.6393 at $x = 0.5$ m. From $x = 0.4450$ m to $x = 0.9$ m the surface elevation autoskewness is above 0.5 and we categorise the distribution of the surface elevation as fairly asymmetric with a elongated or fatter right tail. At $x = 2$ m the autoskewness drops to $-0.1040$ and continues to drop to $-0.1266$ at 2.3 m.

By contrast, in Figure 9.6(b) we cannot see the same significant asymmetry in the velocity distribution. At $x = 0.6$ m the autoskewness of the velocity field reaches a maximum of 0.2253 which would characterize the distribution as fairly symertical. Furthermore, at $-0.8$ m the velocity field autoskewness is $-0.0574$. The autoskewness of the velocity field starts slightly negative and transitions to a positive autoskewness.

By comparing the simultaneous velocity field and surface elevation autoskewness in Figure 9.7, we see that they follow the same trend with a rapid increase and peak on the shoal plateau. Then, the autoskewness rapidly decreases as the processes pass the slope behind the plateau and then seems to return back to initial values the initial autoskewness.

Surprisingly, Figure 9.7 shows that even if we radically alter the shape of the shoal the wave process behaves in a very similar manner. The autoskewness of the surface elevation abruptly increases at the the start of the plateau, reaches a peak and decreases before the end of the plateau. The autoskewness drops further on the slope after the shoal to reach a minima and then increases slightly. The individual plots of the autoskewness of the surface elevation and velocity field of shoal 2 and shoal 3 can be found in appendix A.
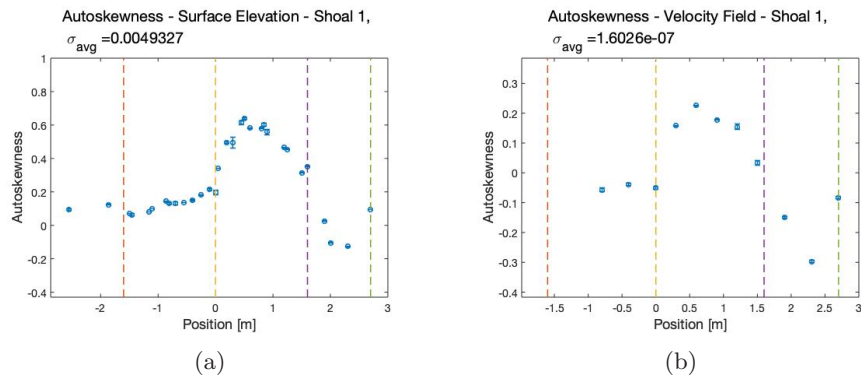


Figure 9.6: Figure (a) displays the autoskewness of the surface elevation as it propagates over shoal 1.Figure (b) displays the autoskewness of the velocity field as it propagates over shoal 1.
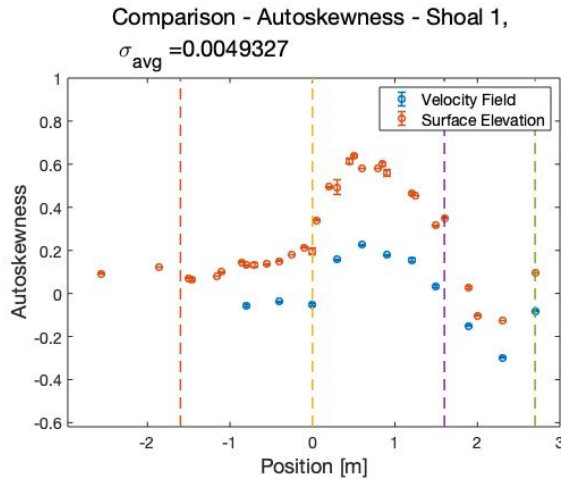
Figure 9.7: Comparison between the autoskewness of the surface elevation and velocity field as the process propagates over shoal1.



(a)                                                    (b)
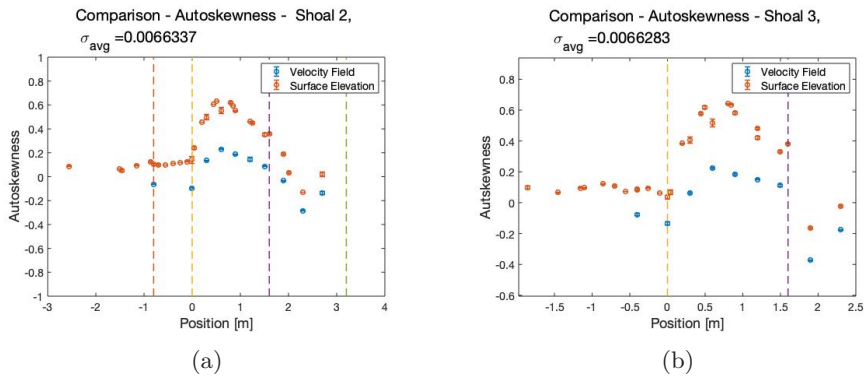
Figure 9.8: Figure (a) compares the autoskewness of the surface elevation and velocity field as the process propagates over shoal2. Figure (b) compares the autoskewness of the surface elevation and velocity field as the process propagates over shoal3.

Figure 9.9(a) shows that the surface elevation autokurtosis is quite stable as the process propagates towards the shoal. As the process passes $x = 0$ m the autokurtosis of the surface elevation sharply increases and reaches a peak at $x = 0.5$ m. The location of the maximum surface elevation autokurtosis is the same as the location of the maximum surface elevation autoskewness. Moreover we see a very small dip in autokurtosis after the shoal plateau. However, we cannot be certain that this dip is significant as we have similar values as before the shoal.

The behaviour of the velocity field autokurtosis, Figure 9.9(b) is the antithesis of the surface elevation autokurtosis. As the process passes $x = 0$ m the autokurtosis of the velocity field decreases and reaches a minima at $x = 0.6$ m. As the process reaches the downward slope the autokurtosis of the velocity field reaches a maxima at $x = 2.3$ m.

Figure 9.10 compares the surface elevation and velocity field autokurtosis and the results are striking. It seems as if the surface elevation and velocity field behave independently from each other and have their separate maxima, and minima, at different locations. This is remarkable as deterministic wave theory teaches us that if we understand the behaviour velocity field then we also know the behaviour of the surface elevation. The two should be inextricably linked.

Figure 9.11 shows that even when the shoal changes, the behavioural pattern of the autokurtosis of the surface elevation and velocity field remains the same. The autokurtosis of the surface elevation of shoal 2 and shoal 3 both have a maximum at $x = 0.6$ m. Immediately after shoal 3, the velocity field has a large maximum, with a kurtosis of 3.14 at $x = 1.9$ m. This is the largest maximum achieved by the velocity field for any of the three different shoals.
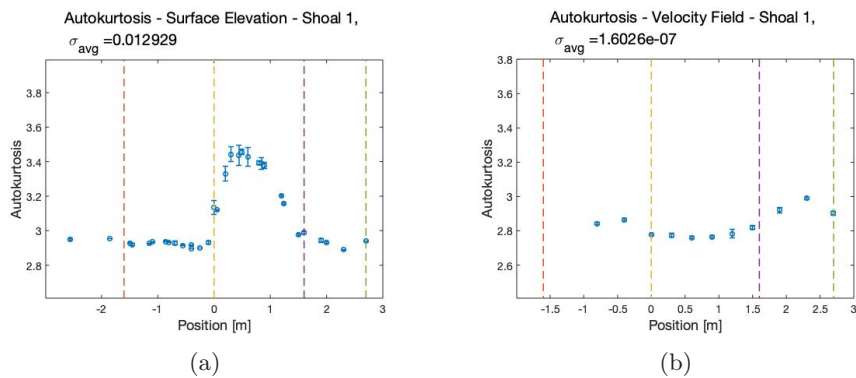


Figure 9.9: Figure (a) displays the autokurtosis of the surface elevation as it propagates over shoal 1. Figure (b) displays the autokurtosis of the velocity field as it propagates over shoal 1.
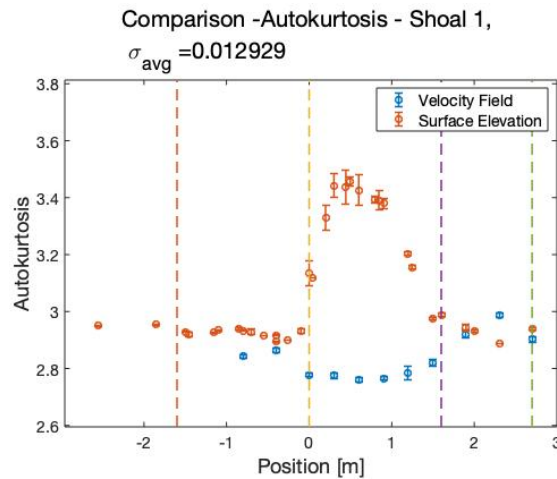


Figure 9.10: Comparison between the autokurtosis of the surface elevation and velocity field as the process propagates over shoal 1.

60
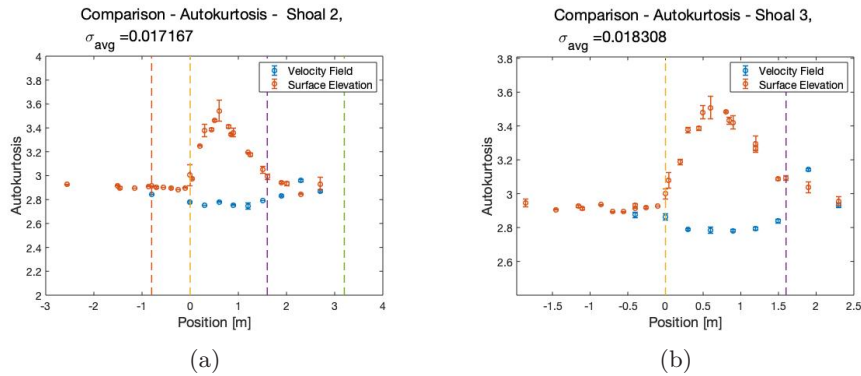
Figure 9.11: Figure (a) compares the autokurtosis of the surface elevation and velocity field as the process propagates over shoal 2. Figure (b) compares the autokurtosis of the surface elevation and velocity field as the process propagates over shoal 3.

## 9.3 Comoments

In this section we view the results from the comoment analysis for shoal 1, 2 and 3. The theoretical background can be found in Section 3.3. As in the last section, the results in each position are an average of the results of each run. Furthermore, the coskewness and cokurtosis are found using a mean of $Z1$ and $Z2$ and not using the $V_x$best algorithm. Earlier studies have not included comoments.

Figure 9.12 shows the correlation between surface elevation and velocity field for the process that propagates over shoal 1. For every position the correlation is above 0.89 except at $x = 1.5$ m where the correlation is 0.8319. Notably, the correlation is much higher after the shoal plateau. Figure 9.13 depicts the correlation between surface elevation and velocity field for shoal 2. We see the same trend of higher correlation after the shoal plateau than on the shoal plateau, and a lower correlation at $x = 0$ m. In addition, the correlation between the surface elevation and velocity field for shoal 3, Figure 9.14, shows a significantly lower correlation on the shoal plateau compared to before or after the shoal. The lowest correlation is 0.8578 at $x = 0.3$ m compared to 0.8989 at $x = -0.4$ m and 0.9626 at $x = 1.9$ m.

There are two types of coskewness for bi variate simultaneously distributed variables. The first is $\gamma_{2,1}$, Equation (3.15), and the second is $\gamma_{1,2}$, Equation (3.16). For all analysis of simultaneously distributed variables in this thesis we define the ADV measurements in x-direction as our $X$ variable and the ultrasound probes as our $Y$ variable.

Figure 9.15 displays the coskewness of surface elevation and velocity field as the process passes over shoal 1. We see that both versions of coskewness have the same shape as the autoskewness. They increase to a peak as the process passes the shoal plateau and then rapidly decrease before the end of the shoal plateau. The coskewness also has a minima at on the downward slope. We also note that (1,2)coskewness displays significantly higher values than (2,1)coskewness.
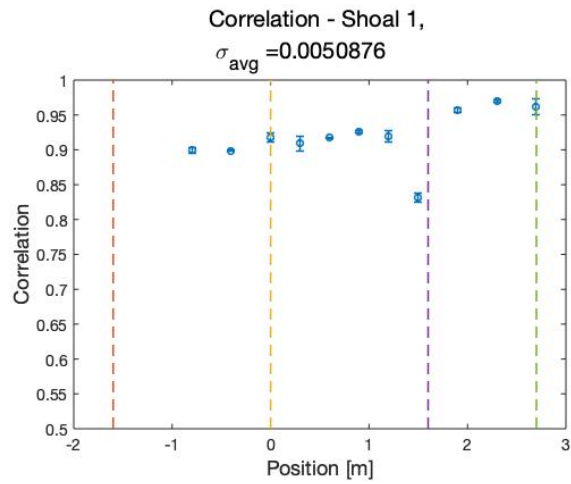
Figure 9.12: Correlation between surface elevation and velocity field for shoal 1.
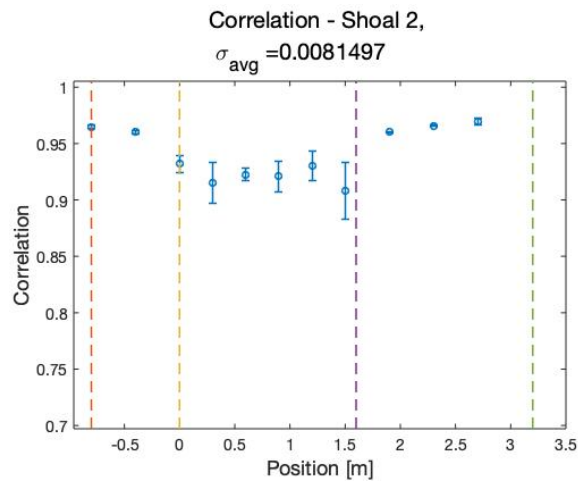


Figure 9.13: Correlation between surface elevation and velocity field for shoal 2.

Moreover, we see the coskewness of shoal 2, Figure 9.16, behave in a very similar manner. The form of both (1,2)coskewness and (2,1)coskewness for shoal 2 is almost identical to that of (1,2)coskewness and (2,1)coskewness for shoal 1.

By contrast, the coskewness of shoal 3, Figure 9.17, does not display the rapid decrease. Both versions of coskewness, for shoal 3, reach a maximum at $x = 0.6$ m and have minima after the shoal plateau.
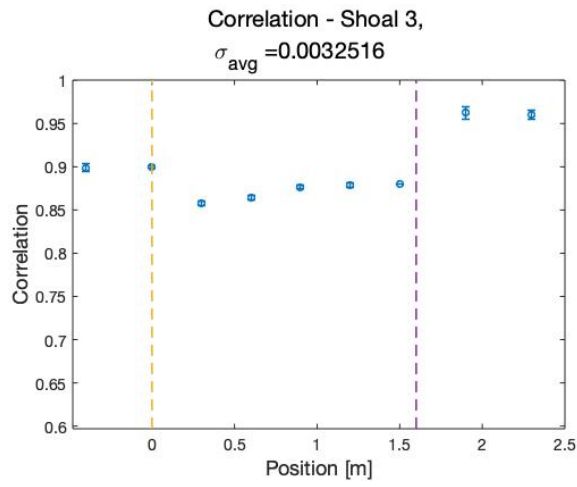
Figure 9.14: Correlation between surface elevation and velocity field for shoal 3.
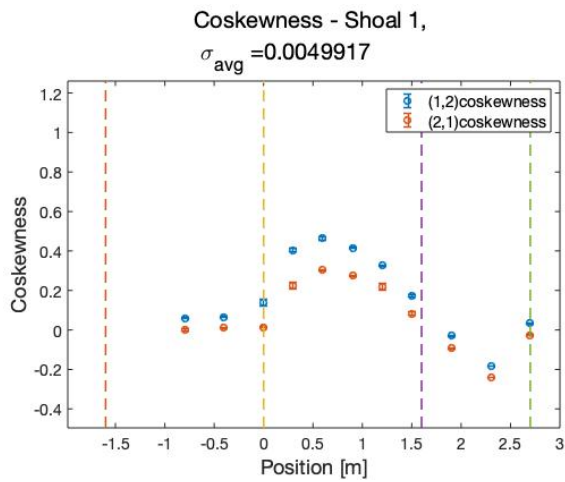


Figure 9.15: Coskewness of velocity field and surface elevation at different positions along the tank. Shoal1.
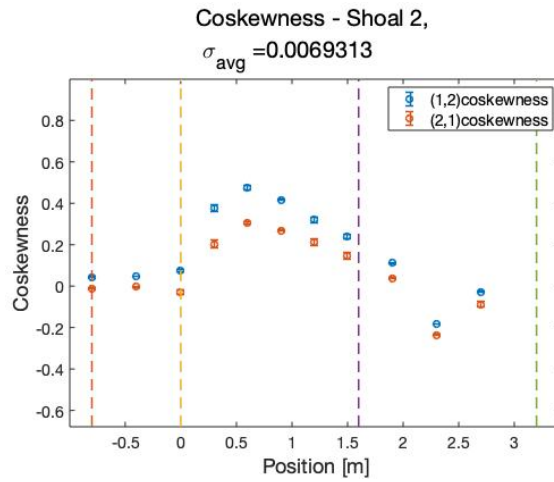
Figure 9.16: Coskewness of velocity field and surface elevation at different positions along the tank. Shoal2.
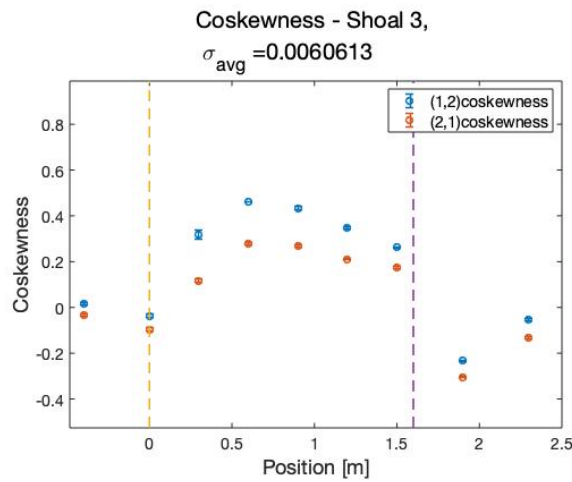


Figure 9.17: Coskewness of velocity field and surface elevation at different positions along the tank. Shoal3.

There are three types of cokurtosis for bi variate simultaneously distributed variables: (2,2)cokurtosis found in Equation (3.17), (3,1)cokurtosis found in Equation (3.18), and (1,3)cokurtosis found in Equation (3.19).

In Figure 9.18 we see that the the mix of the velocity field and surface elevation affects the form of the cokurtosis in the sense that (1,3)cokurtosis is much larger than (3,1)cokurtosis. As a reminder the numbers 1 and 3 in (1,3)cokurtosis refers to the exponentials in the cokurtosis function. Additionally, in (1,3)cokurtosis the velocity field part is to the power of 1, whilst the surface elevation is to the power of 3. Notably, (3,1)cokurtosis has a local minimum at $x = 0.3$ m whilst both (2,2)cokurtosis and (1,3)cokurtosis are increasing. Moreover, we see that all three cokurtosis have a minimum at $x = 1.5$ m. This minimum is

not as prevalent for all the of the cokurtosis for shoal 2, Figure 9.19 or shoal 3, Figure 9.20.

The cokurtosis' of shoal 2 demonstrates the clear importance of the mix of ADV and probes on the final cokurtosis. Yet, this effect seems more minimal than for shoal 1. We also see that the different (2,2)cokurtosis seems to have a peak earlier than (1,3)cokurtosis. Contrarily, we see that (3,1)cokurtosis does not increase until after the shoal plateau.

Similarly, although all the cokurtosis' of shoal 3 have a local maxima on the shoal plateau, all of the cokurtosis' have a larger maxima just behind the shoal plateau.
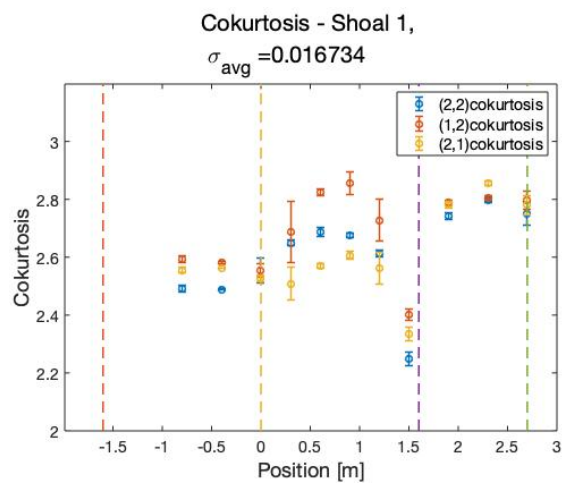


Figure 9.18: Cokurtosis of velocity field and surface elevation at different positions along the tank. Shoal 1.
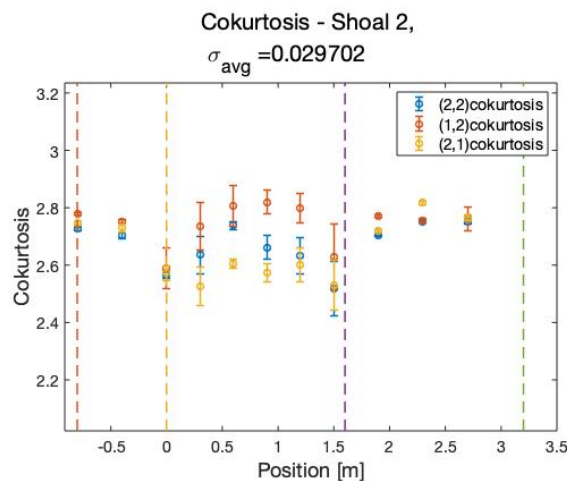


Figure 9.19: Cokurtosis of velocity field and surface elevation at different positions along the tank. Shoal 2.
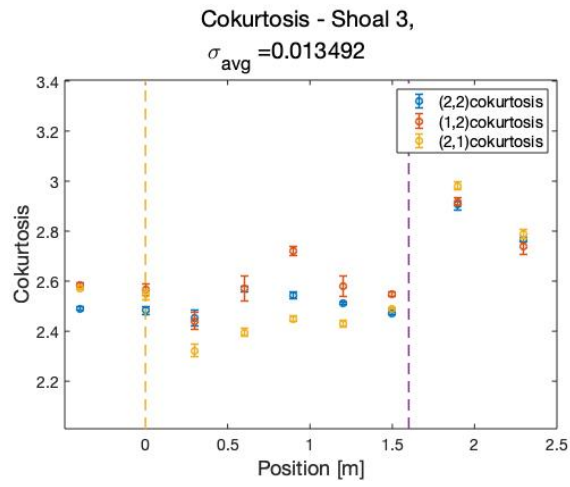
Figure 9.20: Cokurtosis of velocity field and surface elevation at different positions along the tank. Shoal 3.

## 9.4 Probability Estimate

The results in this section compares the probability distribution of the data to that of a normal distribution. Due to time constraints we limit our analysis to shoal 1.

Firstly, we study quantile to quantile plots, thereafter Q-Q plots. They compare the probability distribution of the experimental data to that of a theoretical normal distribution by plotting their quantiles against each other, Wilk and Gnanadesikan (1968). The Q-Q plots are generated through MATLABs `qqplot(x)`

Secondly, we use kernel density estimation, through MATLABs `ksdensity(x)`, to estimate a probability density function, at specific locations along the tank, for our experimental data.

### Q-Q plots

For the Q-Q plots, Figure 9.21 and Figure 9.22, the surface elevation, or velocity field, is represented in blue and the normal distribution is the $45°$ red line.

Figure 9.21(a) and Figure 9.22(a) shows the the center quantiles of the surface elevation and velocity field distributions align with the quantiles one would expect from a normal distribution. We see that the experimental data primarily deviates from a normal distribution in the tails. Moreover, Figure 9.21(a) shows that the probability distribution of the surface elevation at $x = 0$ m is highly similar to a normal distribution with the exception that in the left tail the surface elevation quantiles sharply decrease and in the right tail some quantiles are slightly above Gaussian values. The probability distribution of the velocity field in Figure 9.22(a) shows a larger deviation from a normal distribution compared to Figure 9.21(a). The quantiles in the left tail are larger than expected from a normal distribution whilst the quantiles in the right tail are less than a normal distribution.

As the wave process continues to propagate to $x = 0.9$ m we see that the tails of the probability distribution of the surface elevation, in Figure 9.21(b), have increased in size. The quantiles of the right tail have grown significantly from Figure 9.21(a), and are much higher than that of a normal distribution. Furthermore, we see that the left tails have also grown and the surface elevation quantiles are much greater than Gaussian ones, before they suddenly drop off. The tails of the velocity field probability distribution, in Figure 9.22(b), have also grown. However, the tails of the velocity field distribution behave very differently compared to the tails of the surface elevation. In Figure 9.22(b) we see that the left tail is much greater than the expected normal distribution, and the right tail is much less than the normal distribution.

In Figure 9.21(c) we see that the right tails has reduced in size whilst the left tail still has a similiar shape to that of Figure 9.21(b). Similarly, we see that in in Figure 9.22(c) the right tail is slightly reduced and the left tail is similar to Figure 9.22(b).

As the process has propagated beyond the shoal to $x = 2.7$ m, Figure 9.21(d) and Figure 9.22(d), we see that the change becomes even more stark. The right tail of the surface elevation probability distribution,Figure 9.21(d), has

gone from being much larger compared to a normal distribution to a little less that the quantiles given by a normal distribution. Whilst, the deviation from a normal distribution in left tail has significantly reduced. Likewise, the deviation in left and right tail from a normal distribution have been significantly reduced in Figure 9.22(d).
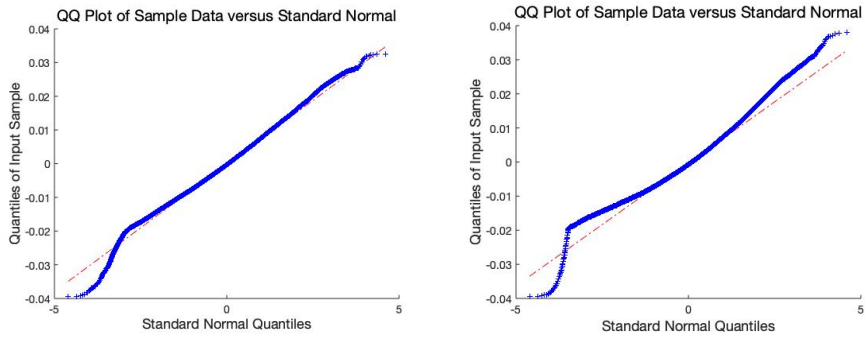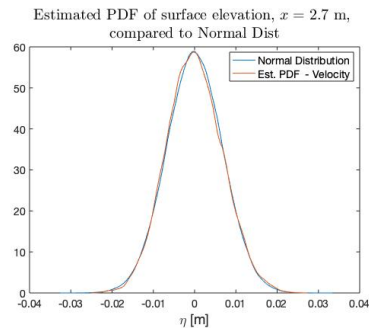


(a) Shows the measurement of the probe placed at $x = 0$ m.



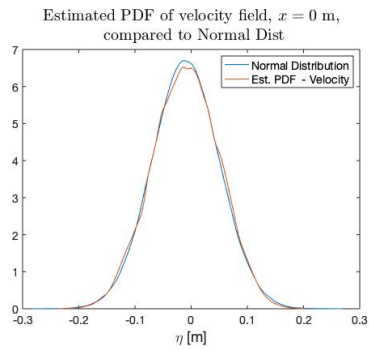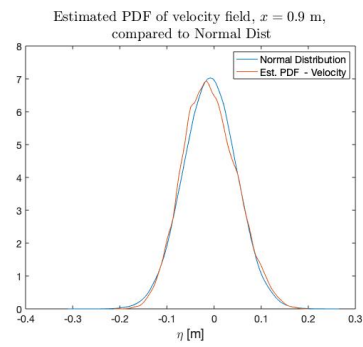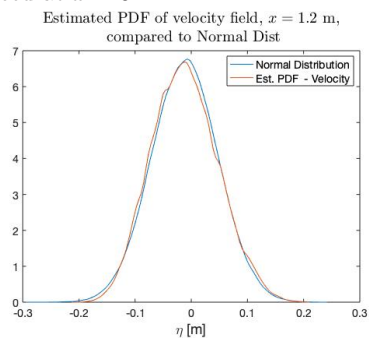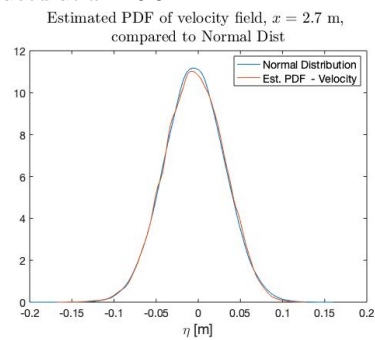(b) Shows the measurement of the probe placed at $x = 0.9$ m.
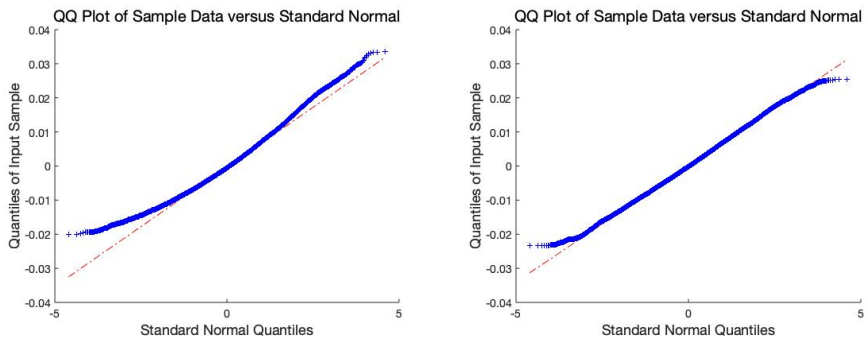


(c) Shows the measurement of the probe placed at $x = 1.2$ m.



(d) Shows the measurement of the probe placed at $x = 2.7$ m.

Figure 9.21: This figure shows Q-Q plots of the surface elevation at different locations along the tank.
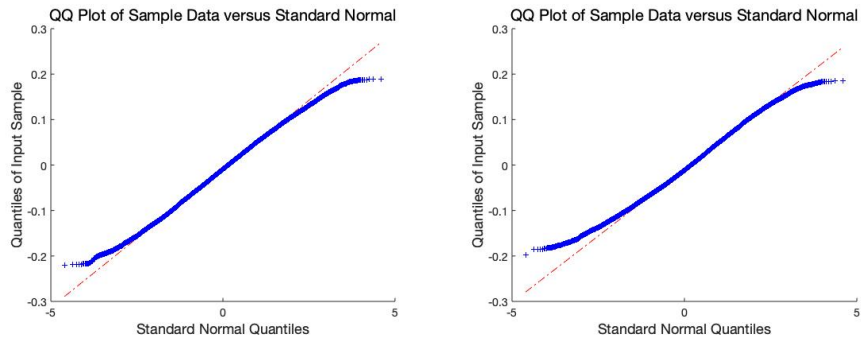
(a) Shows the measurement of the probe placed at $x = 0$ m.

(b) Shows the measurement of the probe placed at $x = 0.9$ m.
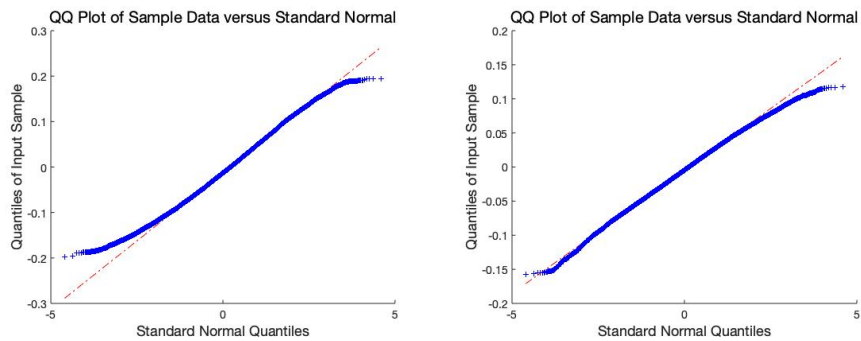
(c) Shows the measurement of the probe placed at $x = 1.2$ m.

(d) Shows the measurement of the probe placed at $x = 2.7$ m.

Figure 9.22: This figure shows Q-Q plots of the velocity field at different locations along the tank.

### Estimated Probability Density Function

We continue our analysis of the probability distributions of the surface elevation and velocity field by comparing their estimated PDFs with that of a normal distribution.

Figure 9.23(a) we that the estimated pdf of the the surface elevation is very similar to that of a normal distribution. Likewise, Figure 9.24(a) the velocity field PDF is also similar to that of a normal distribution.

As the process propagates to $x = 0.9$ m we see that the surface elevation PDF, Figure 9.23(b), has changed form by developing an elongated right tail an the mode has shifted to the left. The same trend is visible in Figure 9.24(b) as the mode has shifted a little to the left.

We observe that as the process propagates further, to $x = 1.2$ m the shape of Figure 9.21(c) has shifted back towards a normal distribution as the elonglongated tail seen in Figure 9.23(b) has retracted slightly and the mode has moved towards the middle of the probability distribution. The shape of the velocity field distribution, Figure 9.22(c) seems almost Gaussian. It is clear that the probability distribution of the surface elevation and the probability of the velocity field probability distribution behave differently from each other.

After the shoal, at $x = 2.7$m we see that the probability distribution of the surface elevation, Figure 9.23(d) , has returned to resemble a Gaussian distribution. Likewise, the probability distribution of Figure 9.24(d) also seems to resemble a Gaussian distribution with the exception that the mode is shifted a little to the right.
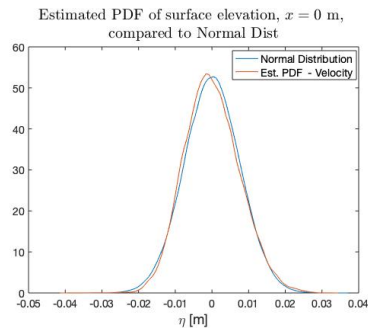


(a) Shows the measurement of the probe placed at $x = 0$ m.
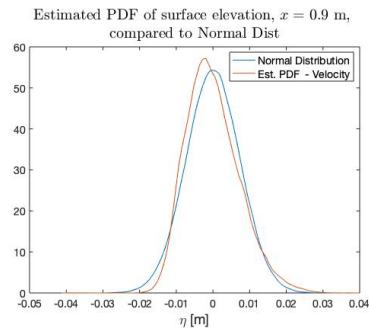


(b) Shows the measurement of the probe placed at $x = 0.9$ m.
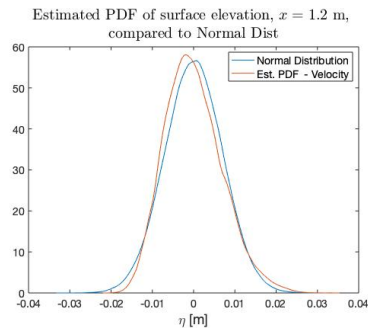


(c) Shows the measurement of the probe placed at $x = 1.2$ m.



(d) Shows the measurement of the probe placed at $x = 2.7$ m.

Figure 9.23: This figure compares estimated PDFs of the surface elevation at different locations along the tank.

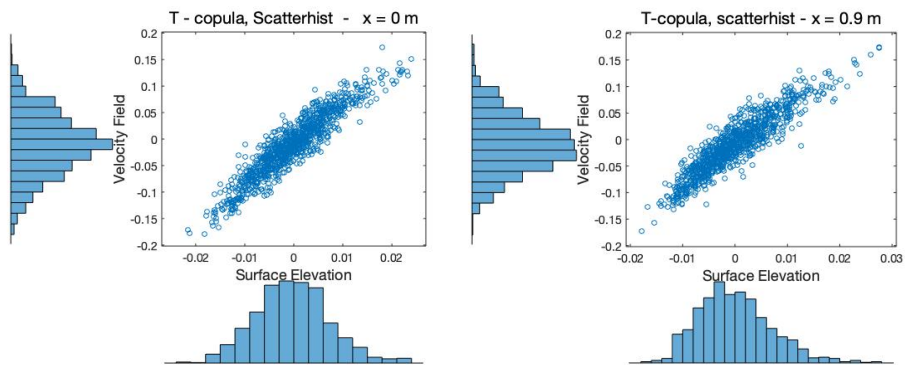(a) Shows the measurement of the probe placed at $x = 0$ m.



(b) Shows the measurement of the probe placed at $x = 0.9$ m.



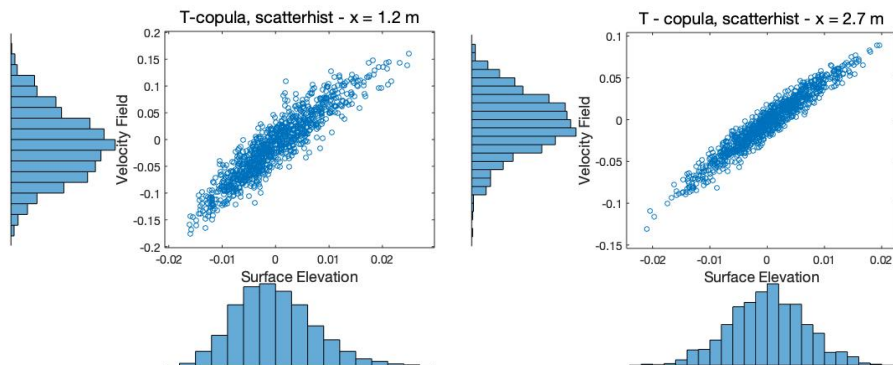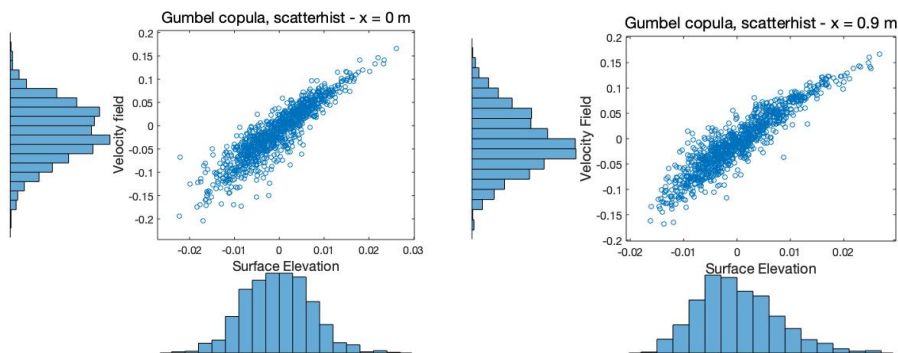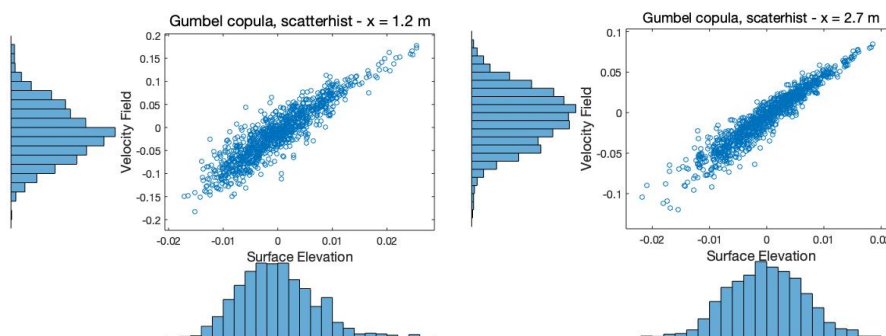(c) Shows the measurement of the probe placed at $x = 1.2$ m.



(d) Shows the measurement of the probe placed at $x = 2.7$ m.

Figure 9.24: This figure compares estimated PDFs of the velocity field at different locations along the tank.

71

## 9.5 Copula

This section introduces three different copulae and attempts to describe the dependence structure of the surface elevation and velocity field. The theoretical background can be found in Section 3.5. The copula is fitted to the data using maximum likelihood using MATLABs `copulafit`. The estimation methodology used in this thesis is inspired by Bouyé et al. (2000).

To best visualise the dependence structure we use scatter-histograms which plot histograms of the marginals of the surface elevation and velocity field on the axis of a scatter plot. The scatter plot contains simulated data distributed by the copula created based on the surface elevation and velocity field.

Figure 9.25 presents the development of Gaussian copulae, Equation (3.28), as the stochastic process propagates along the tank. It seems as if the marginals are quite similar, although the marginals of the surface elevation, on the x-axis, have noticeably longer tails. A Gaussian copula does not have tail dependence, i.e. there is no change in the relationship between the surface elevation and velocity field for very large or very small values.

Figure 9.26 depicts the development of T-copulae, Equation (3.29), as the process propagates a long the tank. The trend of the marginal probability distribution of the surface elevation be skewed as the process propagates is also evident when using the T-copula. The T-copula has both positive and negative tail dependence of the same magnitude.

Figure 9.27 displays the development of Gumbel-copulae, Equation (3.30), as the process propagates along the tank. A Gumbel copula has positive tail dependence but not negative tail dependence. This means that if $X_1$ reaches large extreme values there is a tendency for $X_2$ to reach large extreme values as well.

For all three copulae, Figure 9.25, Figure 9.26, and Figure 9.27, we see that the copula distributed simulated data become more concentrated along the diagonal axis of the scatter plot.

The copula that best fits our data is the one that minimises the Akaike information criterion, AIC, Equation (3.31). We see from Section 10.2 that for all positions it is the T-copula that minimises AIC. For positions $x = 0$ m, $x = 1.2$ m, $x = 2.7$ m the second best fit is the Gaussian copula. At $x = 0.9$ m the second best fit is the Gumbel copula.

| x [m] Copula | AIC | | | |
|---|---|---|---|---|
| | 0 | 0.9 | 1.2 | 2.7 |
| T | $-4.97 \times 10^5$ | $-4.89 \times 10^5$ | $-4.72 \times 10^5$ | $-6.69 \times 10^5$ |
| Gaussian | $-4.63 \times 10^5$ | $-4.71 \times 10^5$ | $-4.66 \times 10^5$ | $-6.66 \times 10^5$ |
| Gumbel | $-4.60 \times 10^5$ | $-4.72 \times 10^5$ | $-4.53 \times 10^5$ | $-6.30 \times 10^5$ |

Table 9.1: The AIC of three different copulas at four different locations of Shoal 1. x is the position of the probe.
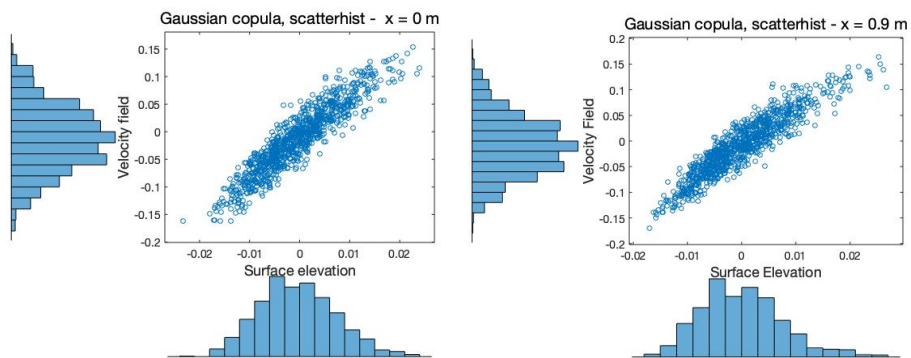
(a) Shows the measurement of the probe placed at $x = 0$ m.



(b) Shows the measurement of the probe placed at $x = 0.9$ m.
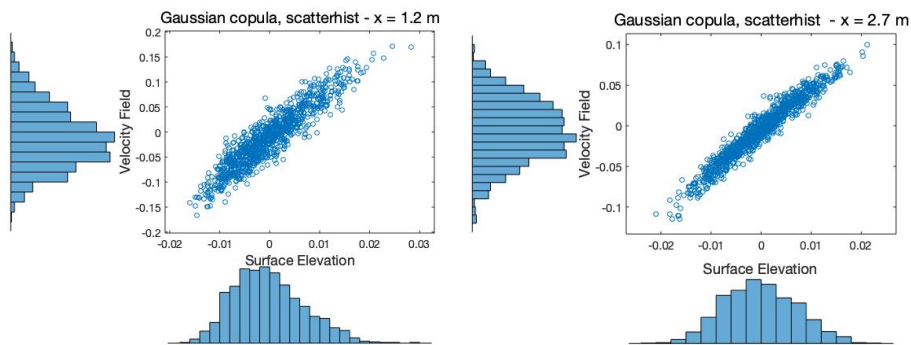


(c) Shows the measurement of the probe placed at $x = 1.2$ m.



(d) Shows the measurement of the probe placed at $x = 2.7$ m.

Figure 9.25: The figure shows the development of a Gaussian copula as the stochastic process propagates along the tank. The surface elevation is on the x-axis and the velocity field is on the y-axis. The histograms describing the marginal distributions are also shown on their respective axis.

(a) Shows the measurement of the probe placed at $x = 0$ m.



(b) Shows the measurement of the probe placed at $x = 0.9$ m.



(c) Shows the measurement of the probe placed at $x = 1.2$ m.



(d) Shows the measurement of the probe placed at $x = 2.7$ m.

Figure 9.26: The figure shows the development of a T-copula as the stochastic process propagates along the tank. The surface elevation is on the x-axis and the velocity field is on the y-axis. The histograms describing the marginal distributions are also shown on their respective axis.

(a) Shows the measurement of the probe placed at $x = 0$ m.



(b) Shows the measurement of the probe placed at $x = 0.9$ m.



(c) Shows the measurement of the probe placed at $x = 1.2$ m.



(d) Shows the measurement of the probe placed at $x = 2.7$ m.

Figure 9.27: The figure shows the development of a Gumbel copula as the stochastic process propagates along the tank. The surface elevation is on the x-axis and the velocity field is on the y-axis. The histograms describing the marginal distributions are also shown on their respective axis.

# CHAPTER 10

# Discussion

This chapter is dedicated to discussing and interpreting the results and their limitations, as well as placing them in an academic context. Section 10.1 discusses the results of Experiment 1. Section 10.2 discusses the results of Experiment 2. Section 10.3 considers the limitations of the research.

## 10.1 Experiment 1

Experiment one studies the evolution of two narrow banded spectra as they propagate along a wave tank with uniform bathymetry. The experimental setup of experiment 1 can be found in Section 7.1. The results of experiment 1 can be found in Chapter 8.

### Mechanical Parameters

It is clear from Figure 8.1 that the steepness of both the Gaussian 1 and Gaussian 2 wave processes is decreasing as the wave processes propagate along the tank. A decrease in steepness is may sometimes be an indicator of a decrease of the nonlinearity of the wave process.

From Figure 8.2 we see that the dimensionless depth is reasonably stable. However, we see a clear downshift in figure Figure 8.2(a) which we suspect is due to the wave spectra of the surface elevation experiencing a frequency downshift.

It is clear that using the half peak half width method of estimating the bandwidth of a wave spectra undergoing asymmetric spectral deformation produces significant errors. In future the bandwidth should be estimated in another manner. Moreover, due to the unreliability of the bandwidth estimation the BFI calculation is called into question.

Nonetheless, there are a few insights we can gleam from the BFI. The first is that the Gaussian 2 surface elevation BFI is decreasing as the wave process propagates along the tank. This steams form the Gaussian 2 steepness decreasing. Additionally, the initial BFI is much higher for the surface elevation of the Gaussian 1 compared to the Gaussian 2 process.

**Statistics**

The autoskewness of the surface elevation of Gaussian 1 increases as the process propagates, Figure 8.10. This indicates that the probability distribution of the surface elevation is developing a slight elongated right tail. However, the autoskewness is still fairly small and the probability distribution would still be characterised as symmetric. There may be a slight increase in in the autoskewness of Gaussian 2, however, it is very slight.

Figure 8.13 compares the autokurtosis of the velocity field and the surface elevation of Gaussian 1 and Gaussian 2. It is clear that the increased amplitude factor in Gaussian 1 increases the rate at which the surface elevation autokurtosis increases compared to Gaussian 2. Aditionally, it is also evident that the surface elevation autokurtosis increases much faster than the autokurtosis of the velocity field for the wave process with a higher amplitude factor, Gaussian 1. Comparatively, the increase in the autokurtosis of the surface elevation and velocity field are very similar for the wave process with a lower amplitude factor, Gaussian 2.

By considering the autoskewness and the autokurtosis of the velocity field and surface elevation of Gaussian 1, we notice that the tails in both ends of the probability distributions grow. This means that as the wave process propagates the risk of very large waves and very small waves increases. Similarly, the risk of very high velocities and very low velocities increase.

**Spectral Analysis**

Figure 8.14(a) compares the power spectral density of the surface elevation of Gaussian 1 at 2 m and 18 m. Figure 8.14(b) compares the power spectral density of the surface elevation of Gaussian 2 at 6 m and 18 m. This image is extremely similar to Figure 2 in K. B. Dysthe et al. (2003). They used numerical simulations to study the evolution of fairly narrow banded gravity wave spectra. K. B. Dysthe et al. (2003)'s Figure 2 is the result of changing the bandwidth of a wave process and keeping the amplitude factor constant, and our Figure 8.14 is the result of changing the amplitude factor and keeping the bandwidth the same. These are two different methods of achieving the same thing, which is studying the effects of two wave spectra with different initial BFI. Figure 2(a) has a bandwidth of $\Delta = 0.1$ Hz and Figure 2(b) has a bandwidth of $\Delta = 0.3$ Hz. Since, BFI is defined as steepness over bandwidth. Thus, Figure 2(a) will have a higher initial BFI than Figure 2(b). Figure 8.14(a) has an amplitude factor of $\alpha = 0.05$ and Figure 8.14(b) has an amplitude factor of $\alpha = 0.025$. This means that Figure 8.14(a) will have a higher initial BFI than Figure 8.14(b).

Moreover in Figure 8.14 we see two effects clearly. The first is a frequency downshift and the second is spectral deformation. The frequency downshift is due to nonlinear effects other than modulation instability.

## 10.2 Experiment 2

Experiment 2 studies the effects on non-uniform bathymetry. Although similar experimental research has been conducted in the past, we would like to point to key differences. Firstly, our wave process has a Pierson-Moskowitz wave spectra

whilst previous research, particularly Trulsen, Raustøl et al. (2020), utilised a JONSWAP wave spectra. Secondly, our first two shoals are asymmetric whilst the third is a 'step'. The research in Trulsen, Raustøl et al. (2020) used a symmetric shoal. The experimental setup of experiment 2 can be found in Section 7.1. The results of experiment 2 can be found in Chapter 9.

### Mechanical Parameters

From Figure 9.1, Figure 9.2, and Figure 9.3 we see that as the process propagates over the shoal the steepness increases, the dimensionless depth decreases and the Ursell number increases which all indicate that as the wave process propagates over the shoal it becomes more nonlinear.

Figure 9.4(a), (c), and (e) shows that the bandwidth of the surface elevation, for all three different shoals, has small deviations, but remains somewhat constant. It is difficult to determine if there is a slight increase in the bandwidth of velocity field in Figure 9.4(b), (d), and (f) or if it somewhat constant with significant variability.

Although, the BFI of the surface elevation in Figure 9.5(a), (c), and (e) increases as the wave process propagates over the shoals it is not high enough to indicate that the process is modulationally unstable. The BFI of the velocity field display the same behaviour, Figure 9.5(b), (d) and (f), and are also modulationally stable.

### Automoments

Our results in Figure 9.6, Figure 9.7, and Figure 9.7 are in accordance with several studies which show that the autoskewness of the surface elevation of an irregular velocity field propagating over a shoal will have a maximum on the shoal plateau and an minimum on the downward slope, Trulsen, Zeng and Gramstad (2012), Gramstad et al. (2013), Trulsen, Raustøl et al. (2020), Lawrence, Trulsen and Gramstad (2021).

Similarly, the velocity field autoskewness are also in accordance with the results in Trulsen, Raustøl et al. (2020) and Lawrence, Trulsen and Gramstad (2021).

The maximal autoskewness of the surface elevation, $\gamma_s$, and velocity field, $\gamma_v$, that we achieve is $\gamma_s = 0.64$, $\gamma_v = 0.23$ for shoal 1, $\gamma_s = 0.63_s$, $\gamma_v = 0.20$ for shoal 2, and $\gamma_s = 0.64$, $\gamma_v = 0.22$ for shoal 3. It is striking that even though we dramatically change the shape of the shoal, the values of the autoskewness are very similar. Our values are also very similar to the simulations in Lawrence, Trulsen and Gramstad (2021), where they achieved an autoskewness of $\gamma_s = 0.67$ with $T_p = 1.1$ s, $H_s = 2.5$ cm, and depth $h_1 = 0.53$ m and $h_2 = 0.11$ m. We also see similar values in Trulsen, Raustøl et al. (2020). This is particularly interesting as the wave field in Trulsen, Raustøl et al. (2020) is a JONSWAP spectrum with a peak enhancement factor of 3.3, whilst the wave field in our experiments is a Pierson-Moskowitz spectrum.

Likewise, our autokurtosis results, in Figure 9.9, Figure 9.10, and Figure 9.11 also coincide with other publications, Trulsen, Zeng and Gramstad (2012), Gramstad et al. (2013), Trulsen, Raustøl et al. (2020), Lawrence, Trulsen and Gramstad (2021). It is worth noting that only Trulsen, Raustøl et al.

(2020) and Lawrence, Trulsen and Gramstad (2021) report the autokurtosis of the velocity field. Moreover, in these publications there is variation in the location of the transition zone between upward slope and shoal plateau. In the simulations of Lawrence, Trulsen and Gramstad (2021) we see that the distance from the leading edge of the shoal plateau to the maximum in surface elevation autokurtosis, varies with peak period. Our maximal surface elevation autokurtosis is $\kappa = 3.43$ at 0.5 m for shoal 1, $\kappa = 3.54$ at 0.6 m for shoal 2, and $\kappa = 3.51$ at 0.6 m. The locations of our maxima are fairly similar to the simulated results in Lawrence, Trulsen and Gramstad (2021) with $T_p = 1.1$ s. Furthermore, our results confirm the observation by Lawrence, Trulsen and Gramstad (2021), stating that there is a tendency for the local minimum of the autoskewness of surface elevation and the local maximum of the autokurtosis of the horizontal velocity field to be at the same location.

It is highly noticeable that our maximal autokurtosis is significantly lower than the experimental results in Trulsen, Zeng and Gramstad (2012). This could be attributed to the fact that our experimental results are produced using a Pierson-Moskowitz spectra, however the surface elevation have been filtered and interpolated to remove dropouts. It is a fine line to filter and interpolate the data enough to remove the dropouts, and not alter the shape. Especially, since the autokurtosis is a measure of outliers. Therefore, there is some uncertainty linked to the actual values of autokurtosis. On the other hand, the reader is reminded that our experimental values have all been averaged so that some of the idiosyncratic noise should significantly reduced.

### Comoments

An analysis of the comoments of velocity field and surface elevation in an irregular wave field propagating through inhomogeneous media, has to our understanding never been done before.

When learning about deterministic wave theory, we are taught that if you know the behaviour and the characteristics of the surface elevation then we automatically know the behaviour and the characteristics of the velocity field, Gevik, Pedersen and Trulsen (2021). Therefore, a natural starting point for an analysis of the simultaneous behaviour of the velocity field and surface elevation is to study the correlation between the two, Figure 9.12, Figure 9.13, and Figure 9.14.

The results for shoal 2, and shoal 3 show that the correlation drops as the wave distribution propagates over the shoal before it increases on the lee side of the shoal. The correlation between the surface elevation and velocity field of the wave process that propagates over shoal 1 shares the tendency to increase after the shoal, however, there are some significant deviations.

It is clear from Figure 9.15, Figure 9.16, and Figure 9.17 that the coskewness follows the shape of the autoskewness of the velocity field and surface elevation. This is to be expected as autoskewness of the velocity field and the autoskewness of the surface elevation share the same form. Yet, there is a distinguishable difference in the maximal values of coskewness achieved across the three shoals. With the highest (1,2)coskewness achieved for shoal 1, and the lowest (1,2)coskewness achieved over shoal 3. It seems that as the leading slope of the

79

shoal becomes steeper the coskewness over the shoal decreases.

When comparing the cokurtosis of shoal 1, Figure 9.18, with the correlation in Figure 9.12, we see that at $x = 1.5$ m both the correlation drops and the cokurtosis. If we assume that the velocity field and surface elevation should be highly correlated then the sudden drop in correlation at $x = 1.5$ m for shoal 1 leads to some uncertainty as to the quality of the other comoments at 1.5 m for shoal 1.

A clear trend emerges as we study the cokurtosis of shoal 1, shoal 2, shoal 3 in comparison, Figure 9.18, Figure 9.19, Figure 9.20. The maximal cokurtosis achieved by the wave process, decreases as the shoals leading slope becomes steeper.

### Probability Estimate

From the Q-Q plot of the surface elevation at $x = 0$ m, Figure 9.21(a), we see that it is an almost a completely Gaussian distribution with a few deviations. The left tail has a sharp decrease for the smallest quantiles which probably is due to the filtering process. Our dropouts were located in the wave troughs just after the local minimum. It is unsurprising the that the interpolation may have changed the probability distribution of the wave troughs. Therefore the reader is advised to disregard the sharp decrease in the left tail in the Q-Q plots of the surface elevation.

We see that as our wave process propagates inwards on the shoal, $x = 0.9$ m, the tails of the surface elevation Q-Q plot grows. The quantiles of the left and the right tail are much larger than expected from a Gaussian distribution. This means that more extreme values, outliers, are possible and the risk of rogue waves is greater. Our observations align closely with Cherneva et al. (2005) who states that near Gaussian distributions underestimate the probability of large wave crests.

The Q-Q plot of the surface elevation at $x = 1.2$ m is interesting because the right tail has significantly decreased, lowering the probability of large values for the surface elevation. However, the left tail remains very similar. There is an asymmetric decrease in tail mass.

After the shoal, the quantiles in the right tail have become smaller than the values expected from a Gaussian distribution. Contrarily, the quantiles in the left tail are still larger than expected. This implies that we can expect smaller large values of the surface elevation, and larger small values of the surface elevation than predicted by a Gaussian distribution.

The quantiles of the velocity field behave remarkably different from the quantiles of the surface elevation. The Q-Q plot of the quantiles of the velocity field at $x = 0$ depict a distribution that has some minor deviations from a Gaussian distribution before propagating over the shoal plateau. The quantiles of the right tail are smaller than expected from a Gaussian distribution and the left tail is a larger than expected from a Gaussian distribution. As the wave process propagates over the shoal plateau, these characteristics are strengthened. This means that at $x = 0.9$ m and $x = 1.2$ m we can expect fewer high velocity values compared to a Gaussian distribution and more small velocity values.

After the slope, at $x = 2.7$ m, we see that the quantiles of the left tail have become similar to those of a Gaussian distribution. The quantiles of the right tail are still less than expected of a Gaussian distribution. It seems as if a Gaussian distribution continuously over predicts the largest quantiles of the velocity field.

The estimated probability density functions help in our attempt to understand the behaviour of the stochastic process as it propagates over the shoal. The estimated PDF of the surface elevation tells a distinct tale. As the process enters the shoal it is near Gaussian, it then becomes noticeable asymmetrical with a positive autoskewness. This asymmetry does not last. Even before the end of the shoal plateau the process has started to stabilise and the asymmetry has decreased. After the the shoal, the probability distribution of the surface elevation returns to a near Gaussian distribution.

Due to the probability distribution of the velocity field having small deviations for a Gaussian distribution, it is much harder to interpret the estimate probability distributions. Although we can see the evidence of the autoskewness, especially at 2.7 m where there is a clear left tail.

It striking to compare the way in which the surface elevation and velocity field develop. The two dynamic stochastic processes behave independently of each other. Moreover, we observe that the the wave process is a dynamic stochastic process even when it is characterised by a Pierson-Moskowitz wave spectra without modulation instability. Underlining that even though there is no modulation instability, it does not mean that the nonlinearity of the wave process is unimportant.

### Copulae

Copulae are commonly used within quantitative finance and applied to risk and portfolio management, optimisation and derivatives pricing. Lately, the use of copulae outside of mathematical finance is gaining traction. Copulae are used in reliability analysis of highway bridges in civil engineering, Kilgore and Thompson (2011). Copulae are used in medical research, specifically, magnetic resonance imaging research to segment images, Lapuyade-Lahorgue, Xue and Ruan (2017). Moreover, copulae are used to study the joint statistics of electroencephalographic (EEG) signals, with applications to early diagnosis of Alzheimer's, Iyengar et al. (2010).

The use of copulae in the study of wave processes is also gaining popularity. Corbella and Stretch (2013) used Archimedean copulae to study the dependencies of wave height, wave period, storm duration, water level and storm inter-arrival time using data from the east coast of South Africa. They found that only wave height, wave period, and storm duration have a clear dependence structure. Bai et al. (2020) proposed a joint probability distribution of coastal wind waves using copulae. They include wave height, wind speed, and wave period in their research.

We see from our results that the copula that best describes the dependence between the surface elevation and velocity field is a T-copula, Figure 9.26. This means that the surface elevation and velocity field have positive and negative tail dependence.

The literature review documents numerous publications that research the marginal behaviour of the surface elevation and velocity field respectively. Yet, using copulae to study the dependence structure of the velocity field and surface elevation of an inhomogeneous wave field propagating over a shoal has, as far as the author is aware, not been attempted before.

Using copulae to model the relationship between the surface elevation and the velocity field have several advantages.

The first is that it allows to avoid potential fallacies that arise from dependence models that only use correlation. Although correlation is an extremely useful measure, it has several pitfalls that are not always obvious. According to, McNeil, Frey and Embrechts (2015), correlation is only a natural concept in context the of multivariate normal, or more generally elliptical models, as their copulae depend only on the correlation matrix and characteristic generator. The correlation does not have this parametric role for more general multivariate models. Moreover, the correlation between to random variables is a measure of *linear* dependence and therefor gives us no indication of tail dependence.

Secondly, copulae allow us to build multivariate models from the bottom up. We have a much better understanding of individual behavior of marginal distributions of the surface elevation and velocity field respectively, compared to their dependence structure. Using copulae allows us to combine our more mature understanding of the marginal behavior with a multitude of dependence models and test their fit.

Lastly, copulae assert dependence on a quantile scale which is convenient when we want to study the behavior of rogue waves.

## 10.3 Limitations

All experimental results have limitations as they require those involved to maintain a high level of variable control. The experimental results suffer the risk of human error. Our numerical results included several "dropouts", stemming from data not being properly registered by the probes. This is a limitation with the Hydrodynamic Laboratory. We could possibly have removed the dropouts experimentally by using a lower amplitude factor, but this would reduce the steepness of waves over the shoal. The reduced steepness is emblematic of the reduced nonlinearity caused by reducing the amplitude factor.

A clear limitation of the study of the mechanical parameters of Section 8.1 is using the half peak half width estimation method of bandwidth. It produces unreliable results when studying a process undergoing spectral deformation. In future work a more reliable method of calculating bandwidth should be implemented.

The correlation between surface elevation and the velocity field is sometimes less than 0.9. This could be actual results in accordance with the 'true' state of the world or it could be due to problems with the synchronisation between the ultrasound probes and ADV. The problem is we do not know for certain and have no benchmark. This is a perfect topic for numerical simulations.

Moreover, the correlation tested in this thesis is the Pearson correlation coefficient which reflects linear correlation of variables. Yet, from our study

of copulae we see that the dependence in our data is best reflected by a T-copula indicating that there is tail dependence between the surface elevation and velocity field. We have not analysed the strength of the tail dependence. Further research should study the tail dependence in more detail possibly deriving tail dependence coefficients.

We calculated copulae for four different positions along the tank. This is due to computational cost. Although we can gleam valuable insights for the analysis, studying four positions does not provide the full picture. Further work could extend the analysis to more positions along the tank. Additionally, we did our copula analysis for three different copulae. There are many other possible copula methods that could have been included. This could also possibly be expanded on in further work.

An analysis of data using Hilbert transforms would have been interesting, but time limitations saw this relegated to Appendix C. The theory described there includes novel discoveries made by the author and was therefore included even though the framework was not applied to the experimental data. This analysis is planned to be continued in further work.

# CHAPTER 11

## Conclusion

Numerous studies have shown, experimentally and numerically, that a inhomogenous wave field that propagates over non-uniform bathymetry has a larger probability of rogue waves in the shallow regime above the shoal. Furthermore, autokurtosis of the surface elevation and velocity field have their maxima and minima at different locations along the shoal. As a natural continuation of this work, we wanted to study the effects of wave spectra and the bathymetry separately and therefore performed two different experiments.

The first experiment studies the effects of an 'interesting' narrow banded spectrum with uniform bathymetry. The second experiment utilises a 'boring' spectrum, but with a varying bathymetry. Experiment one shows that the autokurtosis of the surface elevation increases faster when it has a higher initial BFI. Further, the autokurtosis of the surface elevation and velocity field increase at different rates.

Experiment two studies the effects of non-uniform bathymetry on a wave process with a Pierson-Moskowitz spectrum. We show that the automoments follow a similar trend as Trulsen, Raustøl et al. (2020). Q-Q plots and estimated probability functions reveal that distributions of the surface elevation and velocity field behave differently. They also show that the stabilisation of the surface elevation autokurtosis and autoskewness is asymmetric. Furthermore, our results indicate that the cokurtosis of the surface elevation and velocity field decreases as the uphill slope onto the shoal becomes steeper. The dependence structure of the surface elevation and velocity field is described by a T-copula implying that the surface elevation and velocity field have tail dependence in both tails.

# Appendices

# APPENDIX A

# Extended Results

## A.1  Experiment 2

Figure A.1 are the plots of the autoskewness of the surface elevation of shoal 2, (a), and shoal 3,(b). They are not included in the main text as they are superfluous. They both depict the autoskewness increasing as the wave propagates over the shoal plateau. Noticeably, we see that the autoskewness is stable until $x = 0$ m where the shoal plateau starts.

Similarly, in Figure A.2 are the plots of the autoskewness of the velocity field of shoal 2, (a), and shoal 3, (b).



(a)  (b)
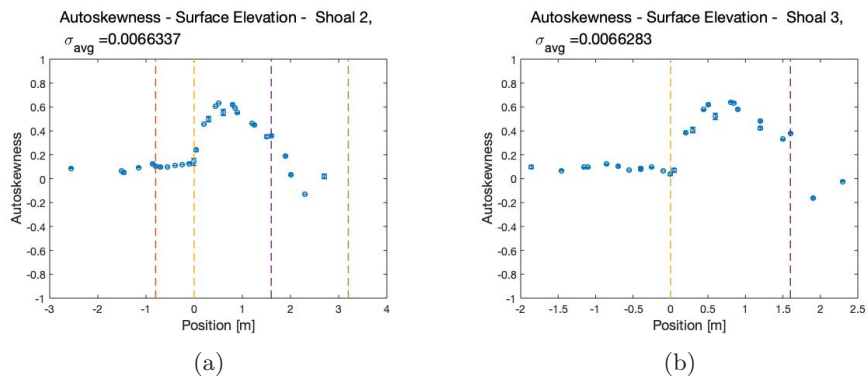
Figure A.1: Figure (a) surface elevation autoskewness, shoal 2. Figure (b) surface elevation autoskewness, shoal 3.
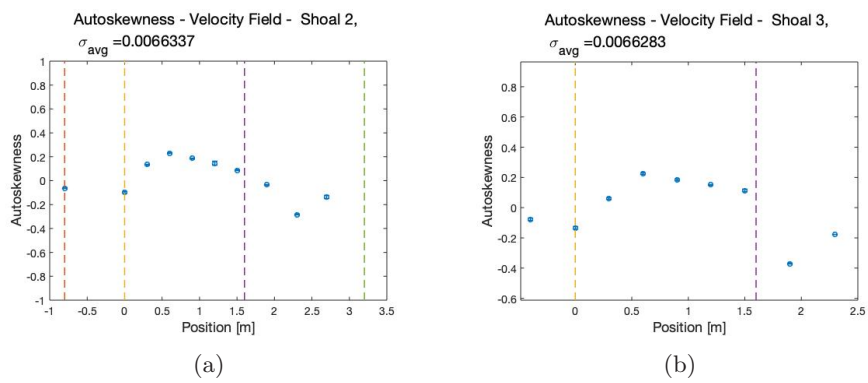
Figure A.2: Figure (a) velocity field autoskewness, shoal 2. Figure (b) velocity field autoskewness, shoal 3.

# APPENDIX B

---

# Verifying the Equipment

---

To test the ultrasound probes and the Vectrino we conducted an experiment with monochromatic waves with a constant depth. We performed eight different test cases with three runs in each case. This gave us a grand total of 27 runs. Each run lasted 1 minute. We started with a very low small wave maker displacement, and for each test case we increased it.

| Test case | Displacement |
|-----------|--------------|
| 1 | 0.050 |
| 2 | 0.075 |
| 3 | 0.100 |
| 4 | 0.125 |
| 5 | 0.150 |
| 6 | 0.175 |
| 7 | 0.200 |
| 8 | 0.225 |

Table B.1: Test cases of equipment verification

The water depth kept constant at 0.5 m. and the ADV depth was kept constant at -0.0725 below the quiescent surface. The peak period was $T_p = 1$ for all runs.

## B.1 Ultrasound Probes

To test the ultrasounds probes we want to test their ability to reproduce a monochromatic wave. We found the theoretical amplitude manually. Due to time constraints and the exercise being of limited interest we chose to only include a plot of test case 1.

We see that our measurements fit well with a monochromatic wave. There are some slight deviation which is to be expected for experimental data.

## B.2 ADV

The functionality and accuracy of ADVs in general and Vectrinos in particular are both heavily documented. The Vectrino is a plug-and-play lab instrument that is calibrated at the factory. Furthermore, the geometry of the Vectrino
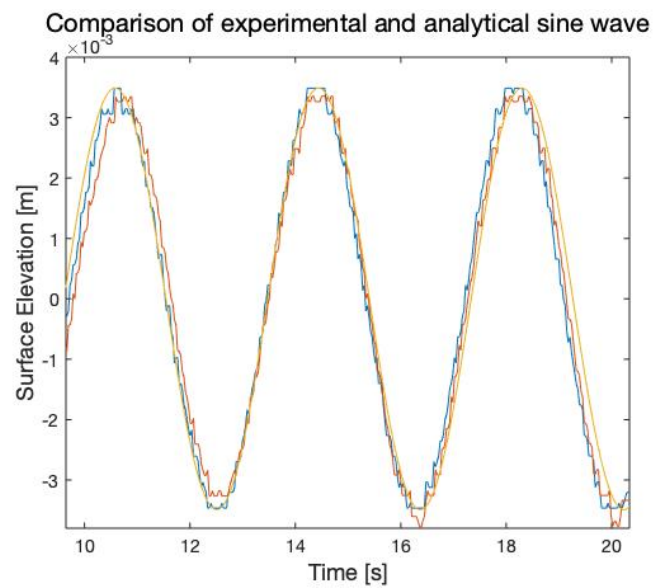
Figure B.1: Figure comparing two experimental runs in test case 1 with a sine wave.

probe does not change unless it has been physically damaged in some way. Damage can easily be visually detected by inspection. Moreover, the Vectrino has built-in software, called `Probe Check`, that will detect damage.

P. J. Rusello et al. (2006) found that the Vectrino has an accuracy of 4% by testing the Vectrino against PIV measurements.

# APPENDIX C

---

# Hilbert Transforms

---

## C.1 The Hilbert transform in 1D

An important first step when introducing Hilbert transforms is to clarify that they have nothing to do with Hilbert spaces, other than that they are the work of the same illustrious mathematician, David Hilbert. A Hilbert transform is a linear operator that transforms a function $f(t)$, where t is a real value, into $Hf(x)$.

The Hilbert transform on the real line is defined, in King ([2009b](#)), by the principal value integral

$$Hf(x) = \frac{1}{\pi} P \int_{-\infty}^{\infty} \frac{f(t)}{x-t} dt \tag{C.1}$$

Let

$$g(x) = \frac{1}{\pi} P \int_{-\infty}^{\infty} \frac{f(t)}{x-t} dt \tag{C.2}$$

then the function f is connected to g by the following result:

$$f(x) = -\frac{1}{\pi} P \int_{-\infty}^{\infty} \frac{g(t)}{x-t} dt \tag{C.3}$$

Equation C.2 and C.3 are a Hilbert transform pair.

### The Hilbert Envelope

There are many alternative definitions of what an envelope of a process can be. Moreover, there are many different types of Hilbert transform which do not always share the same statistical properties. The definition of a Hilbert envelope in this thesis relies on the work of Ochi ([1998](#)), Papoulis and Pillai ([2002](#)), and Lindgren ([2013](#)).

We define the underlying signal as $x(t)$ and the Hilbert transform as $Hf(t)$. The Hilbert envelope is then

$$\varepsilon(t) = \sqrt{x^2(t) + Hf^2(t)} \tag{C.4}$$

Futheremore we have

$$x(t) = \varepsilon(t) \cos \psi(t)$$

$$Hf(t) = \varepsilon(t)\sin\psi(t)$$

where $\psi(t)$ is the total phase of $x(t)$.

## C.2 Properties of Hilbert Transforms

The Hilbert transform two properties that are highly interesting for this thesis. The first is that the Hilbert transform and the underlying signal are orthogonal, meaning that as long as they are at the same time step, they are uncorrelated. The second is that if the underlying process is Gaussian then the envelope of the Hilbert transform has a Rayleigh distribution. These properties will be shown in turn.

### The Hilbert transform and its signal are orthogonal

This can be shown two ways, with a Plancherels identity and by calculating the correlation. This thesis chooses to display the latter proof. It is first worth defining the inner product such that

$$\langle u, v \rangle = \text{Cov}(u, v). \tag{C.5}$$

It is clear that processes that are uncorrelated are orthogonal and vice versa, as long as they are at the same time step.

### Uncorrelated

This proof, based on a proof from Lindgren (2013), will show that as long as the time difference, $\tau = 0$ then

$$\text{Cov}(x, \hat{x}) = 0$$

*Proof.* Let the underlying process x(t) be a weakly stationary stochastic process with zero mean $E[x] = 0$ and power spectrum $S(\omega)$. The covariance is given by

$$\text{Cov}[x, Hf] = \text{E}[x(t+\tau), Hf(t)^*]$$

$$= \int_{-\infty}^{\infty} \int_{-\infty}^{\infty} g(\omega_2)^* \, \text{E}[\hat{X}(\omega_1), \hat{X}(\omega_2)^*] e^{-i\omega_1(t+\tau)+i\omega_2 t} \, \mathrm{d}\omega_1 \, \mathrm{d}\omega_2,$$

where $\hat{X}$ is the Fourier transform. We define

$$g(\omega) = \begin{cases} i \text{ for } \omega < 0, \\ 0 \text{ for } \omega = 0, \\ -i \text{ for } \omega > 0. \end{cases}$$

For a weakly stationary process we have,

$$\text{E}[X(\omega_1), Hf(\omega_2)^*] = \delta(\omega_1 - \omega_2)S(\omega_1),$$

hence

$$\text{Cov}[x, \hat{x}] = -\int_0^{\infty} S_{one-sided}(\omega)\sin(\omega\tau) \, \mathrm{d}\omega.$$

Since we have clearly specified that the time difference is zero, $\tau = 0$ then we get,

$$\mathrm{Cov}[x, \hat{x}] = 0.$$

∎

## If the underlying process is Gaussian then Hilbert envelope is Rayleigh distributed

Let the underlying process, $x(t)$, be a Gaussian process with zero mean, $E[x(t)] = 0$ and power spectrum $S(\omega)$. The variance of $x(t)$ is given by

$$\mathrm{Var}[x(t)] = R(0) = \int_{\infty}^{-\infty} S(\omega_1) \, \mathrm{d}\omega_1.$$

Let

$$g(\omega) = -i \, \mathrm{Sign} \, \omega.$$

The variance of the Hilbert Transform, $Hf(t)$ of the underlying process $x(t)$ is given by

$$\mathrm{Var}[Hf(t)] = E[Hf(t)Hf^*(t)],$$
$$= \int_{-\infty}^{\infty} \int_{-\infty}^{\infty} g(\omega_1)g^*(\omega_2) \, \mathrm{E}[\hat{X}(\omega_1)\hat{X}^*(\omega_2)]e^{i(\omega_2 - \omega_1)t} \, \mathrm{d}\omega_1 \, \mathrm{d}\omega_2.$$

Let $\hat{X}$ denote the Fourier transform. For a weakly stationary process we have

$$\mathrm{E}[\hat{X}(\omega_1)\hat{X}^*(\omega_2)] = \delta(\omega_1 - \omega_2)S(\omega_1).$$

Therefore we get

$$\mathrm{Var}[\hat{x}(t)] = \int_{-\infty}^{\infty} \int_{-\infty}^{\infty} g(\omega_1)g^*(\omega_2)\delta(\omega_1 - \omega_2)S(\omega_1)e^{i(\omega_2 - \omega_1)t} \, \mathrm{d}\omega_1 \, \mathrm{d}\omega_2,$$
$$= \int_{-\infty}^{\infty} S(\omega_1) \, \mathrm{d}\omega_1.$$

It is clear that the Hilbert transform and the underlying process have the same variance. The Hilbert transform can be seen as a linear superposition of different time instances of the underlying process. Since the underlying process is Gaussian then the Hilbert transform is also Gaussian.

If the under ying process is a weakly stationary Gaussian process then the Hilbert transform is an identically distributed Gaussian process. At the same time instance they are uncorrelated. It there must follow that they are independent at that time instance. The Hilbert envelope is defined by

$$\varepsilon(t) = \sqrt{x^2(t) + Hf^2(t)}.$$

The square of a Gaussian process, such as the underlying process and the Hilbert transform, has a Chi-squared distribution. The square root of a Chi-squared distribution is a sum of several Chi - distributions. This means that if

$Z_1, Z_2, ..., Z_n$ are independent standard normally distributed variables, i.e with mean $\mu = 0$ and standard deviation $\sigma = 1$, we can write

$$Y = \sqrt{\sum_{i=1}^{n} Z_i^2}$$

where Y has a chi-distribution with $n$ degrees of freedom. The Hilbert envelope has this exact structure and must there have a Chi-distribution with two degrees of freedom, which is a Rayleigh distribution. It is possible to conclude that if underlying process is Gaussian, then the Hilbert transform is also a Gaussian process, whilst the Hilbert Envelope is Rayleigh distributed.

## C.3 The n-dimensional Hilbert Transform

For the case $n = 1$ there is only one possible definition of the Hilbert transform. For the case $n \geq 2$, there are infinitely many choices. The specific choice given in King (2009b) is

$$H_n f(x_1, x_2, \ldots, x_n) = \frac{1}{\pi^n} P \int_{-\infty}^{\infty} \int_{-\infty}^{\infty} \int_{-\infty}^{\infty}$$
$$\times \cdots \int_{-\infty}^{\infty} \frac{f(s_1, s_2, \cdots, s_n) ds_1, ds_2, \cdots, ds_n}{\prod_{k=1}^{n}(x_k - s_k)}.$$

Note that the notation $H_1$ is reserved for the one-sided Hilbert transform and not the one-dimensional case. Moreover it is assumed that the Cauchy principal value applies to each individual integral. This means that a the n-dimensional Hilbert Transform can be concisely defined as

$$H_n f(x) = \frac{1}{\pi^n} P \int_{-\infty}^{\infty} f(s) \prod_{k=1}^{n} \frac{1}{(x_k - s_k)} ds \qquad (C.6)$$

An important property of n-dimensional Hilbert transforms is that they can be written as a product of one-dimensional Hilbert transforms. The subscript $H_{(k)}$ denotes the one-dimensional operator. Therefore the n-dimensional Hilbert transform can be written as

$$H_n = \prod_{k=1}^{n} H_{(k)} \qquad (C.7)$$

We also demand that the operator $H_{(k)}$ satisfies that the commutor condition

$$[H_{(k)}, H_{(j)}] = 0, \quad j, k = 1, 2, \cdots, n.$$

### Example: The Double Hilbert Transform

The n-dimensional Hilbert transform with n=2, is the double Hilbert transform which can be expressed as

$$H_2 f(x_1, x_2) = \frac{1}{\pi^2} P \int_{-\infty}^{\infty} P \int_{-\infty}^{\infty} \frac{f(s_1, s_2) \, ds_1 \, ds_2}{(x_1 - s_1)(x_2 - s_2)} \qquad (C.8)$$

**Example: The Hilbert transform of cos(ax)**

Let

$$f(x) = \cos(a \cdot x) = \cos(a_1 x_1 + a_2 x_2 + \cdots + a_n x_n),$$

the

$$
\begin{aligned}
H_n[\cos(a \cdot x)] &= \frac{1}{\pi^n} P \int_{-\infty}^{\infty} \frac{\mathrm{d}s_1}{x_1 - s_1} \int_{-\infty}^{\infty} \frac{\mathrm{d}s_2}{x_2 - s_2} \\
&\quad \times \cdots \int_{-\infty}^{\infty} \frac{\cos(a_1 s_1 + a_2 s_2 + \cdots + a_n s_n) \, \mathrm{d}s_n}{x_n - s_n}, \\
&= \frac{1}{\pi^n} P \int_{-\infty}^{\infty} \frac{\mathrm{d}s_1}{x_1 - s_1} \int_{-\infty}^{\infty} \frac{\mathrm{d}s_2}{x_2 - s_2} \\
&\quad \times \cdots \int_{-\infty}^{\infty} \frac{\cos(a_1 s_1 + a_2 s_2 + \cdots + a_n x_n - a_n y) \, \mathrm{d}y}{y}, \\
&= \frac{1}{\pi^n} P \int_{-\infty}^{\infty} \frac{\mathrm{d}s_1}{x_1 - s_1} \int_{-\infty}^{\infty} \frac{\mathrm{d}s_2}{x_2 - s_2} \cdots \\
&\quad \times \cdots [\sin(a_1 s_1 + a_2 s_2 + \cdots + a_n x_n)] \int_{-\infty}^{\infty} \frac{\cos(a_n y) \, \mathrm{d}y}{y}, \\
&= \frac{1}{\pi^n} P \int_{-\infty}^{\infty} \frac{\mathrm{d}s_1}{x_1 - s_1} \int_{-\infty}^{\infty} \frac{\mathrm{d}s_2}{x_2 - s_2} \cdots \\
&\quad \times \cdots [\sin(a_1 s_1 + a_2 s_2 + \cdots + a_n x_n)] \pi \operatorname{Sign} a_n, \\
&= \frac{1}{\pi^n} P \int_{-\infty}^{\infty} \frac{\mathrm{d}s_1}{x_1 - s_1} \int_{-\infty}^{\infty} \frac{\mathrm{d}s_2}{x_2 - s_2} \cdots \\
&\quad \times \cdots \int_{-\infty}^{\infty} \frac{\sin(a_1 s_1 + a_2 s_2 + \cdots + a_n s_n) \, \mathrm{d}s_{n-1}}{x_{n-1} - s_{n-1}}.
\end{aligned}
$$

This can be simplified to

$$
H_n[\cos(a \cdot x)] = \begin{cases} (-1)^{\frac{(n-1)}{2}} \sin(a \cdot x) \prod_{k=1}^{n} \operatorname{Sign} a_k, & \text{for } n \text{ odd} \\ (-1)^{\frac{(n)}{2}} \cos(a \cdot x) \prod_{k=1}^{n} \operatorname{Sign} a_k, & \text{for } n \text{ even} \end{cases}
$$

For $n = 2, a_1 = 1, a_2 = 2$ we get

$$
\begin{aligned}
H_n[\cos(x + y)] &= (-1)^{\frac{(2)}{2}} \cos(x + y) \prod_{k=1}^{2} \operatorname{Sign} a_k \\
&= -\cos(x + y)
\end{aligned}
$$

For $n = 3, a_1 = 1, a_2 = 1, a_3 = 1$ we get

$$
\begin{aligned}
H_n[\cos(x + y + z)] &= (-1)^{\frac{(3-1)}{2}} \sin(x + y + z) \prod_{k=1}^{3} \operatorname{Sign} a_k \\
&= -\sin(x + y + z)
\end{aligned}
$$

**Are n-dimensional Hilbert transforms orthogonal with their signal?**

This section discusses the whether n-dimensional Hilbert transforms are orthogonal with the underlying signal. This section relies on the work of

King (2009b) and the importance of this section cannot be stated strongly enough. To be able to be able to discuss the statistical properties of the multidimensional Hilbert transform, as well as the multi dimensional Hilbert envelope, we demand that the Hilbert transform is uncorrelated in with the underlying signal. Consequently the Hilbert transform must be orthogonal to its underlying signal

From Appendix C.2, it is clear the one dimensional Hilbert transforms are orthogonal to the underlying signal. Multidimensional Hilbert transforms are different. If the number of dimensions, $n$, is an odd number then the n-dimensional Hilbert transform is uncorrelated with the underlying signal,

$$\int_{\mathbb{R}^n} f(x) H_n f(x) \, dx = 0, \quad \text{if } n = \text{ odd number.} \tag{C.9}$$

*Proof.* From King (2009b), we see that the n-dimensional Hilbert transform satisfies the Parseval inspired formula

$$\int_{\mathbb{R}^n} H_n f(x) g(x) dx = (-1)^n \int_{\mathbb{R}^n} f(x) H_n g(x) dx \tag{C.10}$$

If we now let $g(x) = H_n f(x)$, the we arrive at

$$\int_{\mathbb{R}^n} \{H_n f(x)\}^2 \, dx = \int_{\mathbb{R}^n} \{f(x)\}^2 \, dx. \tag{C.11}$$

Equation C.10, can also be expressed as

$$\int_{\mathbb{R}^n} H_n f_1(x) H_n f_2(x) \, dx = \int_{\mathbb{R}^n} f_1(x) f_2(x) \, dx \tag{C.12}$$

where $f_1 = f$ and $g = H_n f_2$, and is a generalisation of C.11 for a multidimensional case. Now let $f \in L^2(\mathbb{R}^n)$ and set $g = f$, then

$$\int_{\mathbb{R}^n} H_n f(x) f(x) \, dx = (-1)^n \int_{\mathbb{R}^n} f(x) H_n f(x) \, dx$$

which gives us

$$\{1 - (-1)^n\} \int_{\mathbb{R}^n} f(x) H_n f(x) \, dx = 0 \tag{C.13}$$

If n is odd, then

$$\int_{\mathbb{R}^n} f(x) H_n f(x) \, dx = 0. \tag{C.14}$$

From the proof above it is clear that the n dimensional Hilbert transform is orthogonal with its signal if the number of dimensions corresponds to an odd number. ∎

# APPENDIX D

---

# Code

---

This appendix was inspired by Raustøl (2014) as she included the filtering code in the appendix of her master thesis. That code was the basis for my filtering code. In the hopes the I can pay it forward I have attached some code in this appendix.

## D.1   Postprocessing

```
    function [P4] = zeropadding(Z1, Probe4)
%Sizes
N = size(Z1,1);
M = size(Probe4,1);

K = (N-M)/2;
a = ceil(K);
b = floor(K);

%IFFT and separation into real and imag
fn_hat = ifft(Probe4);
fn_real = real(fn_hat);
fn_imag = imag(fn_hat);

%FFTshift
fn_2real = fftshift(fn_real);
fn_2imag = fftshift(fn_imag);

%Zeropadding
before = zeros(a,1);
after = zeros(b,1);

temp_real = cat(1,before,fn_2real);
temp_imag = cat(1,before,fn_2imag);

temp_real = cat(1,temp_real,after);
temp_imag = cat(1,temp_imag,after);

%FFTshift back
```

```
fn_real = fftshift(temp_real);
fn_imag = fftshift(temp_imag);

%Combining real and imag
fn_hat = fn_real + 1i*fn_imag;

%FFT back
P4 = real(fft(fn_hat));


%Clearing temporary variables
clear a
clear b
clear before
clear after
clear K
clear M
clear fn_2imag
clear fn_2real
clear fn_hat
clear fn_imag
clear fn_real
clear temp_imag
clear temp_real

disp('Zeropadding done!')
end
```

# List of Figures

# List of Tables

# Bibliography

Alber, I. and Saffman, P. (1978). *Stability of Random Nonlinear Deep Water Waves with Finite Bandwidth Spectra*. TRW, Defense and Space Systems Group.

Alber, I. (1978). 'The effects of randomness on the stability of two-dimensional surface wavetrains'. In: *Proceedings of the Royal Society of London. A. Mathematical and Physical Sciences* vol. 363, no. 1715, pp. 525–546.

Bai, X. et al. (2020). 'Joint probability distribution of coastal winds and waves using a log-transformed kernel density estimation and mixed copula approach'. In: *Ocean Engineering* vol. 216, p. 107937.

Beji, S. and Battjes, J. (1993). 'Experimental investigation of wave propagation over a bar'. In: *Coastal Engineering* vol. 19, no. 1-2, pp. 151–162.

Benjamin, T. and Feir, J. (1967). 'The disintegration of water waves on deep water, 1, Theory'. In: *J. Fluid Mech* vol. 27, pp. 417–430.

Benjamin, T. B. (1967). 'Instability of periodic wavetrains in nonlinear dispersive systems'. In: *Proceedings of the Royal Society of London. Series A. Mathematical and Physical Sciences* vol. 299, no. 1456, pp. 59–76.

Bitner, E. M. (1980). 'Non-linear effects of the statistical model of shallow-water wind waves'. In: *Applied Ocean Research* vol. 2, no. 2, pp. 63–73.

Bouyé, E. et al. (2000). 'Copulas for finance-a reading guide and some applications'. In: *Available at SSRN 1032533*.

Bunnik, T. (2010). *Benchmark workshop on numerical wave modeling—description of test cases*. Tech. rep. Technical Report 70022-1-RD, MARIN, The Netherlands.

Cherneva, Z. et al. (2005). 'Probability distributions of peaks, troughs and heights of wind waves measured in the black sea coastal zone'. In: *Coastal Engineering* vol. 52, no. 7, pp. 599–615.

Corbella, S. and Stretch, D. D. (2013). 'Simulating a multivariate sea storm using Archimedean copulas'. In: *Coastal Engineering* vol. 76, pp. 68–78.

Crawford, D. R., Saffman, P. G. and Yuen, H. C. (1980). 'Evolution of a random inhomogeneous field of nonlinear deep-water gravity waves'. In: *Wave motion* vol. 2, no. 1, pp. 1–16.

Devore, J. L., Berk, K. N. and Carlton, M. A. (2012). *Modern mathematical statistics with applications*. Springer.

Dysthe, K., Krogstad, H. E. and Müller, P. (2008). 'Oceanic rogue waves'. In: *Annu. Rev. Fluid Mech.* vol. 40, pp. 287–310.

Dysthe, K. B. et al. (2003). 'Evolution of a narrow-band spectrum of random surface gravity waves'. In: *Journal of Fluid Mechanics* vol. 478, pp. 1–10.

Feir, J. (1967). 'Discussion: some results from wave pulse experiments'. In: *Proceedings of the Royal Society of London. Series A. Mathematical and Physical Sciences* vol. 299, no. 1456, pp. 54–58.

General Acoustics (2013). *R: ULS Advanced User Manual, ver 2.3.*

Genest, C. and Rémillard, B. (2006). 'Discussion of" copulas: Tales and facts", by Thomas Mikosch'. In: *Extremes* vol. 9, no. 1, pp. 27–36.

Gevik, B., Pedersen, G. K. and Trulsen, K. (2021). *Lecture Notes MEK4320, Hydrodynamic Wave Theory.* Department of Mathematics, University of Oslo.

Gramstad, O. et al. (2013). 'Freak waves in weakly nonlinear unidirectional wave trains over a sloping bottom in shallow water'. In: *Physics of Fluids* vol. 25, no. 12, p. 122103.

Grue, J. (1992). 'Nonlinear water waves at a submerged obstacle or bottom topography'. In: *Journal of Fluid Mechanics* vol. 244, pp. 455–476.

Hasimoto, H. and Ono, H. (1972). 'Nonlinear modulation of gravity waves'. In: *Journal of the Physical Society of Japan* vol. 33, no. 3, pp. 805–811.

Hasselmann, K. et al. (1973). 'Measurements of wind-wave growth and swell decay during the Joint North Sea Wave Project (JONSWAP).' In: *Ergaenzungsheft zur Deutschen Hydrographischen Zeitschrift, Reihe A.*

Haver, S. (2004). 'A possible freak wave event measured at the Draupner Jacket January 1 1995'. In: *Rogue waves.* Vol. 2004, pp. 1–8.

Al-Humoud, J., Tayfun, M. and Askar, H. (2002). 'Distribution of nonlinear wave crests'. In: *Ocean engineering* vol. 29, no. 15, pp. 1929–1943.

Iyengar, S. G. et al. (2010). 'Quantifying EEG synchrony using copulas'. In: *2010 IEEE International Conference on Acoustics, Speech and Signal Processing*, pp. 505–508.

Janssen, P. A. (2003). 'Nonlinear four-wave interactions and freak waves'. In: *Journal of Physical Oceanography* vol. 33, no. 4, pp. 863–884.

Janssen, T. T. and Herbers, T. (2009). 'Nonlinear wave statistics in a focal zone'. In: *Journal of Physical Oceanography* vol. 39, no. 8, pp. 1948–1964.

Janssen, T., Herbers, T. and Battjes, J. (2008). 'Evolution of ocean wave statistics in shallow water: Refraction and diffraction over seafloor topography'. In: *Journal of Geophysical Research: Oceans* vol. 113, no. C3.

Jorde, S. (2018). 'Kinematikken i bølger over en grunne'. MA thesis.

Kashima, H., Hirayama, K. and Mori, N. (2014). 'Estimation of freak wave occurrence from deep to shallow water regions'. In: *Coastal Engineering Proceedings* vol. 1, no. 34, p. 36.

Kilgore, R. T. and Thompson, D. B. (2011). 'Estimating joint flow probabilities at stream confluences by using copulas'. In: *Transportation research record* vol. 2262, no. 1, pp. 200–206.

King, F. W. (2009a). *Hilbert transforms.* Vol. 1. Cambridge University Press Cambridge.

— (2009b). *Hilbert transforms.* Vol. 2. Cambridge University Press Cambridge.

Lapuyade-Lahorgue, J., Xue, J.-H. and Ruan, S. (2017). 'Segmenting multi-source images using hidden markov fields with copula-based multivariate statistical distributions'. In: *IEEE Transactions on Image Processing* vol. 26, no. 7, pp. 3187–3195.

Lawrence, C., Trulsen, K. and Gramstad, O. (2021). 'Statistical properties of wave kinematics in long-crested irregular waves propagating over non-uniform bathymetry'. In: *Physics of Fluids* vol. 33, no. 4, p. 046601.

Lindgren, G. (2013). *Stationary stochastic processes: theory and applications.* CRC Press.

McLean, J. W. (1982). 'Instabilities of finite-amplitude gravity waves on water of finite depth'. In: *Journal of Fluid Mechanics* vol. 114, pp. 331–341.

McLean, J. et al. (1981). 'Three-dimensional instability of finite-amplitude water waves'. In: *Physical Review Letters* vol. 46, no. 13, p. 817.

McNeil, A. J., Frey, R. and Embrechts, P. (2015). *Quantitative risk management: concepts, techniques and tools-revised edition.* Princeton university press.

Mikosch, T. (2005). *Copulas: tales and facts.* Laboratory of Actuarial Mathematics, University of Copenhagen.

Miller, M. B. (2013). *Mathematics and Statistics for Financial Risk Management.* Wiley.

Mori, N. and Kobayashi, N. (1999). 'Nonlinear Distribution of Neashore Free Surface and Velocity'. In: *Coastal Engineering 1998*, pp. 189–202.

Mori, N. and Yasuda, T. (2002). 'A weakly non-Gaussian model of wave height distribution for random wave train'. In: *Ocean Engineering* vol. 29, no. 10, pp. 1219–1231.

Newman, J. N. (2018). *Marine hydrodynamics.* The MIT press.

Ochi, M. K. (1998). *Ocean waves.* Cambridge University Press.

Papoulis, A. and Pillai, S. U. (2002). *Probability, random variables, and stochastic processes.* Tata McGraw-Hill Education.

Pierson Jr, W. J. and Moskowitz, L. (1964). 'A proposed spectral form for fully developed wind seas based on the similarity theory of SA Kitaigorodskii'. In: *Journal of geophysical research* vol. 69, no. 24, pp. 5181–5190.

Poindexter, C., Rusello, P. and Variano, E. (2011). 'Acoustic Doppler velocimeter-induced acoustic streaming and its implications for measurement'. In: *Experiments in fluids* vol. 50, no. 5, pp. 1429–1442.

Raustøl, A. (2014). 'Freake bølger over variabelt dyp'. MA thesis.

Rusello, P. J. et al. (2006). 'Improvements in acoustic Doppler velocimetery'. In.

Rye, L. B. (2014). 'Freak waves in crossing sea with counterpropagating wave systems'. MA thesis.

Schmidt, T. (Jan. 2007). 'Coping with copulas'. In: *Copulas - From Theory to Application in Finance.*

Sergeeva, A., Pelinovsky, E. and Talipova, T. (2011). 'Nonlinear random wave field in shallow water: variable Korteweg-de Vries framework'. In: *Natural Hazards and Earth System Sciences* vol. 11, no. 2, pp. 323–330.

Sklar, M. (1959). 'Fonctions de repartition an dimensions et leurs marges'. In: *Publ. inst. statist. univ. Paris* vol. 8, pp. 229–231.

Trulsen, K., Raustøl, A. et al. (2020). 'Extreme wave statistics of long-crested irregular waves over a shoal'. In: *Journal of Fluid Mechanics* vol. 882.

Trulsen, K., Zeng, H. and Gramstad, O. (2012). 'Laboratory evidence of freak waves provoked by non-uniform bathymetry'. In: *Physics of Fluids* vol. 24, no. 9, p. 097101.

Viotti, C. and Dias, F. (2014). 'Extreme waves induced by strong depth transitions: Fully nonlinear results'. In: *Physics of Fluids* vol. 26, no. 5, p. 051705.

Whitham, G. (1967). 'Non-linear dispersion of water waves'. In: *Journal of Fluid Mechanics* vol. 27, no. 2, pp. 399–412.

Whitham, G. B. (1967). 'Variational methods and applications to water waves'. In: *Proceedings of the Royal Society of London. Series A. Mathematical and Physical Sciences* vol. 299, no. 1456, pp. 6–25.

Wilk, M. B. and Gnanadesikan, R. (1968). 'Probability plotting methods for the analysis for the analysis of data'. In: *Biometrika* vol. 55, no. 1, pp. 1–17.

Yu, B. et al. (2014). 'Laboratory study of the nonlinear transformation of irregular waves over a mild slope'. In: *China Ocean Engineering* vol. 28, no. 4, pp. 489–500.

Zeng, H. and Trulsen, K. (2012). 'Evolution of skewness and kurtosis of weakly nonlinear unidirectional waves over a sloping bottom'. In: *Natural Hazards and Earth System Sciences* vol. 12, no. 3, pp. 631–638.